Oxidative Chemical Vapor Deposition of Conductive Polymers for Use in Novel Photovoltaic Device Architectures

by

Rachel M. Howden

B.S. Engineering
Harvey Mudd College, 2008

M.S. Chemical Engineering Practice
Massachusetts Institute of Technology, 2013

SUBMITTED TO THE DEPARTMENT OF CHEMICAL ENGINEERING IN PARTIAL FULFILLMENT OF THE REQUIREMENTS FOR THE DEGREE OF

DOCTOR OF PHILOSOPHY IN CHEMICAL ENGINEERING

at the

MASSACHUSETTS INSTITUTE OF TECHNOLOGY

JUNE 2013

Signature of Author: _____
Department of Chemical Engineering
April 2, 2013

Certified by: _____
Karen K. Gleason
Professor of Chemical Engineering
Thesis Supervisor

Accepted by: _____
Patrick S. Doyle
Professor of Chemical Engineering
Chairman, Committee for Graduate Students

Oxidative Chemical Vapor Deposition of Conductive Polymers for Use in Novel Photovoltaic Device Architectures

by

Rachel M. Howden

Submitted to the Department of Chemical Engineering
on April 2, 2013 in Partial Fulfillment of the
Requirements for the Degree of Doctor of Philosophy in
Chemical Engineering

Abstract

The conductive polymer poly(3,4-ethylenedioxythiophene), (PEDOT), deposited via oxidative chemical vapor deposition (oCVD) has been investigated for use in organic electronic devices. The oCVD process as well as the application of oCVD PEDOT in photovoltaic devices is described.

oCVD enables the synthesis of conjugated conductive films with advantageous properties for organic optoelectronic device applications. The oCVD process of forming the polymer film allows compatibility with a wide range of substrates, including those that are flexible or fragile, and provides a relatively low-energy means of depositing film layers that may not be possible through solution or other processing.

Films deposited using varying oCVD process and pre- and post-treatment parameters (e.g. temperature, oxidant exposure, rinsing) were characterized based on their physical and electrical properties. It was found that acid rinsing of the already deposited films led to lower sheet resistance and surface roughness and an improvement in film stability.

The oCVD PEDOT has been demonstrated as a replacement for solution-processed PEDOT:PSS as a hole transporting layer as well as for the transparent electrode material (typically ITO) in typical organic photovoltaic structures. Reverse-structure photovoltaic cells were also created using direct deposition of PEDOT electrodes onto small molecule active layer materials yielding fully dry-processed devices. The direct deposition of PEDOT top electrodes has enabled the fabrication of devices on opaque substrates leading to a greater than ten-fold improvement in previous devices fabricated on paper.

Compatibility with novel photovoltaic materials has been demonstrated in work done using oCVD PEDOT as HTLs on graphene electrodes to make ITO-free devices.

Thesis Supervisor: Karen Gleason

Title: Professor of Chemical Engineering

Acknowledgements

I would like to gratefully acknowledge the help of all those around me who played a significant role in me getting to this point in my career. I would like to thank my committee members Dr. Vladimir Bulović, Dr. Jing Kong, Dr. Michael Strano, and especially my thesis advisor Dr. Karen Gleason. It was due to Karen's optimistic guidance and motivation and allowing me to direct my own research efforts that I was able accomplish what I set out to do.

I would like to express my sincere appreciation for all the various collaborators I have had over the past 5 years who helped take my research to a new level, allowed me to integrate my process and materials with new and exciting research from other labs at MIT, and really again demonstrated to me the value of a collaborative, interdisciplinary learning environment. Miles Barr, Eletha Flores, Elaine McVay, Hyesung Park, and Rishabh Jain, thank you all so much.

I also want to thank all the other students at MIT either from my lab or other labs or classes I was in who helped me with their excellent discussions, training, brainstorming, troubleshooting, and all other work-related things, especially David Borrelli, Eric Shiue, Christy Petruzcok, Patrick Brown, Jill Macko, Mahriah Alf, and Andrew Hilmer.

I would like to acknowledge the MIT staff who have helped through many important steps on the way towards earning my PhD and created an excellent environment to work in in the Chemical Engineering Department

To all my friends and family, thank you so much for your love and support along the way. Having you around to enjoy Boston and take my mind off research has kept my life wonderfully in balance.

Table of Contents

List of Figures

List of Tables

List of Acronyms and Abbreviations

3TE	3-thiopheneethanol
AFM	atomic force microscopy
AP	atmospheric pressure
APCVD	atmospheric pressure chemical vapor deposition
BCP	bathocuproine
CCMR	Cornell Center for Materials Research
CN-PPV	cyano-polyphenylene vinylene
CuPc	Copper phthalocyanine
CVD	chemical vapor deposition
DBP	tetraphenyldibenzoperiflanthene
DOE	Department of Energy
EDOT	3,4-ethylene dioxythiophene
EDX	energy-dispersive X-ray spectroscopy
EET	exciton energy transfer
EHS	environment health and safety
EQE	external quantum efficiency
F8TBT	Poly[(9,9-dioctylfluorenyl-2,7-diyl)-alt-(4,7-bis(3-hexylthiophen-5-yl)-2,1,3-benzothiadiazole)-2',2''- diyl]
$Fe(OTs)_3$	iron (III) tosylate
FF	fill factor
FTIR	Fourier transform infrared spectroscopy
GPC	Gel permeation chromatography
HOMO	highest occupied molecular orbital
HTL	hole transporting layer
ITO	indium-tin oxide
J_{sc}	short circuit current
J-V	current-voltage
LP	low pressure
LPCVD	low pressure chemical vapor deposition
LUMO	lowest unoccupied molecular orbital
MEH-PPV	poly[2-methoxy-5-(2'-ethylhexyloxy)-p-phenylene vinylene]

MeOH	methanol
oCVD	oxidative chemical vapor deposition
OLED	organic light-emitting diode
OPV	organic photovoltaic
OTFT	organic thin-film transistor
P3HT	poly(3-hexylthiophene)
PCBM	[6,6]-phenyl-C_{61}-butyric acid methyl ester
PCE	power conversion efficiency
PEDOT	poly(3,4-ethylenedioxythiophene)
PEDOT:PSS	poly(3,4-ethylenedioxythiophene):poly(styrenesulfonate)
PEG-PPG-PEG	poly(ethylene glycol)-block-poly(propylene glycol)-block-poly(ethylene glycol)
PET	polyethylene terephthalate
PMMA	poly(methyl methacrylate)
PV	photovoltaic
QCM	quartz crystal microbalance
SEM	scanning electron microscope
rms	root mean square
R_{sh}	sheet resistance
SWNT	single-wall carbon nanotube
T	transmittance
TAA	2-thiophene acetic acid
TCE	transparent conducting electrode
TCO	transparent conducting oxide
UPS	ultraviolet photoelectron spectroscopy
UV-Vis	ultraviolet-visible (spectroscopy)
V_{oc}	open circuit voltage
VPP	vapor phase polymerization
WF	work function
XPS	x-ray photoelectron spectroscopy
XRD	x-ray diffraction
Z_0	impedance of free space
σ_{op}	optical conductivity

σ_{dc}	dc conductivity
η_p	power conversion efficiency

CHAPTER ONE

Introduction

1.1 Organic photovoltaics

Continual advancements in the field of renewable energies are essential to ensure the development and production of clean, cost-effective technologies for the future. One critical area of investigation is in the harvesting of solar energy. Though solar energy currently makes up only 0.1% of the nation's energy use, it still represents a multi-billion dollar, rapidly growing market, and thus small improvements to any aspect of the cell efficiency or cost and ease of manufacture can have a significant impact on the feasibility of large-scale production.[1]

An important area being explored by many researchers today is in using organic materials for optoelectronic applications. Some of the foreseen benefits of organic materials over inorganics include lower cost materials, lower energy processes, potential for thin, flexible, and even transparent devices, and rapid large-area production through the use of techniques such as roll to roll processing.[2] Organic photovoltaics are not necessarily intended to replace the current silicon photovoltaic market, in terms of efficiency, but rather to compliment current technology by diversifying the fields of applications to utilize solar energy in new, exciting ways.

1.2 Oxidative chemical vapor deposition (oCVD)

Many promising new materials have been and continue to be developed which have potential in organic electronic devices. However, beyond simply creating novel materials, an important consideration is the processing and feasibility of combining layers together. In many cases, the environment in which a new layer is added can hinder the performance or even destroy any existing layers. The compatibility of layers is crucial in the device architecture, which becomes difficult with organic layers due to the use of environmentally harmful solvents. The proper combination of solvents cannot always be found which will allow the placement of one layer without damaging others.

Chemical vapor deposition (CVD), a widely used technique, could present a viable alternative to solution-based methods of placing organic layers, and expand the possibilities of using organic materials in all areas of the device structure. A specific type of CVD processing developed in the Gleason Laboratory at MIT, dubbed oxidative CVD (oCVD), allows for the nondestructive deposition of conducting polymers onto a wide range of substrates. The oCVD process has most frequently been used to create (3,4-ethylenedioxythiophene), or PEDOT, a conductive polymer commonly used in many organic electronic devices.[3] The technique has also been demonstrated to work for other conducting polymers such as homo- and co- polymers of polypyrrole and polythiophene.[4]

An important concern for solar energy in general is the availability of materials. Even with many organic cells today that utilize polymer blend active layers, the electrodes are still constructed from materials of a limited supply in nature, such as indium tin oxide (ITO). Expanding the material set for photovoltaic applications improves the prospects for large-scale production and employment of this technology.[5]

1.2.1 Process overview

Oxidative chemical vapor deposition replicates the mechanism of oxidative polymerization in solution, in which a desired monomer reacts with an oxidizing species resulting in step growth polymerization. In contrast to solution oxidative polymerization, in oCVD both the monomer and oxidizing agent are introduced in the vapor phase. The materials react in a controlled environment within a vacuum deposition chamber to achieve in one step simultaneously polymer synthesis and deposition of a thin film. The thin film form of insoluble conjugated polymers is essential for device fabrication.

In order to be compatible with the oCVD process, liquid oxidants and monomers must have a high enough vapor pressure that they can be delivered to the substrate surface. Similarly, solid oxidants and monomers must be able to be heated to the vapor phase without first degrading. Table 1-1 shows a list of some of the oxidants and monomers that have been used in oCVD.

Table 1-1: Oxidants and monomers that have been used in oCVD[6]

Oxidants	Monomers
Iron(III) chloride	3,4 ethylenedioxythiophene (EDOT)
Iron(III) p-toluenesulfonate or iron(III) tosylate	Pyrrole
Copper(II) chloride	Thiophene
Bromine	2-thiophene acetic acid (TAA)
Vanadium oxytrichloride	3-thiopheneethanol (3TE)
	Selenophene

1.2.2 Benefits of oCVD

There are several benefits to using oCVD over solution processing or other types of vapor deposition techniques.

Solvent Use

The most unique advantage is that no solvent is required for the polymerization or deposition of the polymer films meaning the technique can be used to deposit insoluble polymers, for example, poly(3,4 ethylenedioxythiophene) (PEDOT) as opposed to PEDOT doped with poly(styrenesulfonate) (PEDOT:PSS). Several applications require the deposition of sequential layers of materials and in solution

processing care must be taken to ensure solvent compatibility with underlying layers. Also, with solution-processed layers, the annealing and drying process is crucial to the final film properties and can be difficult to keep repeatable.

Processing

oCVD is a relatively low energy process generally operating in the temperature range 20-150 °C and at moderate vacuum levels (10^{-1}-10^{-4} Torr). Patterning can be achieved using simple shadow masking.

Figure 1-1 shows a sample mask and patterned oCVD film. Masks can be created from a variety of materials (tape, plastics, metals) and the sharpness of the patterning depends on how flush the mask is to the substrate surface during film deposition. The mask shown in Figure 1-1 (Photo Etch Technology, stainless steel) is an example pattern for making PEDOT electrodes on 0.5" square substrates.

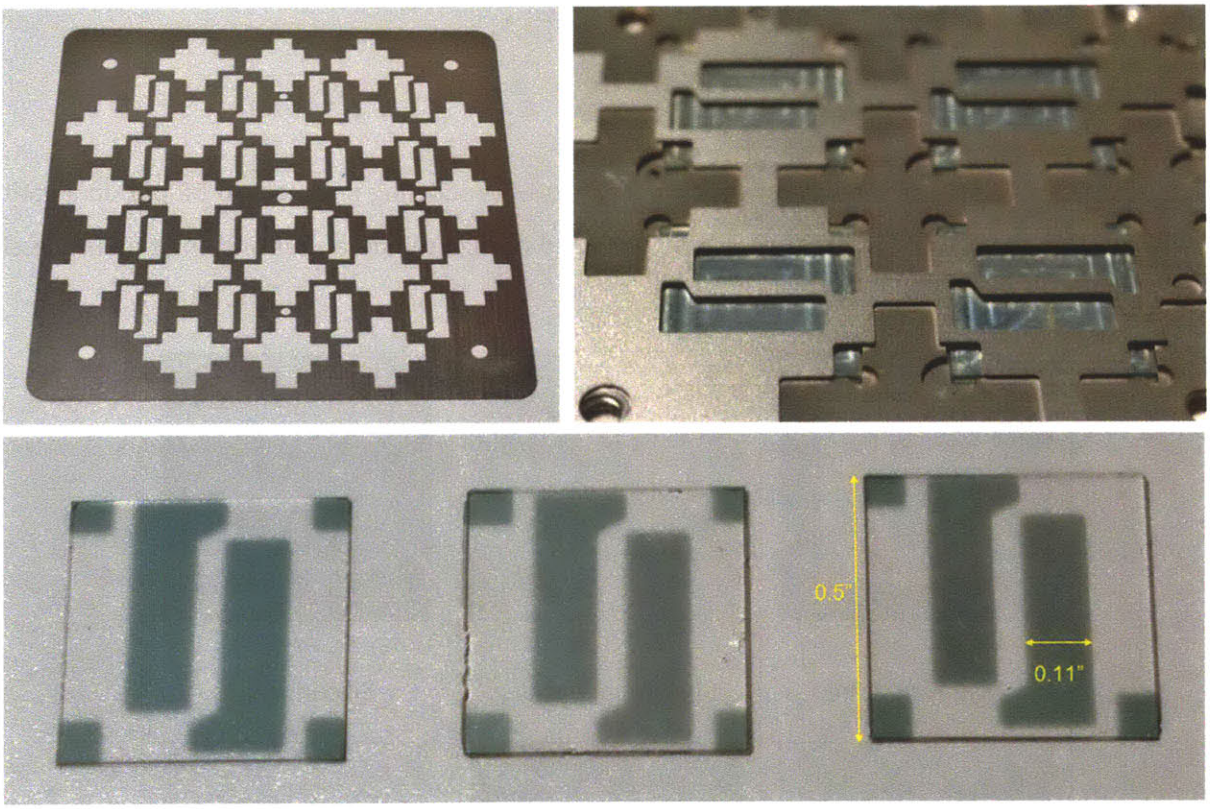

Figure 1-1: oCVD shadow mask and resulting patterned film

Conformality

Since oCVD is a vapor-processing technique, the deposited films display good conformality even over complex features (Figure 1-2).

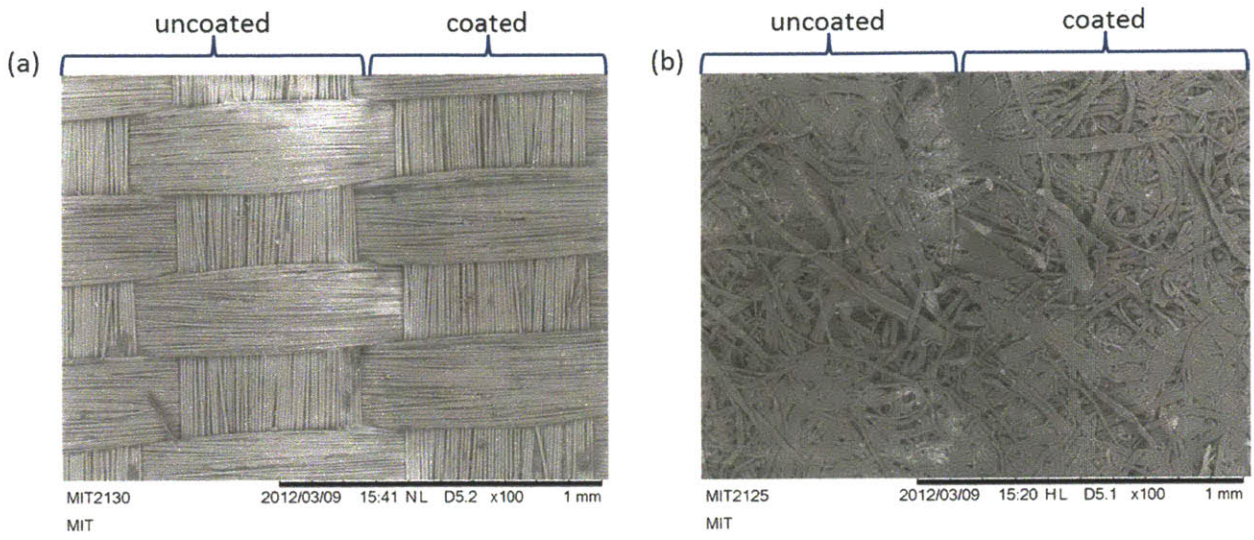

Figure 1-2: SEM images of PEDOT layer deposited on (a) woven backside of fiberglass cloth tape (Saint-Gobain Performance Plastics, CHR2915-7) and (b) paper towel.

Substrate Compatibility

The relatively mild deposition conditions allow for layers of conducting polymers to be put on a variety of different substrates that might otherwise be damaged by high temperatures and solution processing (Figure 1-3).

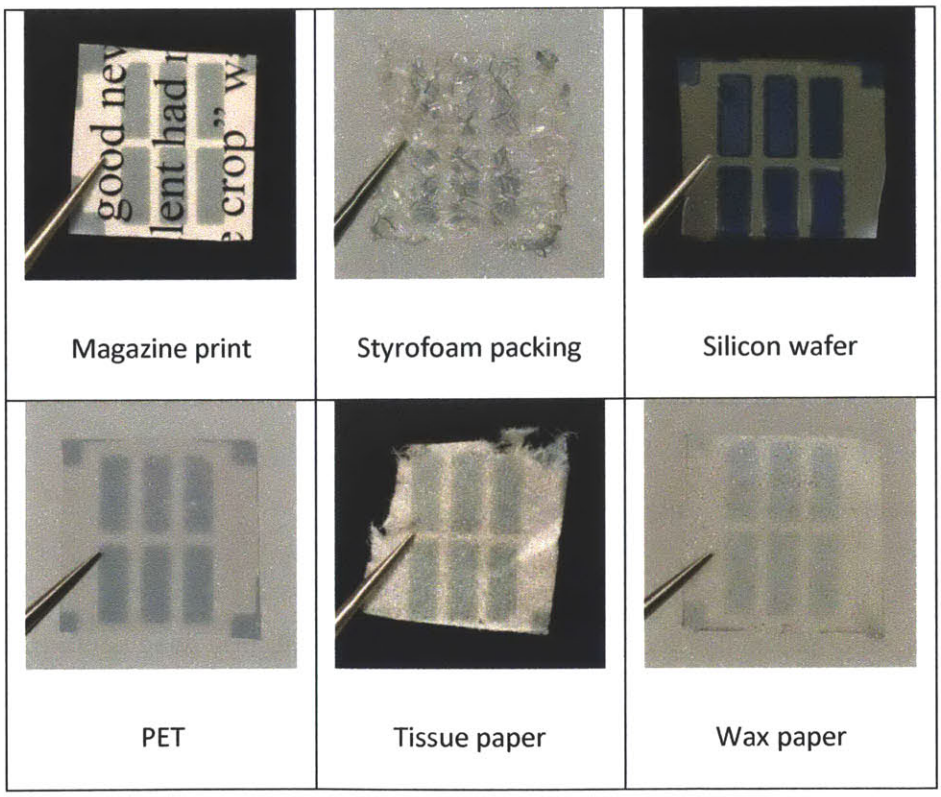

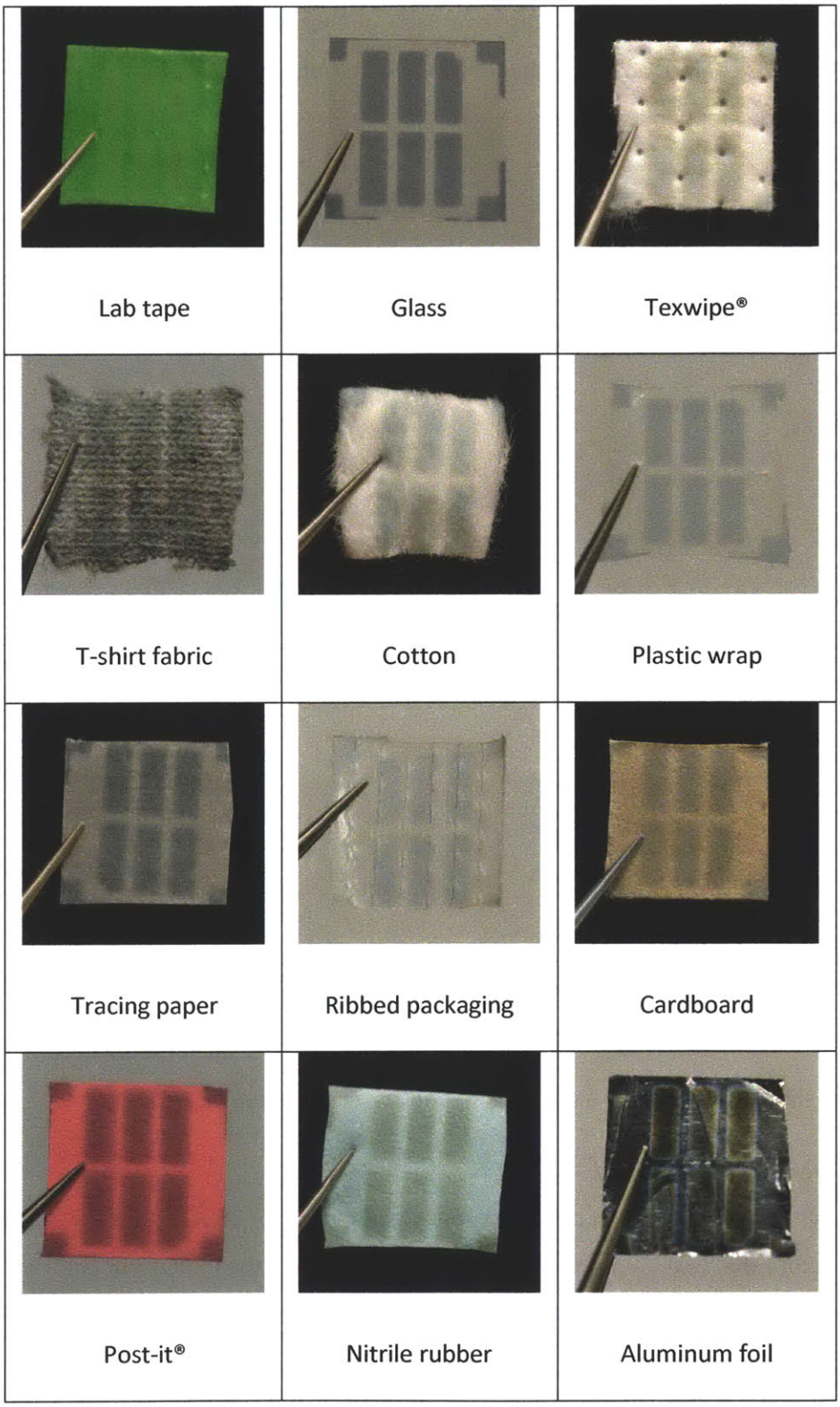

Figure 1-3: oCVD PEDOT patterned by shadow masking onto a wide variety of substrates. The identical procedure was utilized in each case, to demonstrate that the oCVD processes is substrate independent. On each sample, six 1.9 mm by 5.0 mm rectangles can be seen. The spacing between the rectangles is 0.70 mm.

Films can also be deposited on substrates regardless of their surface energy, for example Figure 1-4 shows oCVD PEDOT coated on a graphene film where solution processing is difficult due to the hydrophobicity of the graphene surface.

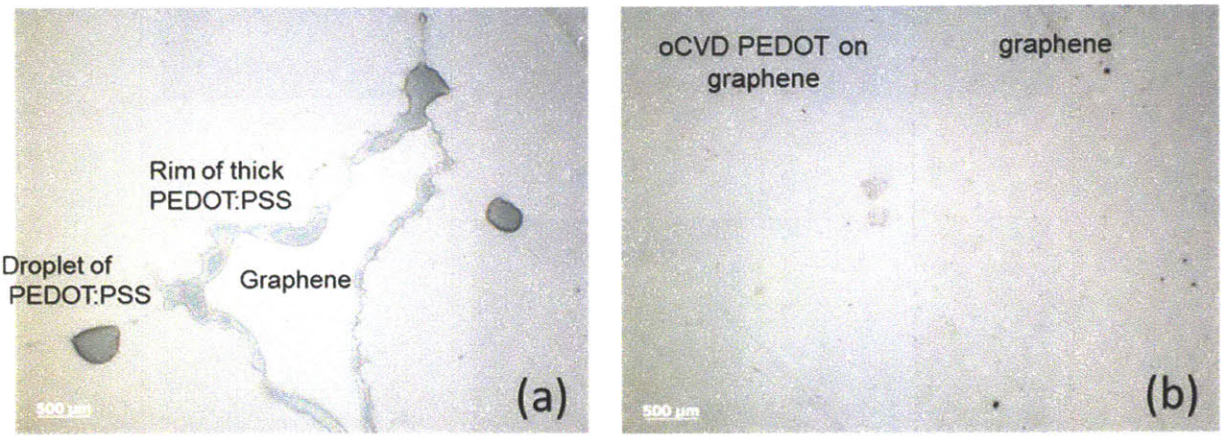

Figure 1-4: SEM images of (a) PEDOT:PSS and (b) oCVD PEDOT on graphene

The films can be put onto flexible or foldable materials (Figure 1-5) and retain their characteristics upon flexing.

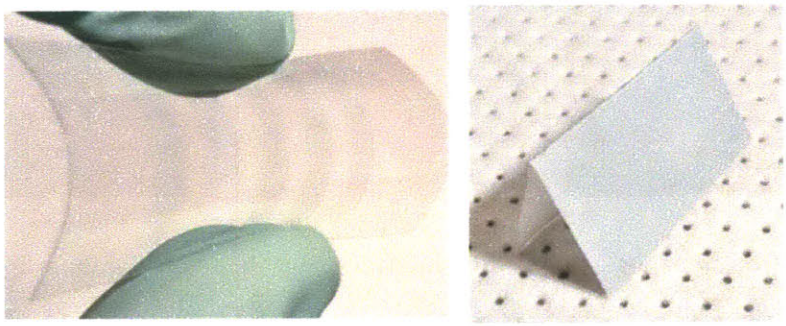

Figure 1-5: oCVD PEDOT patterned on PET substrate (left) and blanket deposited on paper (right)

1.2.3 PEDOT reaction chemistry

Figure 1-6 shows the oCVD reaction chemistry for the deposition of PEDOT using $FeCl_3$ as the oxidant. It is important to note that in this case the $FeCl_3$ is not only oxidizing the PEDOT but chlorine is also getting incorporated into the growing polymer chain as a dopant molecule. The maximum theoretical dopant concentration is approximately 1 in every 3 monomer units.[7-11]

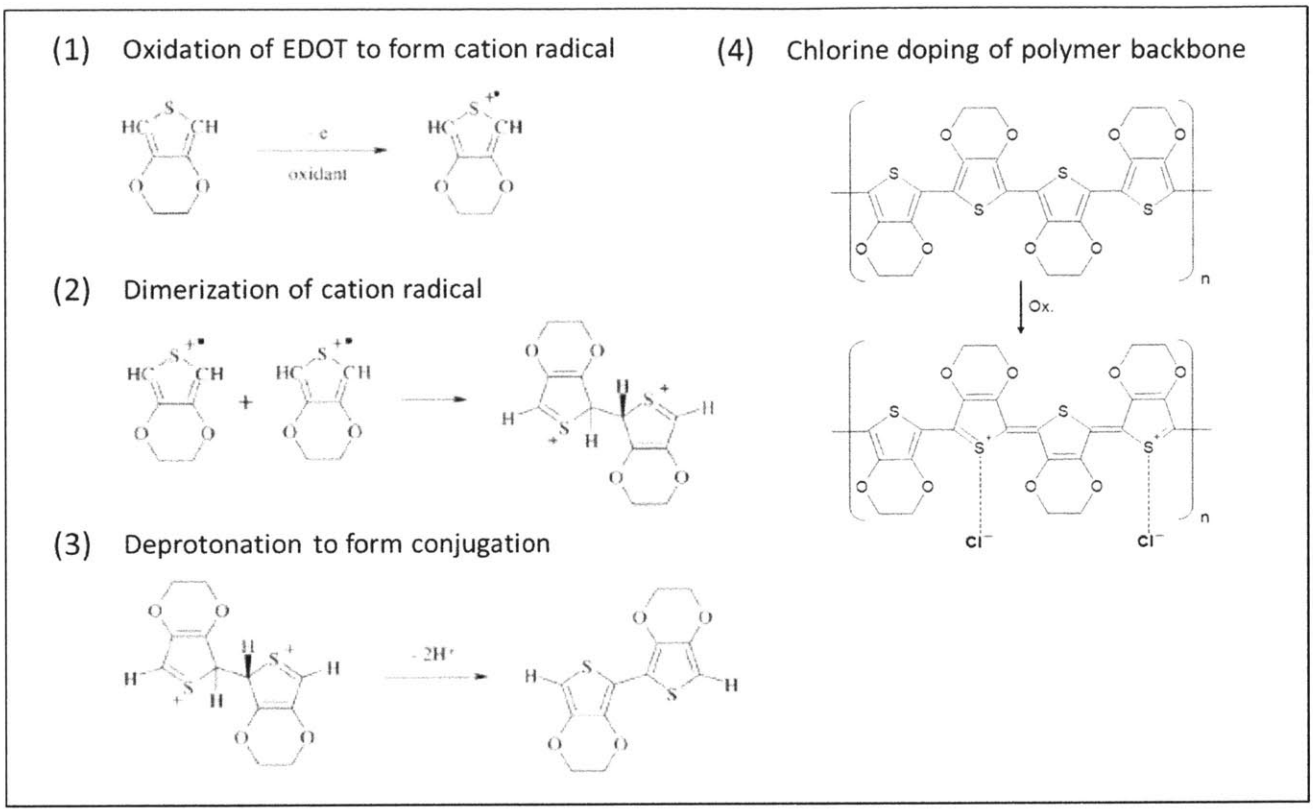

Figure 1-6: Proposed polymerization mechanism for oxidative polymerization of PEDOT (1) oxidation of EDOT to form cation radical; (2) dimerization of cation radicals; (3) deprotonation to form conjugation; (4) doping of the PEDOT chain

1.2.4 Reactor design

A new oCVD reactor was constructed to improve control over the process parameters, give more flexibility in creating new materials, and give more repeatable, higher quality polymer films. Figure 1-7 shows the design of the new oCVD chamber along with a description of the various systems.

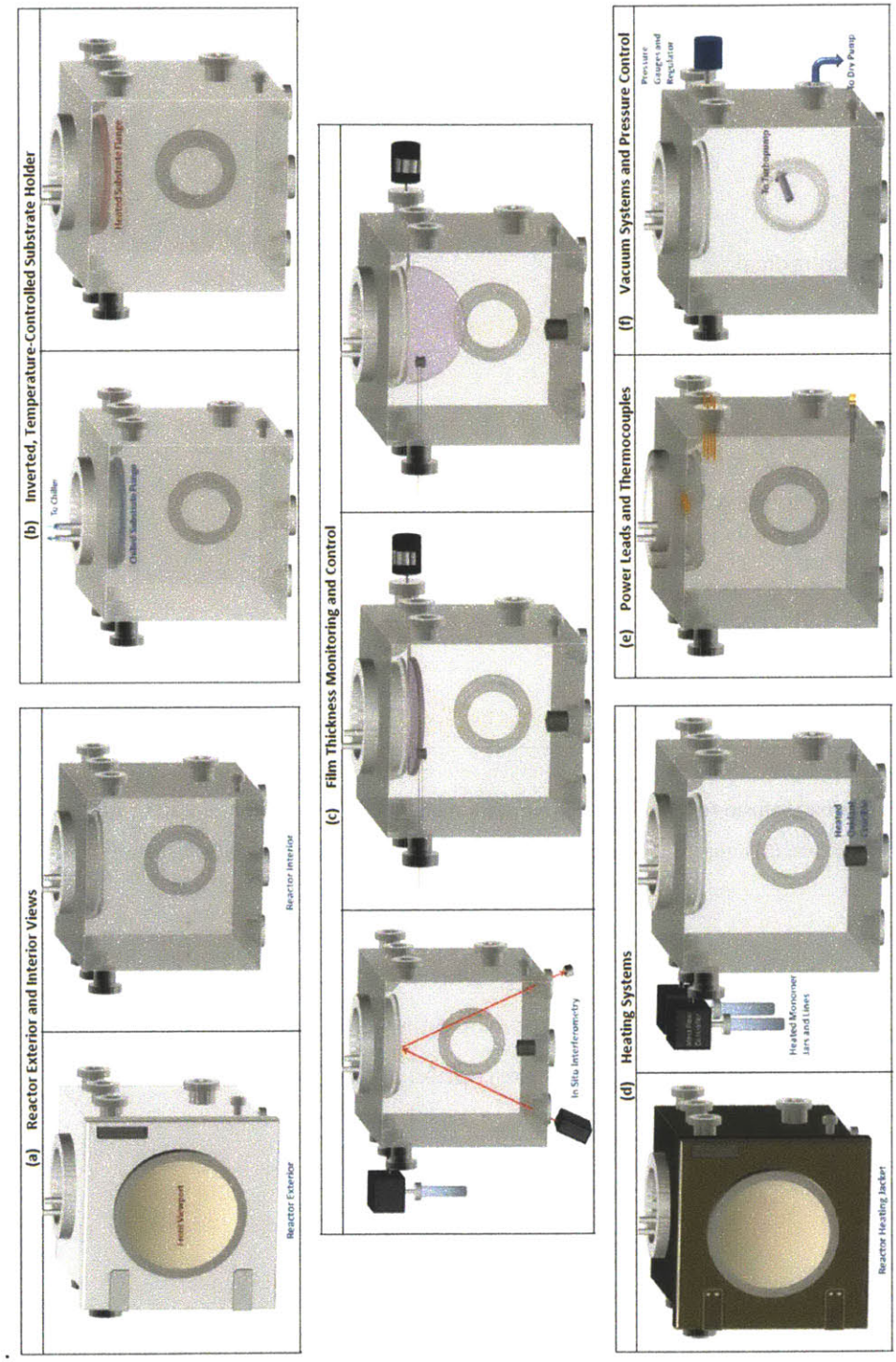

(a) A square chamber design allows for easy access for reactor cleaning and maintenance. The front glass viewport allows for monitoring of the deposition.

(b) A temperature-controlled flange allows for deposition over a wide temperature range (~10-200 °C)

(c) Angled glass viewports at the bottom of the chamber allow for in-situ interferometry measurements of film thickness. Alternatively, a quartz crystal microbalance (QCM) located near the substrate can be used to monitor thickness. The shutter can be opened or closed to time the delivery of oxidant to the substrate.

(d) An external custom heating jacket is used to control the temperature of the body of the reactor. Monomers are delivered to the main chamber through heated delivery lines using mass flow controllers. The oxidant may also be delivered through a heated external line, or directionally delivered by measuring into a heated oxidant crucible placed directly inside the chamber.

(e) Power leads and thermocouple feedthroughs are used to power and monitor components *inside* the reactor during deposition. (Other thermocouples used for external components)

(f) The chamber is connected to a dry roughing pump allowing the chamber to reach pressures of ~1e-2 Torr. A pressure regulator and throttle valve allows for control of the process pressure. The chamber is also connected to a turbopump which can be used to reach lower pressures of ~1e-7 Torr.

Figure 1-7: oCVD Reactor Systems

1.3 oCVD polymer use in photovoltaics

The benefit of using polymers in optoelectronic devices are their tunable features, good mechanical properties, and ability to be used with flexible substrate materials allowing for roll-to-roll processing.

The primary challenges are their lower stability and charge mobility in comparison to inorganic materials. Figure 1-8 shows the locations within a typical device stack where polymers are frequently considered for use.

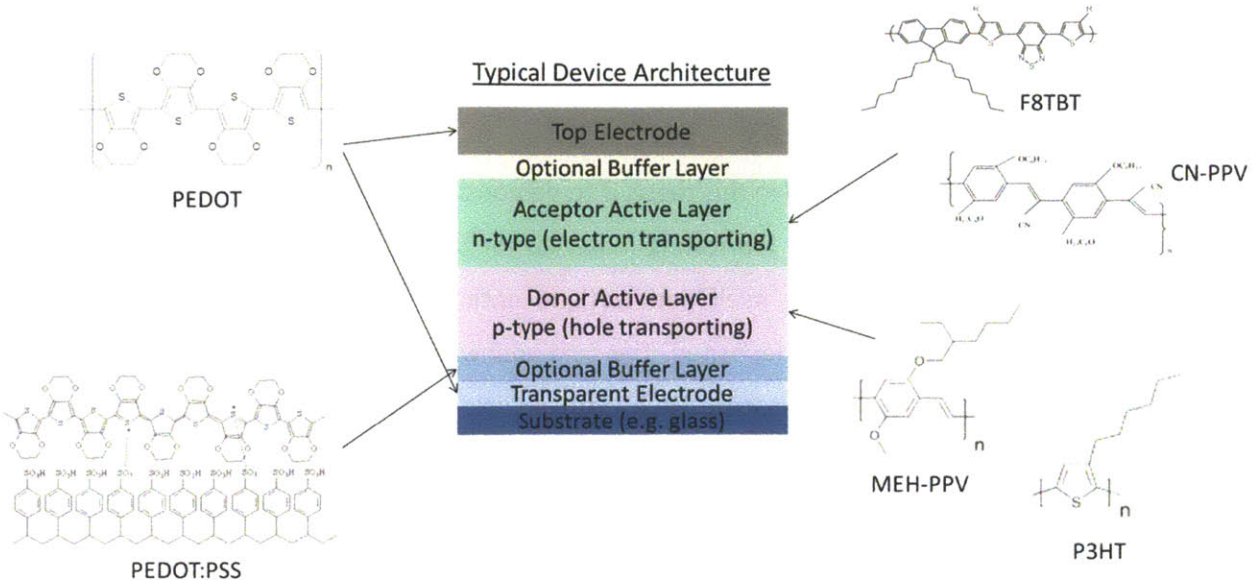

Figure 1-8: Locations within typical OPV device stack where polymer use is under investigation with example polymers pictured

Polymers are most commonly explored to act as the donor active layer within organic photovoltaics. They are also, less commonly, investigated for use as an n-type donor material. Another typical use for polymers in OPVs is as a buffer layer material (e.g. PEDOT:PSS as an HTL on ITO). Polymers, primarily PEDOT, have also been explored as a transparent electrode material, generally as the anode (due to the relatively high work function) but also as the cathode.[12]

1.4 Polymer electrodes

One of the primary motivations of this research is the desire to replace the most commonly used transparent conducting electrode material, ITO. There are several downsides to using ITO. For one, indium is a relatively scarce and expensive material and the cost is only going to continue to increase with the increased production of organic electronic devices.[13] ITO is also brittle, so unlike PEDOT, the sheet resistance of ITO films rapidly increases when flexed due to the formation of micro-cracks.[14] Researchers are exploring a number of alternative electrode materials including graphene,[15] carbon nanotubes,[16] metal grids or thin metal layers, [17] and polymer electrodes.

One of the primary benefits of investigating polymer electrodes is their ability to integrate with cheap, scalable large area processing methods such as various roll-to-roll techniques. Though polymers generally have lower conductivities than traditional metal oxide electrodes, polymer electrodes are compatible with lightweight, flexible substrates and have tunable properties.[18] This compatibility could make way for new OPV applications and novel device architectures.

1.5 Project goals/scope of thesis

The general goal of the work presented in this thesis is to demonstrate the oCVD process as a useful and interesting technique for studying and fabricating materials for use in organic electronic devices. One initial goal was to study the process itself and work to optimize the optoelectronic and physical properties of the polymer films being deposited. The next goal was to integrate the materials created using oCVD into organic photovoltaic devices. The hypothesis was that oCVD conductive polymers could be used in combination with novel electrode, active, and other functional layer materials to form conformal, well-tuned interfaces and allow for the construction of efficient and unique photovoltaic devices.

Chapter 2 discusses a technique for rinsing polymer films post-deposition to improve properties relevant to their integration into organic electronics. Instead of using the traditional rinsing solution, methanol, rinsing in hydrochloric, hydrobromic, and sulfuric acid is explored. The acid rinsing was found to decrease surface roughness, improve the relationship between transparency and conductivity, and increase stability. Thesis enhancements on the materials and processing side should directly translate to improvements in device performance when moving toward integration of oCVD materials into photovoltaics.

In Chapter 3, oCVD PEDOT is demonstrated as a buffer layer material in organic photovoltaics facilitating the use of a novel transparent electrode, graphene, to make ITO-free devices. The work shows the advantages of the oCVD process when working with substrates with difficult surface characteristics. Due to the hydrophobicity of the graphene surface, depositing a necessary buffer layer material was challenging by conventional methods, i.e. spin-coating and led to patchy uneven films, whereas the oCVD PEDOT provided complete coverage to act as a buffer material.

The work in Chapter 4 utilizes the oCVD process to go beyond the traditional PV cell architecture. oCVD PEDOT electrodes enabled the fabrication of inverted top-illuminated devices, a novel technique which

allows building devices on opaque substrates. These top illuminated devices had good performance in comparison to conventional architectures. The fabrication of devices on paper with an inverted structure led to a ten-fold increase in device efficiency over previously demonstrated paper devices.

In Chapter 5 optimization techniques for various PEDOT film synthesis processes are discussed. Conductivity enhancement methods for solution-processed and vapor-processed films are summarized and related to oCVD. Several recommendations are given for further research into optimizing oCVD PEDOT film conductivity and morphology.

Chapter 6 details research that was completed on textured and nonplanar substrates, which took advantage of the conformal oCVD process to go beyond traditional planar architectures to enhance light trapping.

Through these various works, oCVD was demonstrated as an important tool for the design and production of future photovoltaic devices and worthy of further research efforts.

Appendix A details work completed during the Ph.D. thesis not relevant to the core research topic. The first all carbon photovoltaics were developed using single chirality single-wall carbon nanotubes (SWNTs) as the donor absorber layer.

Appendix B contains detailed engineering drawings of the oCVD reactor chamber.

1.6 References

1. *Annual Energy Review*, Energy Information Administration, 2008.
2. H. Hoppe and N. S. Sariciftci, *Journal of Materials Research*, 2004, **19**, 1924-1945.
3. W. E. Tenhaeff and K. K. Gleason, *Advanced Functional Materials*, 2008, **18**, 979-992.
4. S. Vaddiraju, K. Senecal and K. K. Gleason, *Advanced Functional Materials*, 2008, **18**, 1929-1938.
5. C. Wadia, A. P. Alivisatos and D. M. Kammen, *Environmental Scienc & Technology*, 2009, **43**, 2072-2077.
6. D. Bhattacharyya, R. M. Howden, D. C. Borrelli and K. K. Gleason, *Journal of Polymer Science B: Polymer Physics*, 2012.
7. A. Elschner, S. Kirchmeyer, W. Lovenich, U. Merker and K. Reuter, *PEDOT: Principles and Applications of an Intrinsically Conductive Polymer*, CRC Press, Boca Raton, FL, 2011.
8. H. Randriamahazaka, V. Noel and C. Chevrot, *Journal of Electroanalytical Chemistry*, 1999, **472**, 103-111.
9. J. Hwang, D. B. Tanner, I. Schwendeman and J. R. Reynolds, *Physical Review B*, 2003, **67**, 115205.
10. G. Zotti, S. Zecchin, G. Schiavon, F. Louwet, L. Groenendaal, X. Crispin, W. Osikowicz, W. Salaneck and M. Fahlman, *Macromolecules*, 2003, **36**, 3337-3344.
11. K. E. Aasmundtveit, E. J. Samuelsen, L. A. A. Pettersson, O. Inganäs, T. Johansson and R. Feidenhans'l, *Synthetic Metals*, 1999, **101**, 561-564.

12. D. Bhattacharyya, R. M. Howden, D. Borrelli and K. K. Gleason, *Journal of Polymer Science B: Polymer Physics*, 2012, **50**, 1329-1351.
13. R. G. Gordon, *MRS Bulletin*, 2000, **25**, 52-57.
14. M. C. Barr, J. A. Rowehl, R. R. Lunt, J. Xu, A. Wang, C. M. Boyce, S. G. Im, V. Bulovic and K. K. Gleason, *Advanced Materials*, 2011, **23**, 3500-3505.
15. Y. Wang, X. Chen, Y. Zhong, F. Zhu and K. P. Loh, *Applied Physics Letters*, 2009, **95**, 063302-063303.
16. A. D. Pasquier, H. E. Unalan, A. Kanwal, S. Miller and M. Chhowalla, *Applied Physics Letters*, 2005, **87**, 203511-203513.
17. M. G. Kang and L. J. Guo, *Advanced Materials*, 2007, **19**, 1391-+.
18. S. G. Im, K. K. Gleason and E. A. Olivetti, *Applied Physics Letters*, 2007, **90**, 152112.

CHAPTER TWO

Acid rinse dopant exchange for enhanced PEDOT conductivity, stability, and surface roughness

The work described in this chapter has been published in *The Journal of Materials Chemistry: A*[1]

2.1 Abstract

Reduced sheet resistance and longer film stability of oCVD (oxidative chemical vapor deposition) PEDOT films were achieved by including a post-process acid rinse step in the production of the thin films. PEDOT films were rinsed in multiple concentrations of hydrobromic acid, sulfuric acid, and hydrochloric acid to test the effect of acid rinsing on sheet resistance, doping concentration, chemical composition, optical transmittance, and film morphology. XPS, FTIR, Raman spectroscopy, and XRD measurements were taken to determine the morphology and composition of the rinsed films. On average, rinsing films in HCl, HBr, and H_2SO_4 produced conductivity increases of 37%, 135%, and 117%. The dc to optical conductivity ratio, σ_{dc}/σ_{op}, was increased to 6, 12, and 10, for HCl, HBr, and H_2SO_4 rinsed films respectively as compared to σ_{dc}/σ_{op} = 4 for MeOH rinsed films. This study found evidence of dopant exchange within the films facilitated by the acid rinsing step, as well as complete removal of residual iron chloride oxidant. The acid rinse step also resulted in improved film conductivity stability at elevated temperatures. The XRD measurements in particular show signs of semi crystallinity in the PEDOT film after acid rinsing in comparison to an amorphous structure observed before this step. In this study, acid rinsing applied as a post-process step alters thin PEDOT films in ways that enhance their ability to function as electrode materials in photovoltaic devices.

2.2 Introduction

Organic optoelectronic devices, such as organic light emitting diodes (OLEDs) and organic photovoltaics (OPVs), require the use of one or more transparent electrode materials. The most commonly used transparent electrode material, indium tin oxide (ITO), has many limitations including high cost, poor electrical properties, brittleness, and high processing temperatures, making it an unsuitable choice for several applications.[2] Researchers are investigating several alternative materials such as graphene,[3] carbon nanotubes,[4] thin metal layers or metal nanowires,[5] as well as conductive polymer electrodes. Polymer electrodes offer a promising alternative to ITO or other electrode and buffer layer materials due to their low cost and ability to be used with lightweight, flexible substrates.[6] Oxidative chemical vapor deposition (oCVD) has emerged as a promising technology for creating conducting and semiconducting conjugated polymers for application in photovoltaics.[6] The dry, relatively low-temperature process allows polymer films to be grown on virtually any substrate.[7, 8] The most important parameters for a transparent electrode material are stability and the trade-off between transparency and sheet resistance. Polymer electrodes still suffer in comparison to traditional metal-oxide transparent electrodes because of their lower sheet resistance.[6]

Pre- and post-processing techniques can have a significant impact on the film's final electrical and physical properties. Vapor deposited conductive polymers are often rinsed with ethanol or methanol to remove residual iron chloride and unreacted monomer from the film, though these rinses are often unsuccessful at fully removing all of the excess oxidant.[8, 9] Post-deposition chemical rinsing can also be used to perform dopant exchange, change film morphology, tune the work function, or improve the film sheet resistance.[10] One such rinsing treatment that can be conducted is immersing the films in acidic or basic solutions.

Researchers using a similar polymerization technique, vapor phase polymerization (VPP) found that rinsing PEDOT films in solutions of alternating pH they could reversibly cycle the conductivity as well as use acid to recover the conductivity of films stored in air for over a year.[11] Xia et al. demonstrated rinsing in H_2SO_4 as a method for enhancing solution processed PEDOT:PSS, in which the improved conductivity was a result of film thinning and optimized morphology.[12] Acid rinsing is hypothesized to have multiple potential effects on vapor-deposited PEDOT films including fully removing residual reacted and unreacted oxidant from the film, provide a solvating effect allowing dopant ions to be incorporated into the conjugated chain, and lower film roughness.

The work presented here demonstrates that for oCVD PEDOT films using an acid rinsing step before rinsing in methanol can increase the conductivity of the films from 37% - 135% (in comparison to films rinsed only in methanol) and result in longer film stability. These "cleaner," more conductive films can provide a superior electrode material on which to build photovoltaic devices.

2.3 Experimental

Film preparation and rinsing

Glass and silicon substrates were cleaned by sequential sonication in acetone, deionized water, and isopropyl alcohol, followed by 30 second of oxygen plasma treatment. The PEDOT films were synthesized by oxidative chemical vapor deposition, described in more detail elsewhere.[13] In short, glass and silicon substrates were simultaneously exposed to vapors of 3,4-ethylenedioxythiophene (EDOT) monomer (Aldrich 97%) metered at ~5 sccm and $FeCl_3$ oxidant (Sigma Aldrich, 99.99%) controllably evaporated from a crucible resistively heated from 100-180 °C at a constant heating rate of 1.5 °C min^{-1} For each comparison across rinsing conditions all samples were used from a single deposition. Process conditions were held the same across all depositions (chamber pressure ~0.1 mTorr, substrate temperature = 150 °C). Run time was varied to create films of different thicknesses. Hydrochloric acid

(HCl) (Aldrich 37%), hydrobromic acid (HBr) (Aldrich 48%), and sulfuric acid (H_2SO_4) (Aldrich 98%) were diluted with deionized H_2O to make rinsing solutions ranging from 0.01 - 5 mol L^{-1}. With the exception of experiments investigating acid rinse concentration and time, films were rinsed for 5 minutes in acid followed by drying for 30 minutes before a final rinse in MeOH. All rinsing and drying steps were done in ambient conditions.

Characterization

XPS and XRD were performed at the Cornell Center for Materials Research (CCMR). XPS depth profiling was done at a speed of ~10 nm min^{-1}. UV-Vis was performed using a Cary 5000 over a wavelength range of 200-2000 nm. FTIR was performed on a Nexus 870 FT-IR ESP. Raman spectroscopy was performed on a Horiba HR800 using a 784.399 nm laser. Roughness data was collected using tapping mode AFM (Agilent Technologies) over 1 μm and 10 μm square scans. Film sheet resistance was measured using a Jandel 4-pt probe. Averages were calculated over 10 point measurements. Film thicknesses were measured using a Dektak profilometer. Average values were taken over 10 line scans.

2.4 Results and Discussion

Rinse Conditions

The films obtained directly from the oCVD process are doped with a combination of (Cl^-) and ($FeCl_4^-$) anions. Hydrochloric acid (HCl), hydrobromic acid (HBr), and sulfuric acid (H_2SO_4) were selected for investigation since they have anions that have been previously demonstrated as a dopant with PEDOT films. Figure 2-1a shows a schematic of the deposition and rinsing process used to prepare samples for characterization.

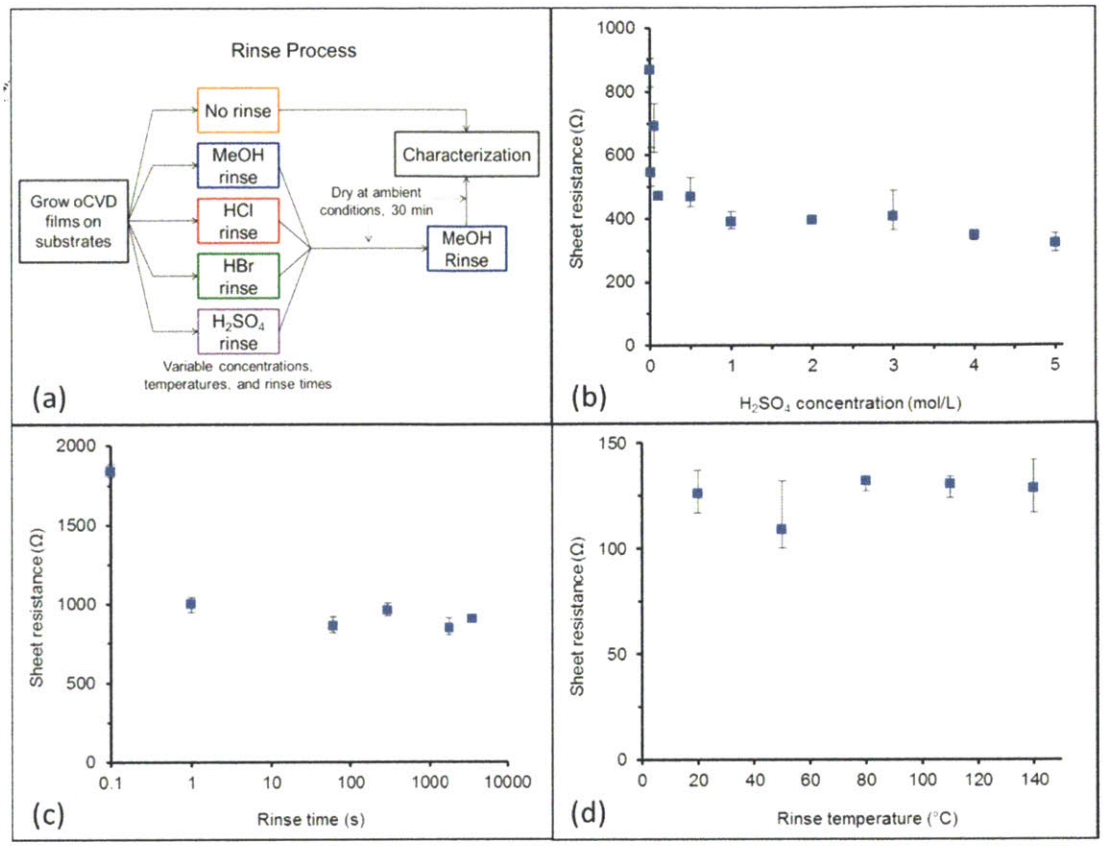

Figure 2-1:(a) Schematic of rinsing process for oCVD PEDOT samples prepared for characterization (b) Representative graph of relationship between PEDOT sheet resistance (R_{sh}) and acid concentration for 25 nm samples rinsed in H_2SO_4 (c) Representative log-scale plot of PEDOT R_{sh} with increasing rinse time for 15 nm samples rinsed in 1 M H_2SO_4 (d) Representative graph of PEDOT R_{sh} with varying rinse temperature for 100 nm films rinsed in 1 M H_2SO_4. Error bars on the graphs represent the spread in R_{sh} values from the 4-pt probe measurements.

Over 20 trials on PEDOT films of varying thickness, average conductivity increases of 37%, 135%, and 117% were seen for HCl, HBr, and H_2SO_4 rinsed films, respectively, in comparison to MeOH rinsed films with a maximum observed conductivity of 1620 S cm^{-1}. The full table of initial and final conductivity values can be seen in

Table 2-1.

Table 2-1: Full table of conductivity values for acid-rinsed PEDOT films

	Sheet Resistance (Ω)					Thickness (nm)					Conductivity (S/cm)				
Set#	NR	MeOH	HCl	HBr	H_2SO_4	NR	MeOH	HCl	HBr	H_2SO_4	NR	MeOH	HCl	HBr	H_2SO_4
1	1260	1450	1150	814	923	15	9	10	9	8	529	750	911	1331	1282
2	11370	14400	15780	8500	10500	6	4	3	4	3	147	194	190	326	277
3	10690	32100	14100	10880	14020	5	3	3	3	3	187	101	220	280	258
4	991	1930	1300	777	563	18	10	11	11	12	561	496	679	1162	1511
5	929	1000	1100	443	441	25	14	16	14	16	431	730	585	1620	1425
6	883	883	693	336	383	33	22	20	21	21	343	523	710	1389	1245
7	186	211	134	85	99	124	78	69	81	79	434	609	1079	1456	1281
8	307	355	267	103	134	106	69	66	65	62	307	411	564	1484	1198

9	472	453	305	170	200	104	63	63	66	65	204	348	523	888	775
10	200	224	142	87	93	130	78	81	84	82	385	572	874	1367	1309
11	128	140	88	43	49	235	149	133	155	144	332	478	854	1502	1421
12	200	169	135	67	74	213	129	139	129	133	235	459	533	1155	1014
13	253	306	174	145	144	102	61	59	57	57	388	534	981	1204	1224
14	914	1100	899	597	603	38	21	24	21	22	288	433	464	816	746
15	570	556	490	203	227	57	37	37	36	36	308	483	549	1365	1228
16	800	888	722	552	608	39	25	25	24	24	321	455	546	740	676
17	8761	9020	7325	4488	5000	8	5	5	5	5	143	241	267	439	415
18	13030	13239	11562	7634	8059	7	4	4	4	4	110	173	206	299	292
19	12489	11100	8333	5884	6128	10	6	5	6	6	83	144	227	285	277
20	136	144	107	53	65	197	119	128	119	122	373	584	730	1590	1258

The reduction in sheet resistance observed after performing acid rinsing on the vapor deposited films occurs rapidly and is not highly dependent on the rinsing solution temperature or concentration, Figure 2-1b-d. The rapid reduction of sheet resistance with increasing rinse time and concentration was observed even for thicker films (>100 nm). The speed with which the change occurs and the ability to significantly lower the film sheet resistance even at low acid concentrations (< 0.5 mol L^{-1}) are beneficial parameters for a potential scaled up process.

XPS

X-ray photoelectron spectroscopy (XPS) spectra are shown in Figure 2-2 comparing an unrinsed film to samples rinsed in MeOH and the three acid solutions.

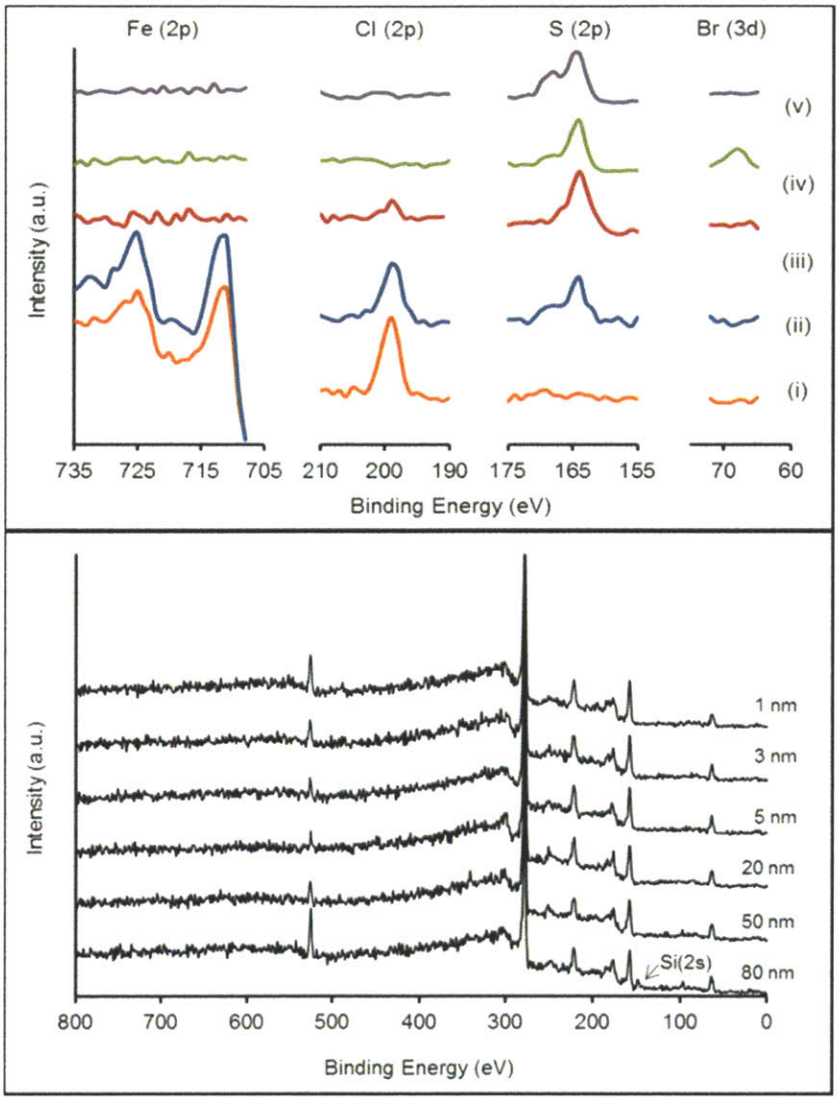

Figure 2-2: (a) X-ray photoelectron spectroscopy (XPS) survey scan of (i) unrinsed (ii) MeOH rinsed (iii) 1 M HCl rinsed (iv) 1 M HBr rinsed and (v) 1 M H_2SO_4 rinsed PEDOT samples on glass comparing regions of interest Fe(2p), Cl(2p), S(2p), and Br(3d). (b) XPS depth profiling on 1 M HBr rinsed sample from 1-80 nm.

The XPS analysis shows that the residual iron chloride is successfully removed for all three acid rinsing treatments, whereas the MeOH rinse leaves a majority of the iron chloride left in the film, as indicated by the Fe (2p) peak. The iron chloride forms hydration complexes with the water (Equation 1) and dissociates (Equation 2).[14] The low pH of the acidic solutions enhances the solubility of ferric materials and provides a stable environment for both +2 and +3 Fe compounds. The removed oxidant compounds can be visually observed in the residual rinsing solution by the yellow color arising from a ligand-to-metal charge-transfer (LMCT) band of $\mathrm{FeOH(H_2O)_5^{2+}}$.

$$FeCl_3 + 6H_2O \rightarrow Fe(H_2O)_6^{3+} + 3Cl^- \quad (1)$$

$$Fe(H_2O)_6^{3+} + H_2O \rightarrow FeOH(H_2O)_5^{2+} + H_3O^+ \quad (2)$$

The XPS analysis also indicates a dopant exchange occurring for the HBr and H_2SO_4 rinsed films. For both, the intensity of the chlorine peak, Cl (2p), goes to zero. Additionally, a Br (3d) peak appears for the HBr rinsed film, and the S (2p) forms a double peak corresponding to sulfate doping for the H_2SO_4 rinsed film. This exchange process is driven by the excess of the new dopant anion in the rinse solution and the system reaching equilibrium with the doped polymer chains (e.g. Equation 3, where EDOT represents a doped monomer unit).

$$H^+Br^- + EDOT^+Cl^- \rightleftharpoons H^+Cl^- + EDOT^+Br^- \quad (3)$$

Figure 2-2b shows XPS depth profiling of a film rinsed with HBr. The profile scans show no presence of iron or chlorine in the rinsed film through the entirety of the film thickness, as the appearance of a Si (2p) peak in the bottom curves indicates the analysis has reached the substrate surface. The presence of the Br (3d) peak through the film also indicates that the dopant exchange occurred throughout the film. The average atomic % ratio of Br to S throughout the HBr rinsed film is 0.3, which amounts to doping of approximately one in every three monomer units (the theoretical limit for PEDOT:PSS).[15, 16] As a note, films rinsed in pure DI water did not show an improvement in conductivity and the rinse did not remove the residual oxidant.

Morphology

Rinsing the samples has a significant impact on the film surface. Table 2-2 shows the roughness of the films after different rinsing conditions, as measured by AFM.

Table 2-2: AFM roughness data (†Sa is the average surface roughness, ‡Sq is the root-mean-square roughness)

Rinse condition	†Sa (nm)	‡Sq (nm)
unrinsed	56.3	77.4
MeOH	7.38	18.1
HCl (0.5 M)	4.54	5.55
HBr (0.5 M)	2.83	3.69
H_2SO_4 (0.5 M)	3.42	5.35

As expected, the unrinsed and MeOH samples have the roughest surfaces, as they have the largest amount of unreacted oxidant remaining in the film. The acid rinsed films have significantly lower roughness, with the lowest being HBr. Having a low surface roughness is beneficial for polymer electrode applications, as the devices will be less likely to have issues with defects and short circuiting.

Figure 2-3 shows x-ray diffraction data for film's rinsed in MeOH, HCl, HBr, and H_2SO_4. The MeOH rinsed film is primarily amorphous, while the acid rinsed films show a larger broad peak at 2θ = 26.3°(corresponding to the [020] reflection)[17] indicating an increase in the film crystallinity. The increased peak intensity over the broad background signifies partial crystallinity where there exist some crystalline regions embedded in an amorphous matrix. The increase of this peak with increasing film conductivity has been demonstrated before for free-standing PEDOT:PSS films,[18] tosylate-doped PEDOT films oxidatively polymerized in various organic solvents,[19] and vapor-phase polymerized PEDOT nanofibers.[20] The higher degree of crystallinity is an indication of better inter-chain stacking, which should improve charge transport via chain hopping and therefore enhance film conductivity.

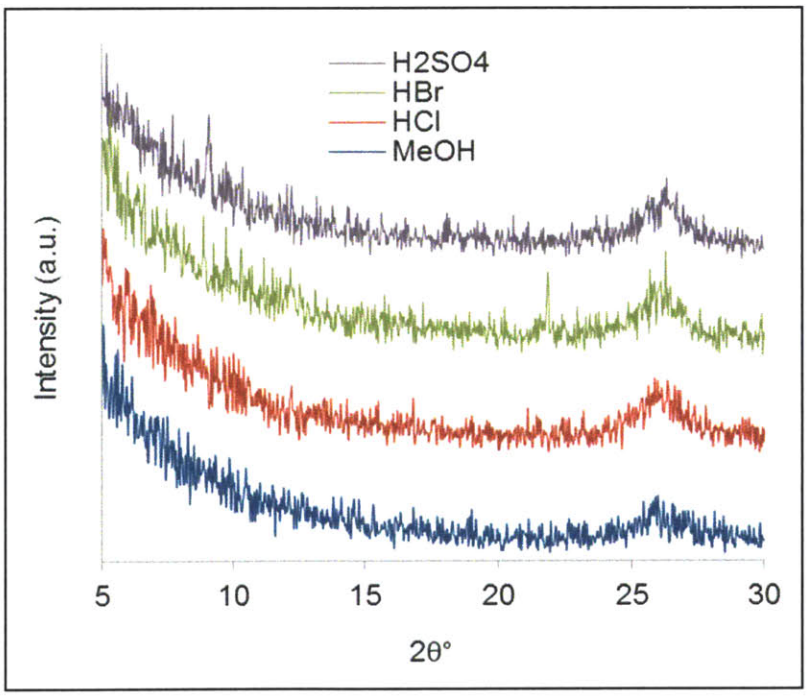

Figure 2-3: X-ray diffraction data for PEDOT films on silicon wafer substrates after different rinsing conditions: MeOH, 1 M HCl, 1 M HBr, and 1 M H_2SO_4

More work needs to be completed to fully understand the affect the rinsing has on the film morphology and on whether other parameters such as annealing or film drying conditions can have a significant impact.

FTIR

Figure 2-4 shows the Fourier transform infrared spectroscopy (FTIR) spectra for films after various rinsing treatments. The similarity between the resultant films suggests that the changes observed in the PEDOT sheet resistance is due to dopant and morphology affects rather than significant structural bond changes, such as increased conjugation length.

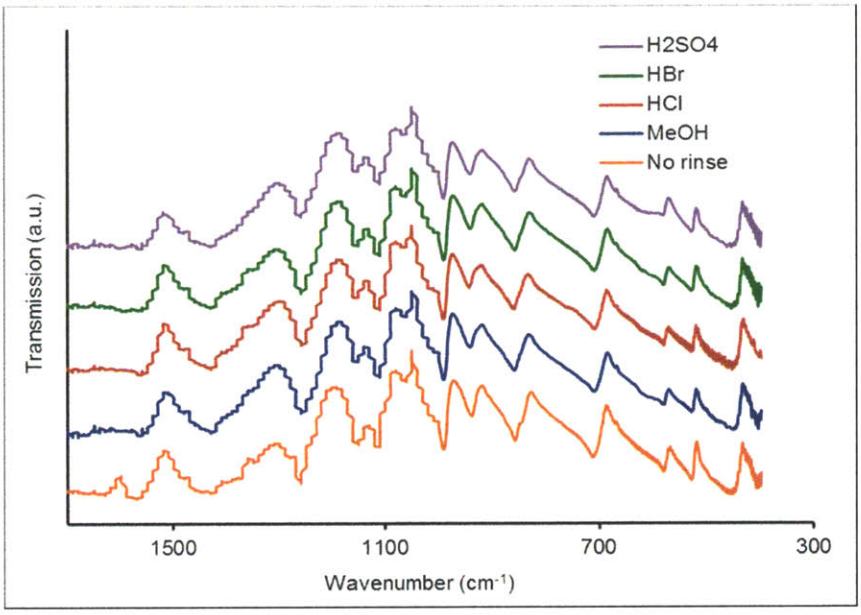

Figure 2-4: Fourier transform infrared spectroscopy (FTIR) spectra of films after different rinsing conditions: unrinsed, MeOH, 1 M HCl, 1 M HBr, and 1 M H_2SO_4.

Transmittance vs. Sheet Resistance

Figure 2-5a shows the tradeoff between transmittance (at 560 nm) and sheet resistance for films after different rinsing conditions. The data points represent experimental data and the solid lines are fit to the following equation relating transmittance (T) and sheet resistance (R_{sh}):

$$T = \left(1 + \frac{Z_0}{2R_{sh}} \frac{\sigma_{op}}{\sigma_{dc}}\right)^{-2}$$

Z_0 = 377 Ω is the impedance of free space and σ_{op} and σ_{dc} are the optical and dc conductivities, respectively. The standard industry value for transparent oxide conductors, such as indium tin oxide (ITO), is $\sigma_{dc}/\sigma_{op} > 35$. Figure 2-5b shows the % transmittance from 300-800 nm of a 15 nm PEDOT film after each rinsing condition. The unrinsed films, which appear cloudy over time, have the lowest

transmittance while the acid rinsed films have the highest transmittance. The increased transparency of the films after rinsing is primarily due to the removal of the light-absorbing Fe-species in the residual oxidant.[21] With decreasing sheet resistance for approximately the same transmittance values, the σ_{dc}/σ_{op} value increases from ~4 for the methanol rinsed films to ~6, 10, and 12 for the HCl, H_2SO_4, and HBr rinsed films, respectively.

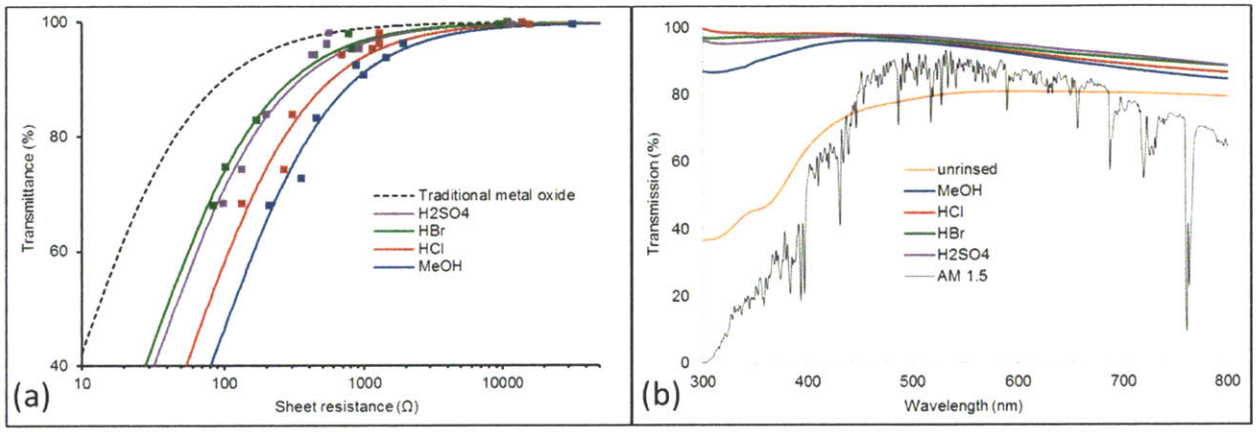

Figure 2-5: (a) Transmittance (550 nm) versus R_{sh} trade-off for rinsed PEDOT samples (MeOH, 2 M HCl, 2 M HBr, 2 M H_2SO_4). The solid lines are a fit to Equation (1) giving σ_{dc}/σ_{op}=4 for MeOH, 6 for HCl, 12 for HBr, and 10 for H_2SO_4 (the dashed black line is representative for traditional metal oxide electrodes, corresponding to σ_{dc}/σ_{op}=35). (b) UV-Vis spectra for 15 nm rinsed PEDOT samples. The black line is for reference and shows the AM1.5 solar spectrum.

Stability

Another important consideration for polymer electrode materials is the film stability. To accelerate film degradation, films were heated in air at various temperatures and measured over time for changes in conductivity. Figure 2-6a-c shows the changes in conductivity over a span of 48 hours at 30°C, 50°C, and 80°C.

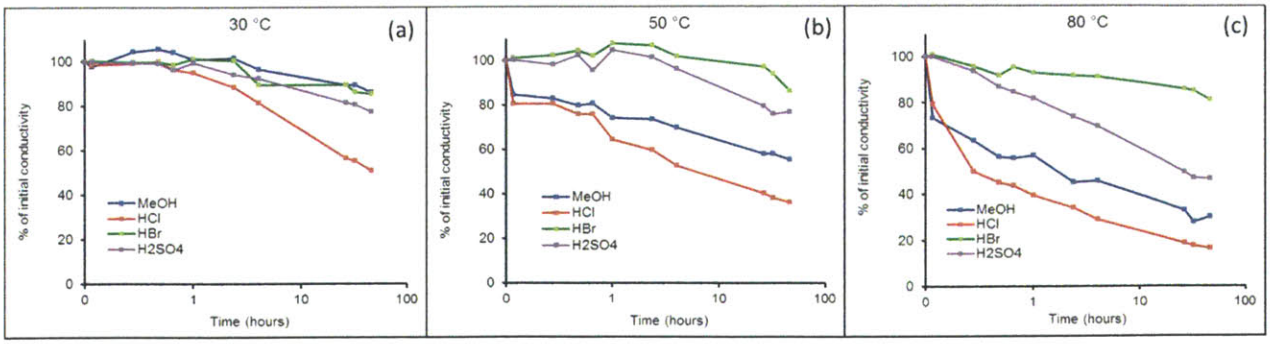

Figure 2-6: Stability of conductivity for films after different rinsing conditions at elevated temperatures (a) 30 °C (b) 50 °C (c) 80 °C.

For each temperature, the MeOH and HCl rinsed films show the fastest decrease in conductivity, while the HBr and H_2SO_4 films show the slowest losses. As expected, the rate of conductivity loss increases with increasing temperature. Previous work suggests that the size of the dopant molecules can have an impact on conductivity loss over time.[22] Researchers have shown that two primary mechanisms of PEDOT degradation are exposure to oxygen and water vapor.[23, 24] Shrinking conductive regions with increased heating over time has also been shown as a thermal degradation mechanism for PEDOT:PSS.[25] One possible explanation for the enhanced stability seen for the acid rinsed films is tighter chain packing, which would provide a better barrier to the atmosphere.[26] The removal of the excess oxidant, which is hygroscopic, could also reduce water content within the films. The size and reactivity of the dopant molecules likely play a role in the film degradation and conductivity loss over time as well. More work needs to be done to determine the exact mechanism(s) of thermal degradation and how the degradation relates to the specific counterions.

Raman Spectroscopy

The presence of chlorine in the reacted and unreacted oxidant left in the film for unrinsed and MeOH-rinsed films and the presence of sulfur in the polymer make it difficult to compare the degree of doping across films of different rinse conditions from the XPS data, so Raman spectroscopy was performed in hopes of revealing the shift in doping levels. Figure 2-7a shows the Raman spectra for the films after the different rinsing conditions. The intensity of the peak at 1259 cm^{-1}, corresponding to $C_\alpha = C_{\alpha'}$ inter-ring stretching, is slightly larger for the HBr and H_2SO_4 rinsed films indicating a quinoid structure. The intensity of the peak height at 1367 cm^{-1}, corresponding to $C_\beta–C_\beta$ stretching, is lower for the more conductive (HBr and H_2SO_4 rinsed) films, also suggesting stabilization of the quinoid structure. Zooming into the peak at 1420 cm^{-1}, Figure 2-7b, corresponding to the symmetric $C_\alpha = C_\beta$ stretching band, we can see broadening and right shifting for the films with lower sheet resistance (the HBr and H_2SO_4 rinsed samples). The right shift corresponds to a shift toward the doped state of PEDOT.[27] A similar shift has been observed in work that looked at enhancing pristine PEDOT:PSS by the addition of dimethyl sulfate (DMS) as the SO4-2 anions partially replaced PSS segments and the films conductivity increased. ENREF 17[28] As the doping level of a film increases, the shift towards higher wave numbers is explained by a shift toward a higher degree of doping. Authors Han et al. also observed a similar shift for their films at higher doping levels.[29] They attributed the shift to a higher wavenumber to the shortening of the conjugation length of the neutral polymer backbone upon further doping.

Figure 2-7c shows Raman spectra for the rinsed films before and after an accelerated aging experiment (heating at ambient conditions for 100 hours at 100 °C). With the decrease in film conductivity after aging, there is a corresponding left shift in the Raman spectra at the 1420 cm^{-1} $C_\alpha = C_\beta$ stretching peak toward the undoped state of PEDOT. Figure 2-7d shows the color change observed for the film rinsed in HCl, which underwent the largest, most rapid decrease in conductivity. The shift from blue to purple is similar to the shift observed when chemically reducing/dedoping PEDOT films.

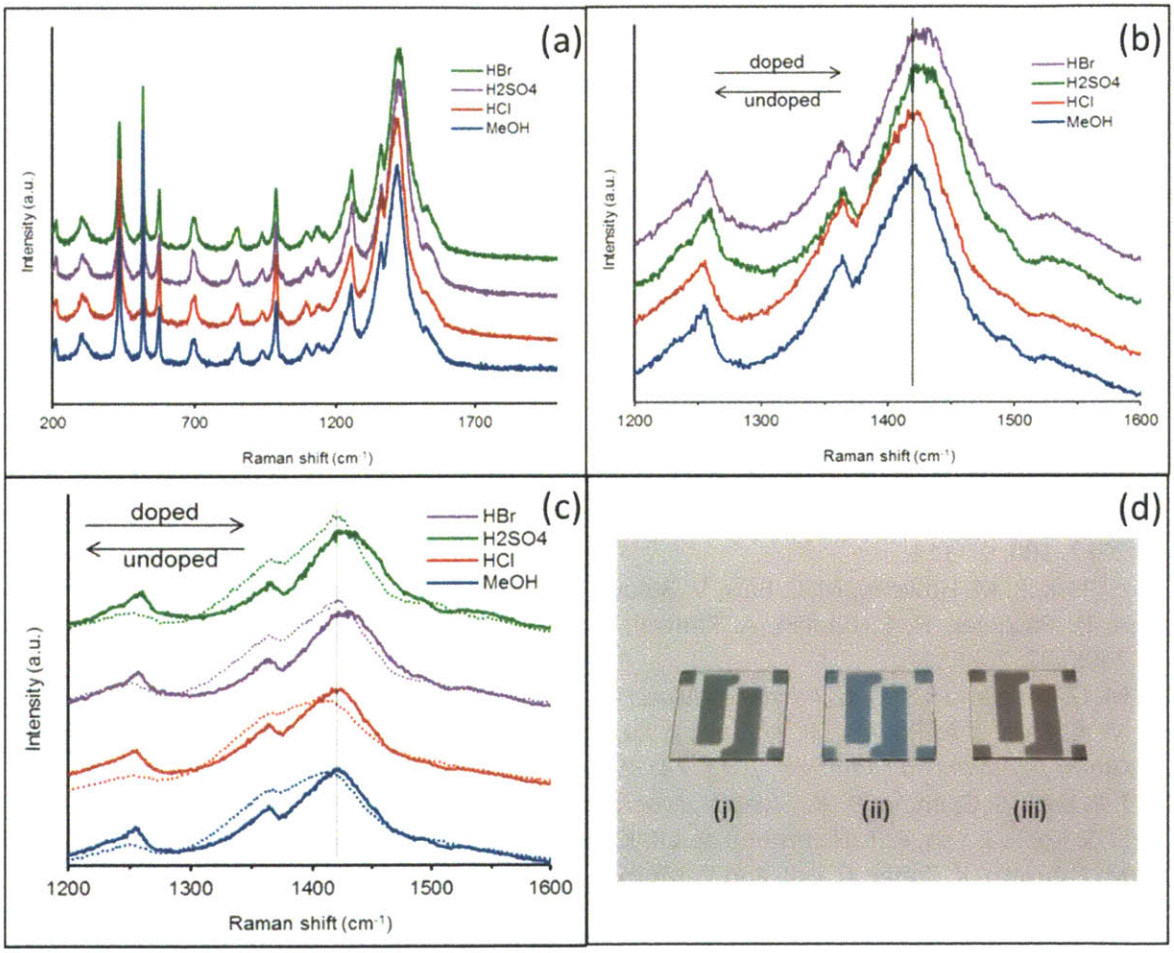

Figure 2-7: Raman spectra of films (pre-rinsed thickness 57 nm) after different rinsing conditions: MeOH, 1 M HCl, 1 M HBr, and 1 M H_2SO_4. (a) full spectra (b) spectra expanded around the 1420 cm^{-1} peak corresponding to symmetric $C_\alpha = C_\beta$ stretching. (c) Raman spectra for films before and after heating for 100 hours at 100 °C. The dotted lines (after heating) show the shift towards the neutral PEDOT state from the original doped state (d) photographs of thick patterned PEDOT films (i) unrinsed (ii) rinsed in 0.5 M HCl (iii) rinsed in 0.5 M HCl and heated for 175 hours at 100 °C.

2.5 Conclusion

It was demonstrated that rinsing oCVD polymerized PEDOT films in an acid solution can have many benefits on the film properties including lowering sheet resistance. The residual reacted and unreacted

oxidant, $FeCl_3$, is fully removed from the film which contributes to increased optical transmittance and lower film roughness. A dopant exchange occurs with the acid anions leading to a higher degree of doping and enhanced film stability. The best performance was observed for the HBr and H_2SO_4-rinsed films, which had the highest conductivities and highest film stabilities. The HCl-rinsed films showed an increase in film conductivity and a decrease in the film stability. These improvements to the film properties are useful for implementing oCVD polymer layers into optoelectronic device applications.

2.6 Acknowledgments

This research is supported in part by Eni S.p.A. under the Eni-MIT Alliance Solar Frontiers Program and by the Department of Energy Office of Science Graduate Fellowship Program (DOE SCGF), made possible in part by the American Recovery and Reinvestment Act of 2009, administered by ORISE-ORAU under contract no. DE-AC05-06OR23100. We thank Jonathan Shu from the Cornell Center for Materials Research (CCMR) for his help with XPS measurements.

2.7 References

1. R. M. Howden, E. D. McVay and K. K. Gleason, *Journal of Materials Chemistry A*, 2013, **1**, 1334-1340.
2. R. Po, C. Carbonera, A. Bernardi, F. Tinti and N. Camioni, *Solar Energy Materials & Solar Cells*, 2012, **100**, 97-114.
3. H. Park, R. M. Howden, M. C. Barr, V. Bulovic, K. Gleason and J. Kong, *ACS Nano*, 2012.
4. A. D. Pasquier, H. E. Unalan, A. Kanwal, S. Miller and M. Chhowalla, *Applied Physics Letters*, 2005, **87**, 203511.
5. M. G. Kang and L. J. Guo, *Advanced Materials*, 2007, **19**, 1391-1396.
6. M. C. Barr, J. A. Rowehl, R. R. Lunt, J. Xu, A. Wang, C. M. Boyce, S. G. Im, V. Bulovic and K. K. Gleason, *Advanced Materials*, 2011, **23**, 3500-3505.
7. J. P. Lock, S. G. Im and K. K. Gleason, *Macromolecules*, 2006, **39**, 5326-5329.
8. S. G. Im, P. J. Yoo, P. T. Hammond and K. K. Gleason, *Advanced Materials*, 2007, **19**, 2863-2867.
9. M. Fabretto, K. Zuber, C. Hall and P. Murphy, *Macromolecular Rapid Communications*, 2008, **29**, 1403-1409.
10. D. Bhattacharyya, R. M. Howden, D. C. Borrelli and K. K. Gleason, *Journal of Polymer Science B: Polymer Physics*, 2012.
11. B. Winther-Jensen and K. West, *Reactive & Functional Polymers*, 2006, **66**, 479-483.
12. Y. Xia, K. Sun and J. Ouyang, *Advanced Materials*, 2012, **24**, 2436-2440.
13. W. E. Tenhaeff and K. K. Gleason, *Advanced Functional Materials*, 2008, **18**, 979-992.
14. G. Hill and J. Holman, *Chemistry in Context*, 5 edn., Nelson Thornes, 2000.
15. A. Elschner, S. Kirchmeyer, W. Lovenich, U. Merker and K. Reuter, *PEDOT: Principles and Applications of an Intrinsically Conductive Polymer*, CRC Press, Boca Raton, FL, 2011.
16. J. Hwang, D. B. Tanner, I. Schwendeman and J. R. Reynolds, *Physical Review B*, 2003, **67**, 115205.
17. K. E. Aasmundtveit, E. J. Samuelsen, O. Inganas, L. A. A. Pettersson, T. Johansson and S. Ferrer, *Synthetic Metals*, 2000, **113**, 93-97.
18. S. Cho and K. Lee, *Journal of the Korean Physical Society*, 2005, **46**, 973-976.

19. T. Y. Kim, C. M. Park, J. E. Kim and K. S. Suh, *Synthetic Metals*, 2005, **149**, 169-174.
20. A. Laforgue and L. Robitaille, *Macromolecules*, 2010, **43**, 4194-4200.
21. D. M. Leeuw, P. A. Kraakman, P. F. G. Bongaerts, C. M. J. Mutsaers and D. B. M. Klaassen, *Synthetic Metals*, 1994, **66**, 263-273.
22. H. Chelawat, S. Vaddiraju and K. Gleason, *Chemistry of Materials*, 2010, **22**, 2864-2868.
23. K. Kawano, R. Pacios, D. Poplavskyy, J. Nelxon and D. D. C. Bradley, *Solar Energy Materials & Solar Cells*, 2006, **90**, 3520-3530.
24. K. Norrman, M. V. Madsen, S. A. Gevorgyan and F. C. Krebs, *Journal of the American Chemical Society*, 2010, **132**, 16883-16892.
25. E. Vitoratos, S. Sakkopoulos, E. Dalas, N. Paliatsas, D. Karageorgopoulos, F. Petraki, S. Kennou and S. A. Choulis, *Organic Electronics*, 2009, **10**, 61-66.
26. A. M. Nardes, M. Kemerink, M. M. de Kok, E. Vinken, K. Maturova and R. A. J. Janssen, *Organic Electronics*, 2008, **9**, 727-734.
27. W. W. Chiu, J. T. Sejdic, R. P. Cooney and G. A. Bowmaker, *Journal of Raman Spectroscopy*, 2006, **37**, 1354-1361.
28. M. Reyes-Reyes, I. Cruz-Cruz and L. Lopez-Sandoval, *Journal of Physical Chemistry C*, 2010, **114**, 20220-20224.
29. Y.-K. Han, M.-Y. Chang, W.-Y. Huang, H.-Y. Pan, K.-S. Ho, T.-H. Hsieh and S.-Y. Pan, *Journal of The Electrochemical Society*, 2011, **158**, K88-K93.

CHAPTER THREE

PEDOT hole transporting layers on graphene electrodes for ITO-free devices

The work described in this chapter has been published in *ACS Nano*[1]

3.1 Abstract

For the successful integration of graphene as a transparent conducting electrode in organic solar cells, proper energy level alignment at the interface between the graphene and the adjacent organic layer is critical. The role of a hole transporting layer (HTL) thus becomes more significant due to the generally lower work function of graphene compared to ITO. A commonly used HTL material with ITO anodes is poly(3, 4-ethylenedioxythiophene) (PEDOT) with poly(styrenesulfone) (PSS) as the solid state dopant. However, graphene's hydrophobic surface renders uniform coverage of PEDOT:PSS (aqueous solution) by spin-casting very challenging. Here, we introduce a novel, yet simple, vapor printing method for creating patterned HTL PEDOT layers directly onto the graphene surface. Vapor printing represents the implementation of shadow masking in combination with oxidative chemical vapor deposition (oCVD). The oCVD method was developed for the formation of blanket (i.e., unpatterened) layers of pure PEDOT (i.e. no PSS) with systematically variable work function. In the unmasked regions, vapor printing produces complete, uniform, smooth layers, of pure PEDOT over graphene. Graphene electrodes were synthesized under low pressure chemical vapor deposition (LPCVD) using a copper catalyst. The use of another electron donor material tetraphenyldibenzoperiflanthene (DBP) instead of copper phthalocyanine (CuPc) in the organic solar cells also improves the power conversion efficiency. With the vapor printed HTL, the devices using graphene electrodes yields comparable performances to the ITO reference devices ($\eta_{p,\,LPCVD}$ = 3.01%, and $\eta_{p,\,ITO}$ = 3.20%).

3.2 Introduction

Graphene is the hexagonal arrangement of carbon atoms forming a one-atom thick planar sheet. The successful isolation of single- and few- layer graphene by the mechanical cleaving of HOPG[2] has led to a significant increase in studies in numerous research areas. Of the many interesting properties of graphene (such as superior electron and hole mobility (up to 200,000 $cm^2 V^{-1} s^{-1}$),[3, 4] high current carrying capability (up to 3×10^8 A cm^{-2})[5]), its uniformly high transparency in the visible and near infrared region, with good electrical conductivity and mechanical robustness,[6], place graphene as a promising candidate for an alternative to indium tin oxide (ITO)[7] as a transparent conducting electrode (TCE).

Several criteria, such as electrical conductivity, optical transmittance, and work function (WF), need to be optimized for the integration of graphene sheets as TCEs in organic photovoltaics (OPV). Recent reports[8, 9] have already demonstrated that graphene has high transmittance with moderate conductivity. The most critical factor, however, is the energy level alignment between the work function of graphene and the highest occupied molecular orbital (HOMO) of the electron donor material. Bae et.

al.[9] reported a WF value of 4.27 eV (electron volts) for a monolayer of graphene synthesized from LPCVD, which is lower than for ITO (~4.5 eV and can be increased up to ~5.0 eV after oxygen (O_2) plasma treatment).[10, 11] This low value for graphene is obviously not a good match for the electron donor material considered in this work (tetraphenyldibenzoperiflanthene (DBP), HOMO = 5.5 eV),[12] as well as other common electron donor materials such as copper phthalocyanine (CuPc) (HOMO = 5.2 eV)[12] or poly(3-hexylthiophene) (P3HT) (HOMO = 5.2 eV),[13] which can induce a large energy barrier at the interface between the graphene and the organic layer.

For ITO anodes, a thin layer of conducting polymer, poly(3,4-ethylenedioxythiophene): poly(styrenesulfonate) (PEDOT:PSS), is commonly inserted before the deposition of the electron donor material in order to favor an ohmic-contact at the junction. The PEDOT:PSS hole transporting layer (HTL) with a WF of 5.2 eV not only facilitates the injection/extraction of holes but is also known to help planarize the rough surface of the ITO, which often becomes a possible source of local shorting through the ultra-thin active layers, thus improving the overall device performance.[14, 15] Therefore smooth and complete coverage of the PEDOT:PSS layer on the underlying electrode surface plays a crucial role in the general OPV device performance. Application of PEDOT:PSS onto the graphene surface has been challenging due to the fact that graphene surface is hydrophobic but PEDOT:PSS is in an aqueous solution. The sputtered ITO surface is also hydrophobic but it is almost always pretreated with O_2 plasma, which renders the hydrophobic surface into an hydrophilic one by introducing hydroxyl (OH) and carbonyl (C=O) groups[16] that enables conformal coverage of PEDOT:PSS. Active oxygen species from the plasma disrupt the aromatic rings of the graphene and greatly reduces the conductivity. In the case of single layer graphene electrodes, a graphene film can completely lose the conductivity after such plasma treatments.

Recently, Park et. al.[17] reported that the wettability of PEDOT:PSS on the graphene surface can be significantly improved by doping it with gold (III) chloride ($AuCl_3$). However, the doping process introduces large Au particles (up to 100 nm in diameter), which can create shorting pathways through the device. This method is less favorable also due to the high cost of $AuCl_3$ dopant. Wang et. al.[18] later reported using a molybdenum oxide (MoO_3) HTL with acid-doped graphene electrodes, which is a common HTL material used with ITO electrodes.[19] However, the device performance was not as efficient as the ITO control device with a MoO_3 layer alone and still required the use of PEDOT:PSS on top of the MoO_3 interfacial layer, which allowed better wetting of PEDOT:PSS on the MoO_3-coated graphene.

In this work, we introduce a novel, yet simple, HTL fabricated by vapor printing of PEDOT[20] directly onto the unmodified graphene surface. In a single step, vapor printing combines (i) the synthesis of conducting polymer chains from vapor-phase (3, 4 ethylenedioxythiophene) (EDOT) monomer, (ii) thin film formation of the PEDOT HTL, and (iii) patterning by in situ shadow masking. Vapor printing is derived from the oxidative chemical vapor deposition (oCVD) (steps (i) and (ii) only). The oCVD blanket (i.e., unpatterned) PEDOT layers readily integrate with a wide range of substrates, because it is a dry process and substrate temperature is mild (~120 °C), the difficulties with film dewetting and substrate degradation by solvents or high temperatures can be completely avoided.[20] In addition, the WF of the oCVD PEDOT layer can be tuned by controlling the doping level of Cl^- ions.[21] In this work, we have found that the oCVD process is also compatible with graphene substrates. The oCVD polymer layer is formed by directly exposing the substrate to vaporized monomer EDOT and an oxidizing agent (in this case, $FeCl_3$) under controlled reactor conditions. The relatively mild deposition conditions (low temperature 120 °C, moderate pressure ~10 mTorr, and no use of solvents) allow for PEDOT to be deposited without damaging or delaminating the graphene electrode. Furthermore, as vapor printing is generally substrate independent, requiring no substrate-specific optimization of the oCVD process or substrate pretreatment, thus it allows the direct printing of the PEDOT onto our graphene substrates. The graphene based solar cells fabricated with vapor printed PEDOT HTLs in this work achieve ~94% of the performance of their ITO counterparts without any additional treatment to the graphene sheets such as chemical doping.

3.3 Experimental

Graphene synthesis (LPCVD, APCVD)

Copper foil (25 μm in thickness, ALFA AESAR) was used as a metal catalyst for both conditions.

LPCVD – The CVD chamber was evacuated to a base pressure of 30-50 mTorr. The system was then heated to a growth temperature of 1000 °C under hydrogen (H_2, 10 sccm) gas (~320 mTorr) and annealed for 30 minutes. Subsequently, methane (CH_4, 20 sccm) gas was introduced (total pressure: ~810 mTorr) and graphene growth was carried out for 30 minutes. The chamber was then cooled down at ~45 °C/min to room temperature.

APCVD – The chamber was heated to 1000 °C under H_2 gas (170 sccm) and annealed for 30 minutes. After annealing, H_2 was reduced to 30 sccm and CH_4 (1 sccm) and Ar (1000 sccm) were additionally

introduced followed by 30 minutes of growth. After growth, the chamber was cooled at ~100 °C/min to room temperature. Both processes are schematically illustrated in Figure 3-2.

Graphene transfer and anode preparation

Transfer was carried out using poly(methyl methacrylate) (PMMA, 950 A9, Microchem). Graphene on one side of the foil was removed via reactive ion etching (RIE) with O_2 gas (Plasma-Therm, 100 Watt at 7×10^{-5} Torr). Cu was etched by a commercial etchant (CE-100, Transene). Graphene films were then thoroughly rinsed with diluted hydrochloric acid (10 %) and de-ionized (DI) water to remove residual iron ions from the Cu etchant. The PMMA layer was removed by annealing at 500 °C for 2 hours under H_2 (700 sccm) and Ar (400 sccm). Repeated transfers were performed for 3-layer graphene films. The transferred graphene films were patterned into the desired shape through RIE. The average sheet resistance (R_{sh}) and transmittance values of the graphene electrodes are ~300 Ω/sq and ~92% (at 550 nm).

Vapor Printed PEDOT

The oCVD reactor configuration and general process procedure are described elsewhere.[22] The oCVD PEDOT HTLs were all deposited under the same reaction conditions. The reactor pressure was held at ~10 mTorr and the substrate temperature was maintained at 120 °C. The monomer 3,4-ethylenedioxythiphene (Sigma Aldrich, 97%), EDOT, was used as purchased. The EDOT was heated to 140 °C and introduced into the reactor at a flow rate of ~5 sccm. Iron (III) chloride (Sigma Aldrich, 99.99%) was evaporated from a heated crucible between 130-160 °C. Different thicknesses were achieved by varying the time of reaction (1, 2, 4, and 8 minutes respectively to get HTL thicknesses of 2, 7, 15, and 40 nm). (PEDOT:PSS (Clevios™ P VP AI 4083) was filtered (0.45 μm), spin-coated at 4000 rpm for 60 seconds, and annealed at 210 °C for 5 minutes in air). The PEDOT was patterned using a pre-cut metal shadow mask with the same dimensions as the graphene electrode. The mask was visually aligned such that the PEDOT was deposited directly on top of the graphene.

OPV device fabrication process

Organic layers (DBP (Luminescence Technology Corp., >99%), C_{60} (Sigma Aldrich, 99.9%), BCP (Luminescence Technology Corp., >99%)) and top cathode (Al (Alfa Aesar, 3.175 mm slug, 99.999%)) were thermally evaporated through shadow masks at a base pressure of 1×10^{-6} Torr at rates of 1.0 Å/s

and 1.5 Å/s, respectively. C_{60} was purified once via thermal gradient sublimation before use. DBP, BCP, and Al were used as received. Pre-patterned ITO (Thin Film Devices, 20 Ω/sq) substrates were cleaned by solvents followed by 30 seconds of O_2 plasma (100 W, Plasma Preen, Inc.). Patterned graphene substrates were cleaned by annealing at 500 °C for 30 minutes under H_2 (700 sccm) and Ar (400 sccm). The device area defined by the opening of the shadow mask was 1.21 mm^2.

Measurements

The surface morphology of graphene sheet was characterized by AFM (Dimension 3100, Veeco) and the transmittance was measured from the UV-Vis_NIR spectrometer (Cary 5000, Varian). Work function measurements were performed using a SKP5050 Kelvin probe system from Kelvin Technology Inc. with analysis taken at various locations on each sample with 50 measurements collected per location (using 30 point averaging). Current-voltage measurements were recorded by a Keithley 6487 picoammeter in nitrogen atmosphere. 100 mW cm^{-2} illumination was provided by 150 W xenon arc-lamp (Newport 96000) filtered by an AM 1.5G filter. Figure 3-1a illustrates the graphene synthesis and transfer process.

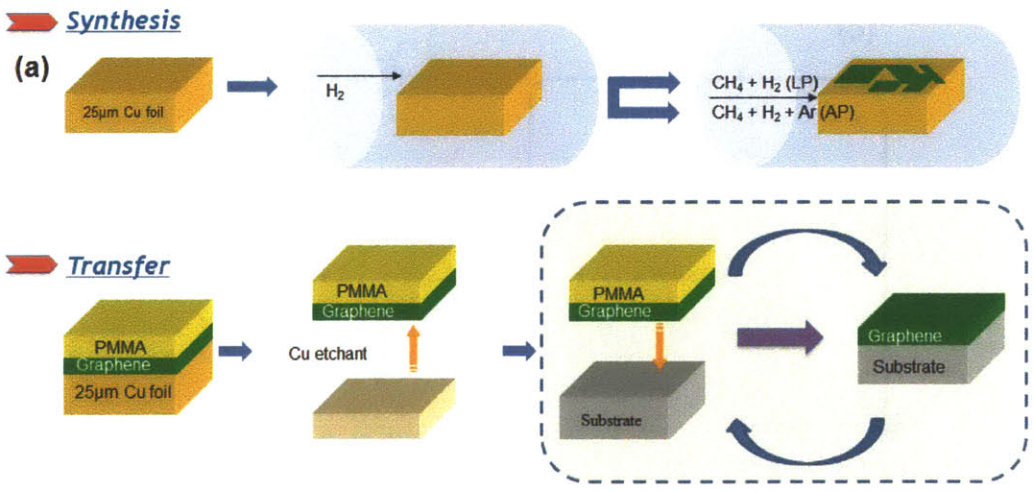

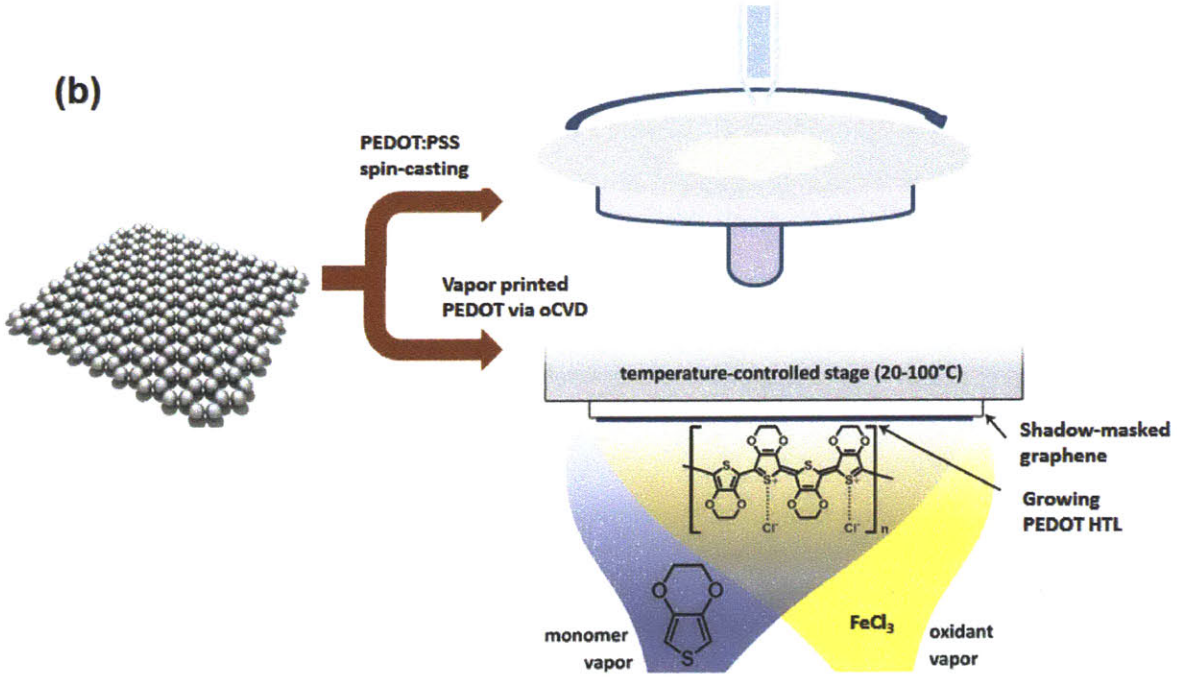
(b)
PEDOT:PSS
spin-casting
Vapor printed
PEDOT via oCVD
temperature-controlled stage (20-100°C)
Shadow-masked
graphene
Growing
PEDOT HTL
monomer
vapor
FeCl3
oxidant
vapor

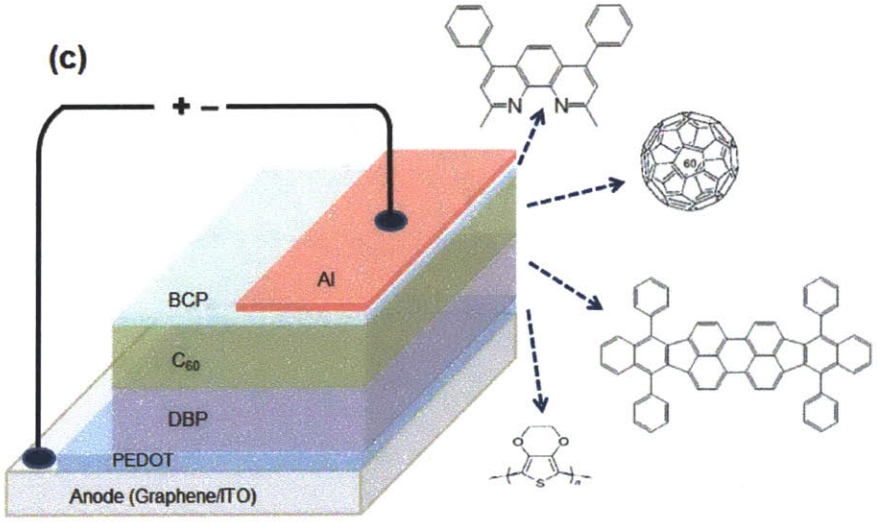
(c)
Al
BCP
C60
DBP
PEDOT
Anode (Graphene/ITO)

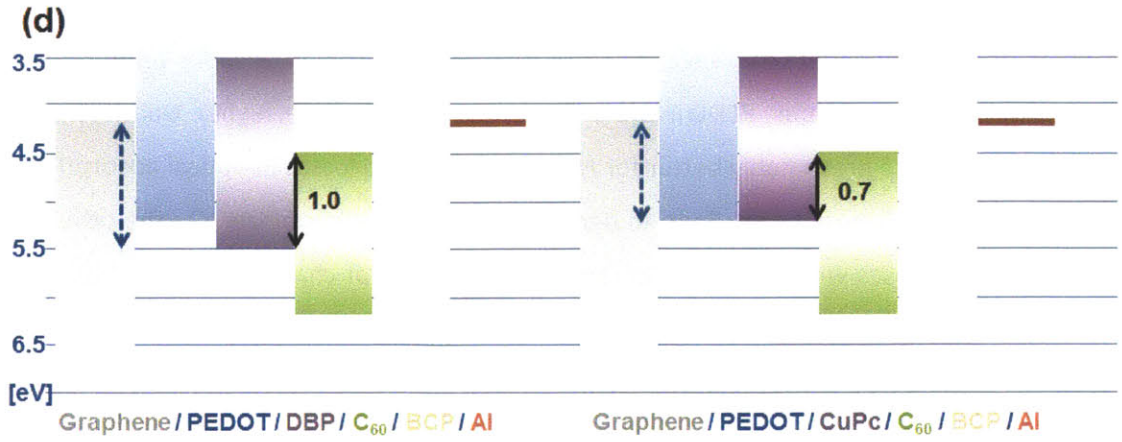

Figure 3-1: Schematics outlining the fabrication process of graphene electrodes, PEDOT HTLs, and OPV devices. (a) Graphene synthesis and transfer. The last part of the transfer procedure is repeated to prepare 3-layer graphene stacks for LPCVD graphene. Detailed growth parameters are graphically illustrated in the Supporting Figure 3-2. (b) PEDOT:PSS spin-coating vs. vapor printing of PEDOT deposition. The spin-casting layer covers the graphene and the surrounding quartz substrate while the vapor printed patterns align to produce PEDOT only on the graphene electrodes. (c) Graphene/ITO anode OPV structure: Graphene(or ITO)/PEDOT/DBP/C_{60}/BCP/Al. (d) Flat-band energy level diagram of the complete OPV device structure comparing DBP and CuPc electron donors.

After patterning the graphene electrodes, PEDOT (PEDOT:PSS or vapor printed PEDOT) and organic layers were subsequently deposited followed by the top capping electrode via thermal evaporation. The PEDOT deposition process is illustrated in Figure 3-1b. The final device structure was: anode (ITO or graphene)/HTL (PEDOT:PSS or vapor printed PEDOT)/DBP/C_{60} (fullerene)/BCP (bathocuproine)/Al (aluminum). The complete solar cell structure is schematically shown in Figure 3-1c.

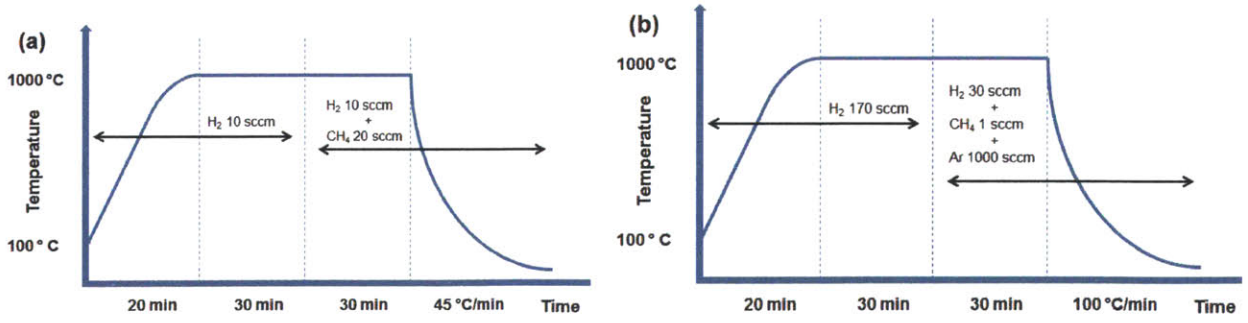

Figure 3-2: Illustration of graphene growth process at different stages: (a) LPCVD and (b) APCVD.

3.4 Results and Discussion

Shown in Figure 3-3a are sheet resistance (R_{sh}) and transmittance values of vapor printed PEDOT with varying thicknesses. The thinner PEDOT layers (2, 7, and 15 nm) have higher transmittance values (generally >90%) that are presumably better for HTL layers, because losses in optical absorption through the transparent electrode could contribute to decrease in device performance. On the other hand, the sheet resistance decreases with increasing thickness, with an abrupt change from 2 nm to the thicker layers (7, 15, and 40 nm) due to the amount of charge pathways increases (as shown in Figure 3-3b and Table 3-1).

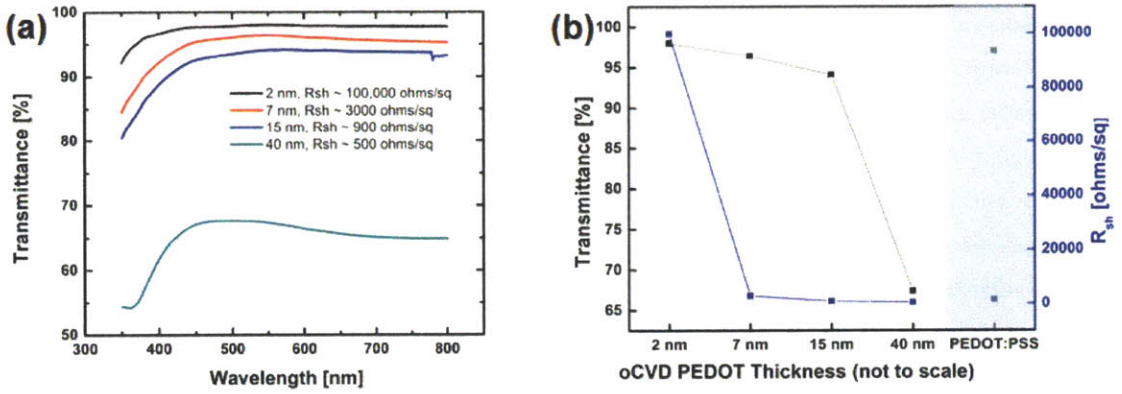

Figure 3-3: (a) Transmittance data for the oCVD PEDOT HTL layers, measured using ultraviolet-visible spectroscopy (UV-Vis) over wavelengths from 350-800 nm. The oCVD PEDOT layers decrease in transmittance and sheet resistance with increasing thickness. The three thinnest PEDOT layers (2, 7, and 15 nm) have high transmittance values (>90% over a majority of the range), which are preferred for HTL layers. (b) Sheet resistance values for each thickness and the transmittance at 550nm. The oCVD PEDOT sheet resistance was measured using a 4-point probe (taking the average of 10 measurements). With increasing oCVD PEDOT thickness, there are more pathways for charge transfer, so the sheet resistance (*Rsh*) decreases. *Rsh* decreases dramatically from the thinnest (2 nm) to thicker PEDOT layers (7, 15, and 40 nm). Transmittance and *Rsh* values of PEDOT:PSS are also shown for comparison.

Having a lower sheet resistance HTL results in better charge transfer to the graphene electrode, however, the thicker the HTL, the further the charge must travel through the layer to reach the graphene electrode and the greater the transmission losses due to absorption. Nevertheless, in our experiments, we have found that the thicknesses in the range of 7-40 nm all give reasonable performances.

Table 3-1: Optical transmittance (*%T*) and sheet resistance (R_{sh}) of oCVD PEDOT with varying thicknesses described in Figure 3-3. PEDOT:PSS values are also shown for comparison.

PEDOT Thickness	Transmittance at 550 nm (%T)	R_{sh} (Ω/sq)
oCVD PEDOT (2 nm)	98.0	100,000
oCVD PEDOT (7 nm)	96.4	3,000
oCVD PEDOT (15 nm)	94.1	900
oCVD PEDOT (40 nm)	67.4	500
PEDOT:PSS (40nm)	97.1	2,000

Figure 3-4 shows the optical and SEM images of the graphene/quartz substrate after spin-coating PEDOT:PSS (left images, Figure 3-4a-c) in contrast with the vapor printed PEDOT (15 nm) (right images, Figure 3-4d-f). The optical image in Figure 3-4a shows that most of the spin-casted PEDOT:PSS dewetts over the graphene electrode as well as the adjacent bare quartz (Figure 3-4b-c shows more details). The dewetting of the PEDOT:PSS is clearly observed over the entire substrate, which signifies that we do not have good coverage of the graphene surface. In contrast, vapor printing provides a well-defined PEDOT region (light blue) (Figure 3-4d). Furthermore, the scanning electron microscopy (SEM) image in higher magnification shows that the coating of vapor printed PEDOT on graphene is uniform in finer detail (Figure 3-4f).

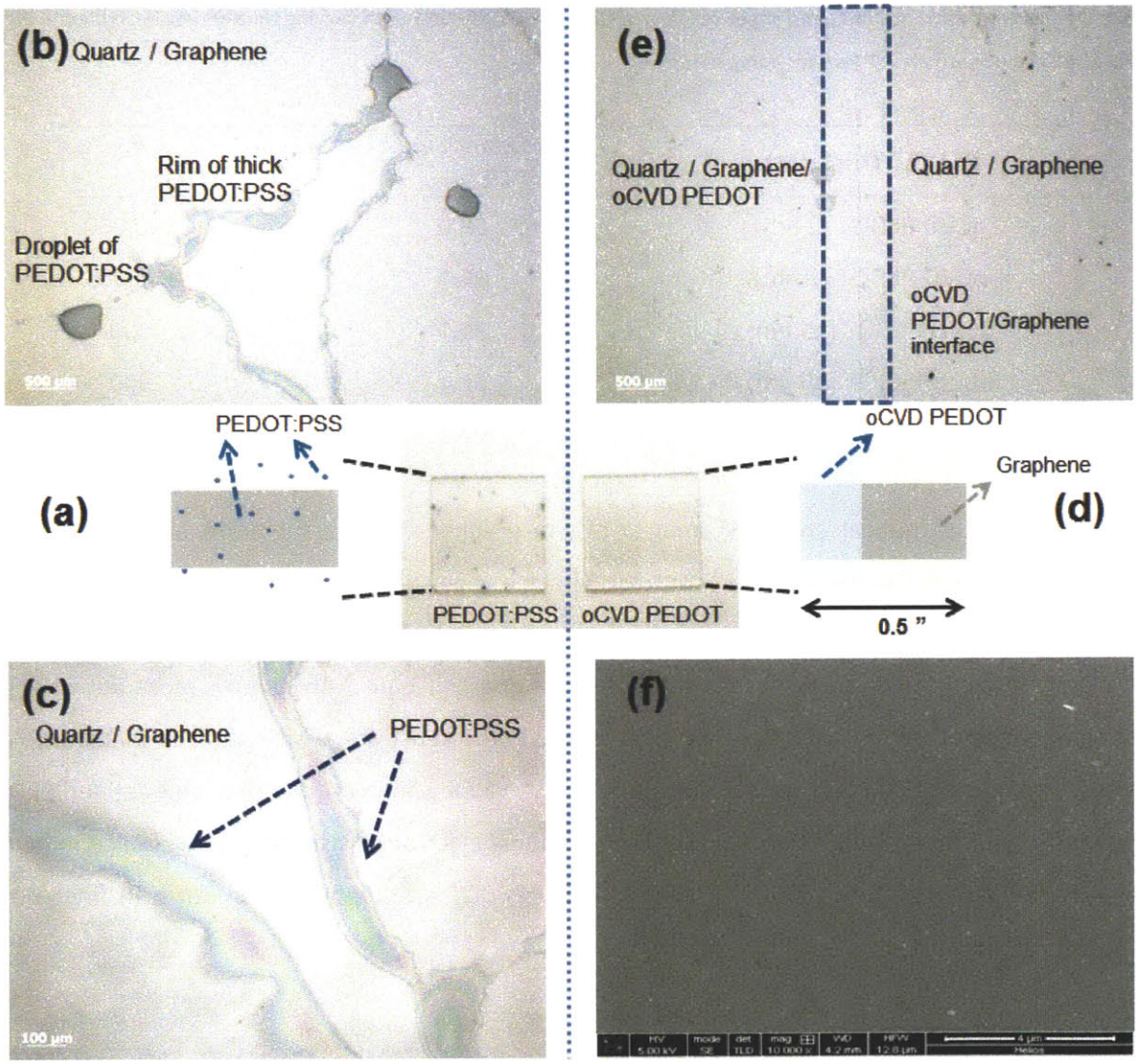

Figure 3-4:Comparing HTL coverage on quartz/graphene substrate. (a-c) Spin-coated PEDOT:PSS on quartz/graphene substrate, (d-f) oCVD PEDOT coating on quartz/graphene substrate: (a) schematic illustration of PEDOT:PSS spun-coated on a quartz substrate with graphene electrode. Most of the PEDOT:PSS layer is dewetted from the substrate with dark macroscopic defects visible to the naked eye. (b-c) Optical micrographs (at different magnifications) of the spin-cast PEDOT:PSS on the graphene surface illustrating the poor wettability of PEDOT:PSS on the graphene. In contrast, (d) is the schematic illustration of CVD PEDOT coated via vapor deposition on quartz/graphene substrate, where a uniform coating and patterning via shadow masking is achieved. The left side in (d) has the oCVD PEDOT coating whereas the right side is shadow masked. (e) Optical micrograph and (f) SEM image of oCVD PEDOT on graphene showing uniform coverage.

Additional atomic force microscopy (AFM) images of oCVD PEDOT are shown in Figure 3-5. oCVD PEDOT itself is relatively smooth and conformal coverage on the graphene surface is confirmed by the reduced surface roughness of the pristine graphene. This confirms the understanding that since oCVD is a dry process, the dewetting problem is avoided and the PEDOT can form a uniform film on the graphene.

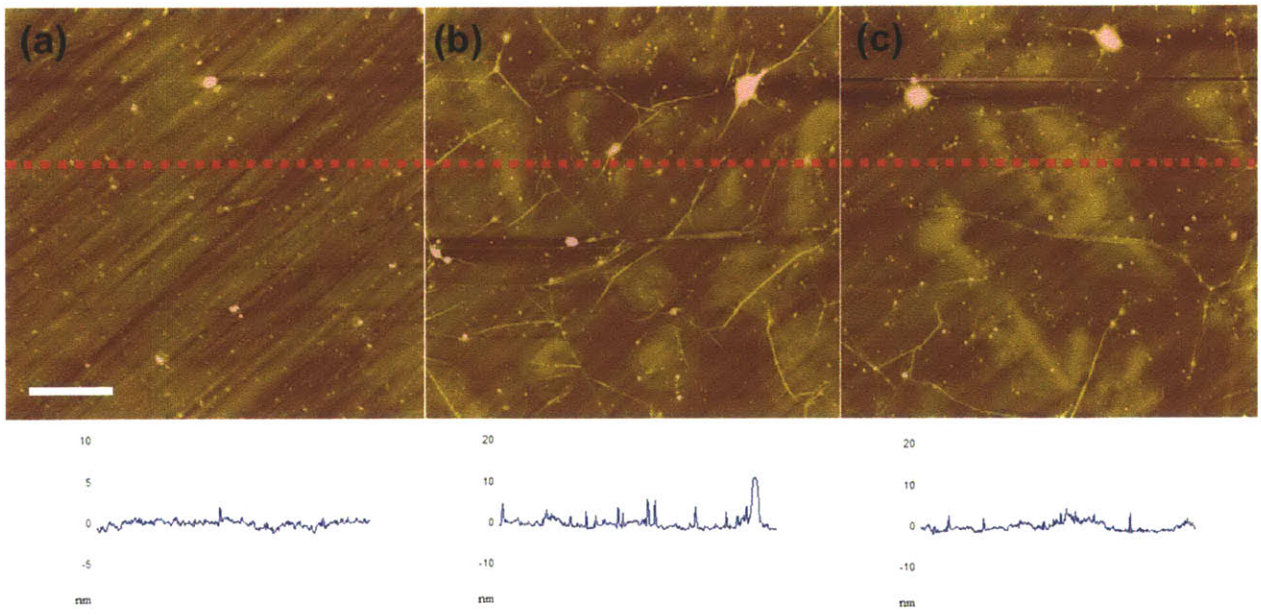

Figure 3-5: AFM (scale bar: 1μm) images of (a) oCVD PEDOT (15 nm), (b) graphene, and (c) oCVD PEDOT/graphene on quartz substrates, with corresponding cross-sectional profiles of the dotted sections. The surface morphology of oCVD PEDOT is relatively smooth (rms roughness 0.71 nm), and it is shown to conformally coat the graphene surface: rms roughness of the graphene is reduced after the oCVD PEDOT deposition from 2.45 nm to 2.20 nm.

Furthermore, the WF of vapor printed PEDOT on the graphene (3-layers) was evaluated by the Kelvin probe method. The measured value averaged over several regions was ~5.1 eV which was similar to the commonly reported WF value of PEDOT:PSS (~5.2 eV). This observation indicates that the injection/extraction of holes from the HOMO of electron donor now becomes energetically favorable compared to the interface of graphene only.

Small molecule organic solar cells with graphene anodes were fabricated with device structures mentioned earlier. Figure 3-6a displays the current density-voltage (*J-V*) measurements of devices with various configurations using 3-layer graphene anodes: graphene with spin-coated PEDOT:PSS and vapor printed PEDOT (15 nm) HTLs along with ITO reference. Due to the poor wetting of PEDOT:PSS, graphene device with PEDOT:PSS typically shows the leaky behavior (not a diode behavior but rather like a linear resistor), and with poor photo-response (much smaller V_{oc} and J_{sc}). On the other hand, the *J-V* responses from the devices having vapor printed PEDOT HTLs (with different thicknesses shown in Figure 3-6b-c for graphene and ITO electrodes) shows good diode behavior, and performance (J_{SC} (short-circuit current density) = 5.69 ± 0.17 mA cm^{-2}, V_{OC} (open-circuit voltage) = 0.88 ± 0.01 V, FF (fill factor) = 0.60 ± 0.01, and η_p (power conversion efficiency, PCE) = 3.01 ± 0.05%) is comparable to the ITO reference device with PEDOT:PSS (J_{SC}=5.14 ± 0.12 mA cm^{-2}, V_{OC} = 0.92 ± 0.01 V, FF = 0.68 ± 0.01, and η_p = 3.20 ± 0.05%).

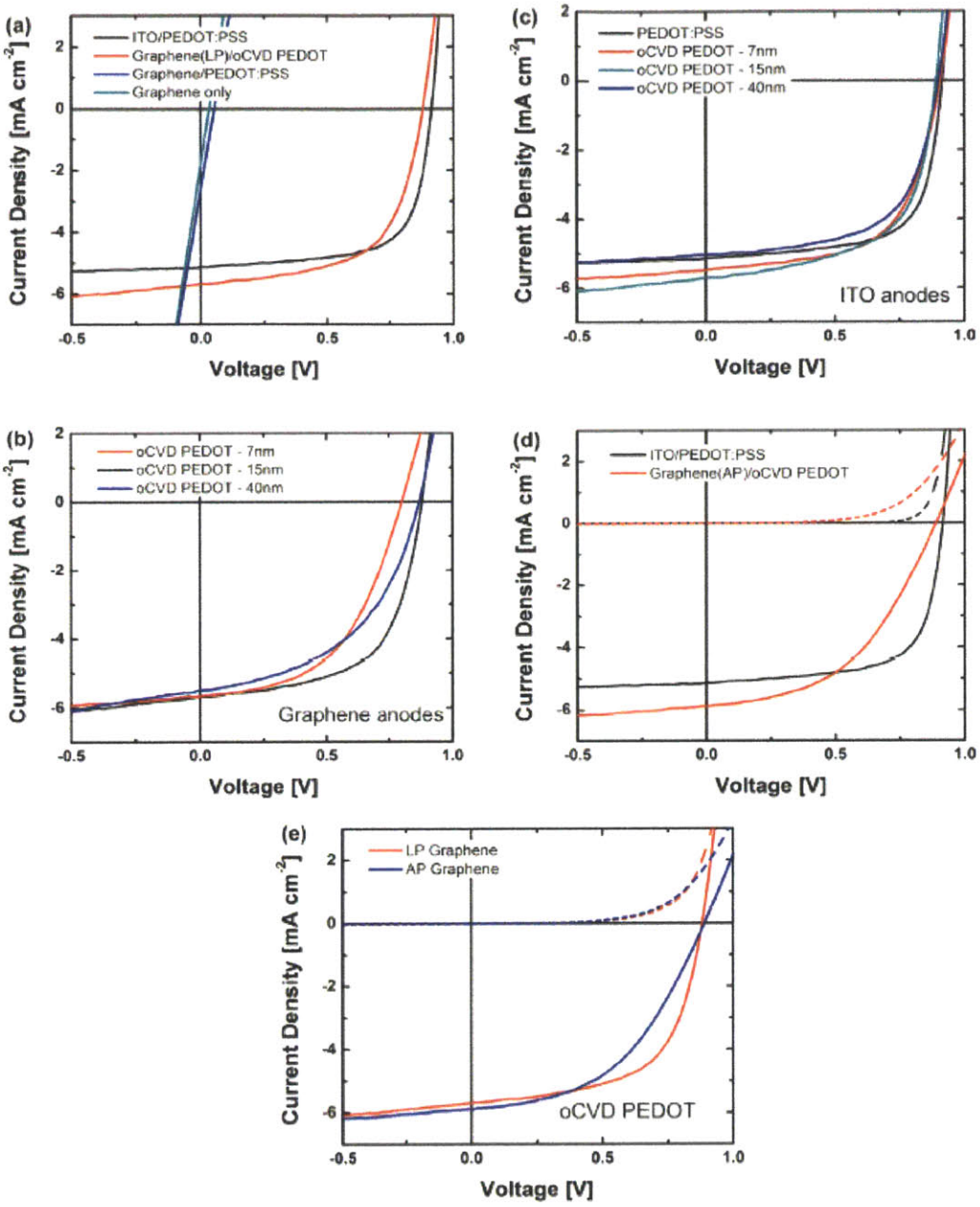

Figure 3-6: J-V characteristics of representative graphene (three-layer, LPCVD)/ITO OPV devices (graphene, ITO/PEDOT:PSS (20 nm), vapor printed PEDOT (7_40 nm)/DBP, 25 nm/C60, 40 nm/BCP, 7.5 nm/Al, 100 nm) under simulated AM 1.5G illumination at 100 mW/cm2. (a) Graphene devices with PEDOT:PSS and vapor printed PEDOT (15 nm) HTL, compared with ITO/PEDOT:PSS reference device. (b) Graphene-anode-based cells with varying thicknesses of vapor printed PEDOT (7, 15, 40 nm). (c) ITO anode devices with varying vapor printed PEDOT thicknesses (7, 15, 40 nm) and a PEDOT:PSS reference. (d) J-V characteristics of representative graphene (APCVD) OPV devices (graphene/vapor printed PEDOT, 15 nm/DBP, 25 nm/C60, 40 nm/BCP, 7.5 nm/Al, 100 nm) along with ITO/PEDOT:PSS reference device under simulatedAM1.5G illumination at 100mW/cm2. (e) Comparison of graphene-based device performances, where graphene electrodes are prepared under either LPCVD or APCVD conditions.

With more devices fabricated using the vapor printed PEDOT on graphene electrodes, we have found that about 30% among the working devices show the (close to) ideal diode *J-V* responses similar to the one presented in Figure 3-6, and with the other working devices non-ideal behaviors have been observed (both for graphene and ITO electrodes), as shown in Figure 3-7a-b. Nevertheless, these non-ideal performances are still considerably better than the performance obtained with devices having spin-coated PEDOT:PSS on graphene since for the PEDOT:PSS HTL, the graphene based devices almost never worked as shown in Figure 3-6. This ideal vs. non-ideal behavior does not appear to be related to the thickness of the vapor printed PEDOT on graphene, as can be seen in both Figure 3-6 and Figure 3-7, for thicknesses between 7-40 nm, the devices have displayed both behaviors. And even within the devices that showed ideal behaviors, there appear to be no direct correlation between the PCE value and the PEDOT thickness. At present the non-ideal behavior appear to be a process-related issue and should be further investigated in the follow up work.

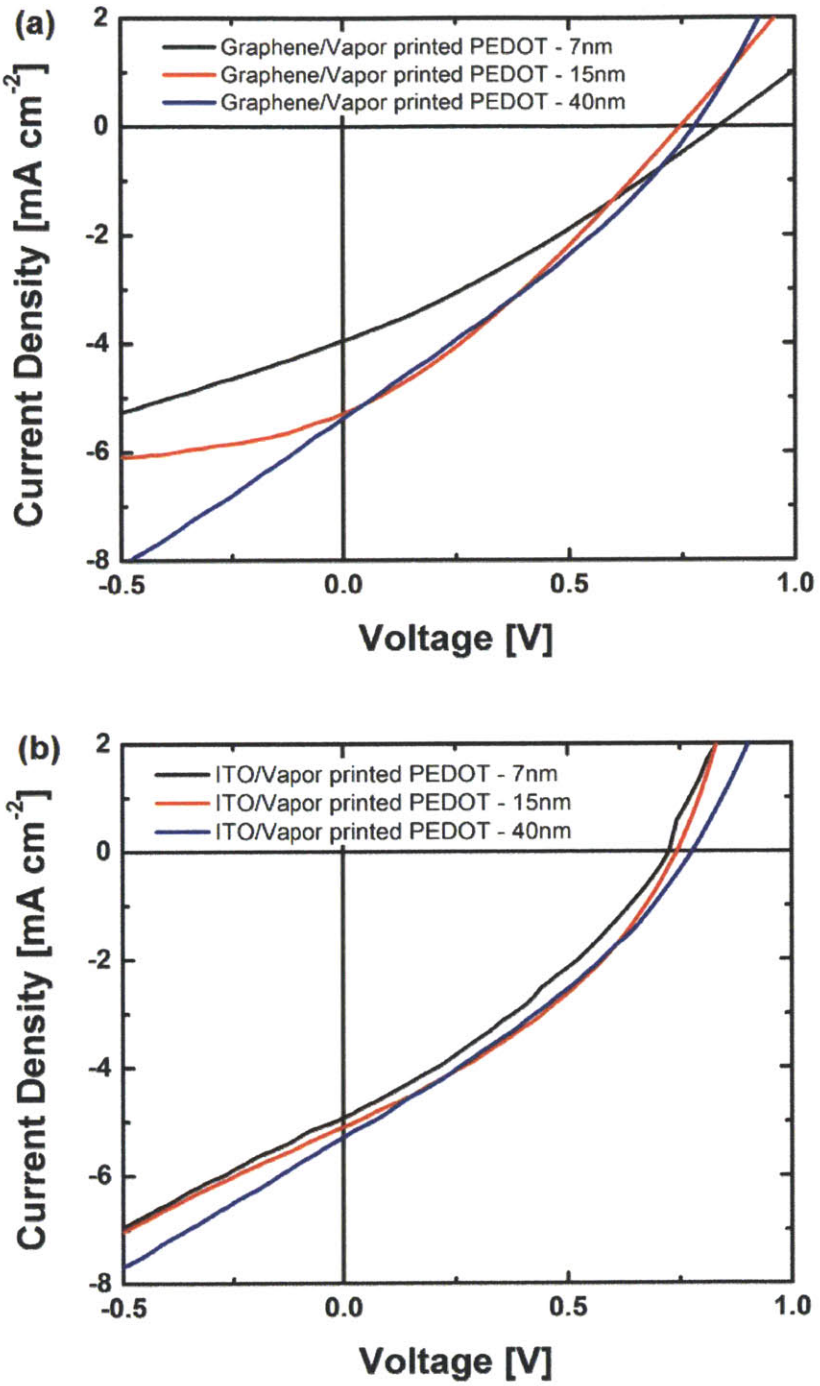

Figure 3-7: *J-V* characteristics of representative graphene (3-layer, LPCVD)/ITO solar cell devices with non-ideal diode characteristics under simulated AM 1.5G illumination at 100 mW/cm^2: Graphene, ITO/vapor printed PEDOT (7-40nm)/DBP, 25nm/C_{60}, 40nm/BCP, 7.5nm/Al, 100nm). (a) Graphene anode solar cells. (b) ITO anode solar cells. Corresponding key photovoltaic parameters of each device are summarized in Table 3-2.

Here it is worth pointing out that the value of η_p = 3.01% is the highest value reported for a graphene anode and small molecule based OPV (~94% of PCE of ITO based device). Apart from the successful

interface engineering by the vapor printed oCVD PEDOT on graphene, another reason for the enhanced performance can be attributed to the increased V_{OC} observed in the cells compared to devices fabricated using CuPc as electron donor materials, one of the most widely used electron donor materials in the small molecules based OPV structure. As shown from the energy level diagram in Figure 3-1d, the maximum V_{OC} achievable from DBP/C_{60} pair is ~1.0 V, ~0.3 V higher than CuPc/C_{60}. Therefore, improvements in V_{OC} mostly originate from the deep-lying HOMO level of DBP compared to that of CuPc.

Table 3-2: Summary of photovoltaic parameters of graphene/ITO devices from Figure 3-7.

Anode	HTL	J_{SC} (mA/cm^2)	V_{OC} (V)	FF	PCE (%)
ITO	oCVD PEDOT – 7nm	4.93	0.73	0.32	1.16
ITO	oCVD PEDOT – 15nm	5.10	0.74	0.35	1.34
ITO	oCVD PEDOT – 40nm	5.28	0.78	0.31	1.29
Graphene	oCVD PEDOT – 7nm	3.95	0.83	0.29	0.97
Graphene	oCVD PEDOT – 15nm	5.30	0.75	0.30	1.20
Graphene	oCVD PEDOT – 40nm	5.38	0.78	0.29	1.22

Graphene synthesized from the Cu catalyst under LP condition succeeded in producing high quality mono-layer sheets, which could not be achieved using nickel (Ni) catalyst.[23, 24] However, due to the self-limiting process of the LPCVD, achieving multi-layers of graphene from the Cu under LPCVD has been difficult.[23] In practice, a mono-layer of graphene sheet can be hardly used as an electrode due to defects induced from the processing issues such as transfer or patterning, as well as the generally lower conductivity compared to stacked multi-layers (R_{sh} decreases as a function of additional layers[17]). On the other hand, transferring multiple steps to obtain multi-layers add complexity and cost to the fabrication process. Therefore, in this work, we also carried out few-layer graphene synthesis under atmospheric CVD (APCVD) condition using Cu foils, where only one-step transfer is needed for graphene electrodes. Figure 3-8a,c shows the optical and AFM images of the APCVD grown graphene, which has a non-uniform film thickness, and the optical and AFM images of LPCVD graphene are also presented in Figure 3-8b,d for comparison. The APCVD graphene layers have average sheet resistance and transmittance values of ~450 Ω/sq and ~92% (at 550 nm), respectively. Even though the thicknesses of the APCVD grown graphene layers are non-uniform, we have verified that the vapor printing of oCVD PEDOT onto these graphene layers is as successful as the LPCVD graphene layers. This is consistent with

the general observation that oCVD PEDOT deposition is substrate independent and it coats uniformly on the substrate.

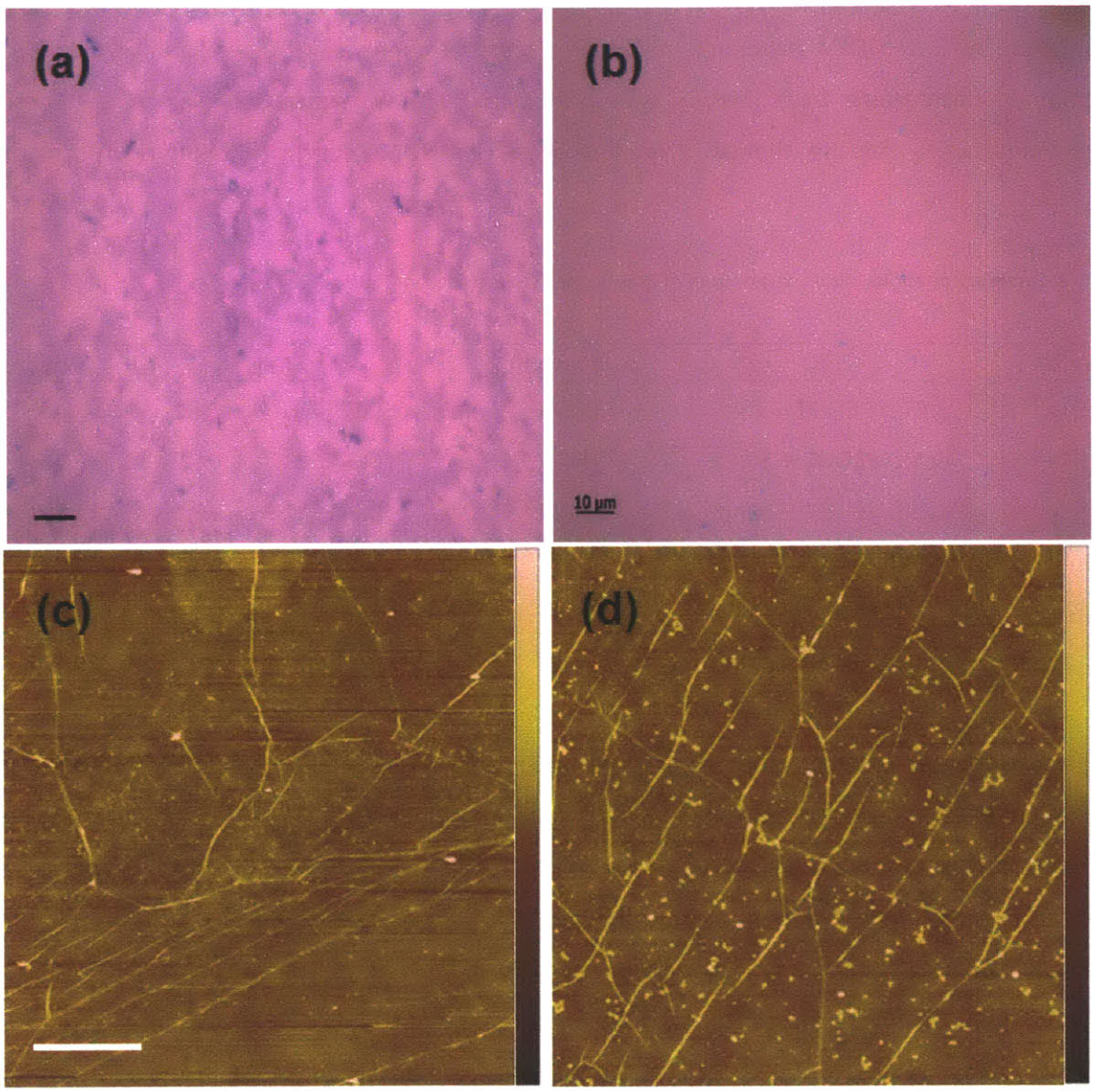

Figure 3-8: Optical (a-b, scale bar: 10 µm) and AFM (c-d, scale bar: 1µm, height bar: 20nm) images of graphene transferred on the SiO_2 (300 nm) substrates synthesized under different pressure conditions: (a, c) APCVD. (b, d) LPCVD images are shown for comparison. (a) APCVD graphene consists of non-uniformly distributed multilayer regions on top of the mono-layer background. (c) AFM image further illustrates the non-uniformity of APCVD graphene. The rms roughness of APCVD graphene is 1.66 nm compared to 1.17 nm for LPCVD graphene in (d).

Solar cells fabricated with graphene anodes prepared under APCVD conditions gives performance close to the devices made via LPCVD conditions ($\eta_{p,\ APCVD}$ = 2.49% and $\eta_{p,\ LPCVD}$ = 3.01%). Figure 3-9a shows the *J-V* characteristics of graphene device with vapor printed PEDOT (J_{SC} = 5.89 ± 0.03 mA cm^{-2}, V_{OC} = 0.89 ±

0.03 V, FF = 0.48 ± 0.01, and η_p = 2.49 ± 0.06%) and ITO reference device with PEDOT:PSS (J_{SC} =5.14 ± 0.12 mA cm^{-2}, V_{OC} = 0.92 ± 0.01 V, FF = 0.68 ± 0.01, and η_p = 3.20 ± 0.05%). Figure 3-9b compares the best device performance using graphene electrodes from different synthesis conditions (LPCVD vs. APCVD), illustrating comparable performances (APCVD graphene performs ~83% of LPCVD graphene).

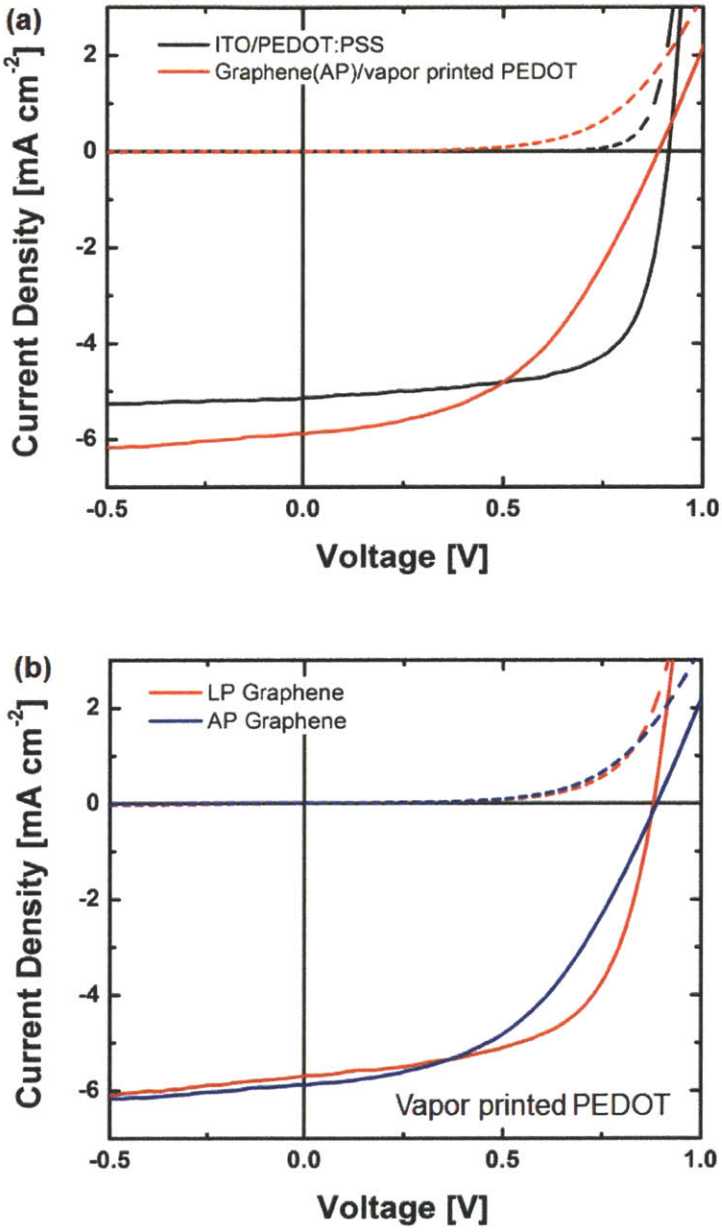

Figure 3-9: (a) *J-V* characteristics of representative graphene (APCVD) OPV devices (Graphene/vapor printed PEDOT, 15nm/DBP, 25nm/C_{60}, 40nm/BCP, 7.5nm/Al, 100nm) along with ITO/PEDOT:PSS reference device under simulated AM 1.5G illumination at 100 mW/cm^2. (b) Comparison of graphene-based device performances, where graphene electrodes are prepared under either LPCVD or APCVD conditions.

3.5 Conclusion

In summary, we introduce a novel, yet simple, method for vapor printing PEDOT onto the graphene surface, which yields well defined patterns using in situ shadow masking. The oCVD process, which is the foundation for vapor printing, results in smooth, complete coverage of PEDOT on the graphene electrode. In contrast, spin-casting PEDOT:PSS from an aqueous solution does not coat the graphene surface as well due to graphene's low surface free energy.[25] The oCVD process works well on both LPCVD grown graphene (with uniform thicknesses) and APCVD grown graphene (with non-uniform thicknesses). Furthermore, the use of small molecular electron donor material DBP combined with the vapor printed PEDOT HTL, yields more efficient graphene based devices with performances comparable to those of ITO reference devices. The results here represent a further step forward in the investigation of using graphene as an alternative TCE for the replacement of ITO and open up opportunities in other applications as well, such as organic light-emitting diodes (OLEDs).

3.6 Acknowledgments

This work was supported by Eni S.p.A. under the Eni-MIT Alliance Solar Frontiers Center and by a National Science Foundation Graduate Research Fellowship. This research was also supported in part by the Department of Energy Office of Science Graduate Fellowship Program (DOE SCGF), made possible in part by the American Recovery and Reinvestment Act of 2009, administered by ORISE-ORAU under contract no. DE-AC05-06OR23100.

3.7 References

1. H. Park, R. M. Howden, M. C. Barr, V. Bulović, K. Gleason and J. Kong, *ACS Nano*, 2012, **DOI: 10.1021/nn301901v**.
2. K. S. Novoselov, D. Jiang, F. Schedin, T. J. Booth, V. V. Khotkevich, S. V. Morozov and A. K. Geim, *Proceedings of the National Academy of Sciences of the United States of America*, 2005, **102**, 10451-10453.
3. C. Berger, Z. M. Song, X. B. Li, X. S. Wu, N. Brown, C. Naud, D. Mayou, T. B. Li, J. Hass, A. N. Marchenkov, E. H. Conrad, P. N. First and W. A. de Heer, *Science*, 2006, **312**, 1191-1196.
4. K. I. Bolotin, K. J. Sikes, Z. Jiang, M. Klima, G. Fudenberg, J. Hone, P. Kim and H. L. Stormer, *Solid State Commun.*, 2008, **146**, 351-355.
5. J. Moser, A. Barreiro and A. Bachtold, *Appl. Phys. Lett.*, 2007, **91**, 163513.
6. J. S. Bunch, A. M. van der Zande, S. S. Verbridge, I. W. Frank, D. M. Tanenbaum, J. M. Parpia, H. G. Craighead and P. L. McEuen, *Science*, 2007, **315**, 490-493.
7. G. Eda, G. Fanchini and M. Chhowalla, *Nature Nanotechnology*, 2008, **3**, 270-274.
8. K. K. Kim, A. Reina, Y. M. Shi, H. Park, L. J. Li, Y. H. Lee and J. Kong, *Nanotechnology*, 2010, **21**.
9. S. Bae, H. Kim, Y. Lee, X. F. Xu, J. S. Park, Y. Zheng, J. Balakrishnan, T. Lei, H. R. Kim, Y. I. Song, Y. J. Kim, K. S. Kim, B. Ozyilmaz, J. H. Ahn, B. H. Hong and S. Iijima, *Nature Nanotechnology*, 2010, **5**, 574-578.

10. Y. Park, V. Choong, Y. Gao, B. R. Hsieh and C. W. Tang, *Appl. Phys. Lett.*, 1996, **68**, 2699-2701.
11. D. J. Milliron, I. G. Hill, C. Shen, A. Kahn and J. Schwartz, *J. Appl. Phys.*, 2000, **87**, 572-576.
12. D. Fujishima, H. Kanno, T. Kinoshita, E. Maruyama, M. Tanaka, M. Shirakawa and K. Shibata, *Sol. Energy Mater. Sol. Cells*, 2009, **93**, 1029-1032.
13. Y. Wang, X. H. Chen, Y. L. Zhong, F. R. Zhu and K. P. Loh, *Appl. Phys. Lett.*, 2009, **95**, 063302.
14. S. Gunes, H. Neugebauer and N. S. Sariciftci, *Chemical Reviews*, 2007, **107**, 1324-1338.
15. P. Peumans and S. R. Forrest, *Appl. Phys. Lett.*, 2001, **79**, 126-128.
16. T. N. Murakami, Y. Fukushima, Y. Hirano, Y. Tokuoka, M. Takahashi and N. Kawashima, *Colloids and Surfaces B-Biointerfaces*, 2003, **29**, 171-179.
17. H. Park, J. A. Rowehl, K. K. Kim, V. Bulovic and J. Kong, *Nanotechnology*, 2010, **21**, 6.
18. Y. W. Y. Wang, S. W. Tong, X. F. Xu, B. Ozyilmaz and K. P. Loh, *Advanced Materials*, 2011, **23**, 1514-1518.
19. L. Cattin, F. Dahou, Y. Lare, M. Morsli, R. Tricot, S. Houari, A. Mokrani, K. Jondo, A. Khelil, K. Napo and J. C. Bernede, *J. Appl. Phys.*, 2009, **105**, 034507.
20. M. C. Barr, J. A. Rowehl, R. R. Lunt, J. Xu, A. Wang, C. M. Boyce, S. G. Im, V. Bulović and K. K. Gleason, *Advanced Materials*, 2011, **23**, 3500-3505.
21. S. G. Im, K. K. Gleason and E. A. Olivetti, *Appl. Phys. Lett.*, 2007, **90**, 152112.
22. J. P. Lock, S. G. Im and K. K. Gleason, *Macromolecules*, 2006, **39**, 5326-5329.
23. X. S. Li, W. W. Cai, J. H. An, S. Kim, J. Nah, D. X. Yang, R. Piner, A. Velamakanni, I. Jung, E. Tutuc, S. K. Banerjee, L. Colombo and R. S. Ruoff, *Science*, 2009, **324**, 1312-1314.
24. A. Reina, X. T. Jia, J. Ho, D. Nezich, H. B. Son, V. Bulovic, M. S. Dresselhaus and J. Kong, *Nano Letters*, 2009, **9**, 30-35.
25. S. R. Wang, Y. Zhang, N. Abidi and L. Cabrales, *Langmuir*, 2009, **25**, 11078-11081.

CHAPTER FOUR

Top-illuminated organic photovoltaics on a variety of opaque substrates with vapor-printed PEDOT top electrodes

The work described in this chapter has been published in *Advanced Energy Materials*[1]

4.1 Abstract

Organic photovoltaics devices typically utilize illumination through a transparent substrate, such as glass or an optically clear plastic. Utilization of opaque substrates, including low cost foils, papers, and textiles, requires architectures that instead allow illumination through the top of the device. Here, we demonstrate top-illuminated organic photovoltaics, employing a dry vapor-printed poly(3,4-ethylenedioxythiophene) (PEDOT) polymer anode deposited by oxidative chemical vapor deposition (oCVD) on top of a small-molecule organic heterojunction based on vacuum-evaporated tetraphenyldibenzoperiflanthene (DBP) and C_{60} heterojunctions. Application of a molybdenum trioxide (MoO_3) buffer layer prior to oCVD deposition increases the device photocurrent nearly 10 times by preventing oxidation of the underlying photoactive DBP electron donor layer during the oCVD PEDOT deposition, and resulting in power conversion efficiencies of up to 2.8% for the top-illuminated, ITO-free devices, approximately 75% that of the conventional cell architecture with indium-tin oxide (ITO) transparent anode (3.7%). Finally, we demonstrate the broad applicability of this architecture by fabricating devices on a variety of opaque surfaces, including common paper products with over 2.0% power conversion efficiency, the highest to date on such fiber-based substrates.

4.2 Introduction

Organic photovoltaics (OPVs) have gained significant momentum as a possible low-cost energy source, and have recently reached record efficiencies of nearly 10%,[2] suggesting near-term commercial potential. One particularly promising direction is deployment on the surface of everyday items, such as wall coverings, product packaging, documents, and apparel, enabled by mechanically flexible device layers, low-temperature manufacturing requirements, and low toxicity.[3-5] For example, there has been significant recent interest in integrating electronics on paper substrates.[6-11] However, for these applications, the OPV must be compatible with opaque substrates.

In the conventional orientation, the OPV is illuminated through a transparent hole-collecting anode deposited on the substrate, typically indium-tin oxide (ITO), and electrons are collected by a low work function metal cathode top contact. This structure necessitates that the substrate be transparent (e.g. glass or optically clear plastics). Alternative top-illuminated OPV architectures that are compatible with opaque substrates, and have useful application in semi-transparent and tandem device structures, require deposition and patterning of a transparent electrode on top of the complete organic device stack.[12] Such devices have previously been demonstrated with sputtered ITO top anodes with a MoO_3 anode buffer layer, reaching efficiencies of 2.4% with evaporated small molecule organic active layers,[13]

and 3% with a poly(3-hexylthiophene) (P3HT): [6,6]-phenyl C_{61} butyric acid methyl ester (PCBM) bulk heterojunction active layer.[14] Transparent ITO top cathodes have also been demonstrated on top of a bathocuproine (BCP) exciton blocking layer in opaque[15] and visible-light transparent[13] small molecule OPVs on glass substrates. However, in these configurations, the ITO transparent electrode must be sputtered on top of the full device which can damage underlying organic layers, and is prone to cracking on highly flexible substrates.[16-18] As an alternative to sputtered metal-oxide transparent top electrodes, ultrathin metal films deposited by vacuum thermal evaporation, have also been demonstrated as the top transparent cathode in top-illuminated, small molecule organic OPVs, reaching efficiencies of 2.2%.[17, 19-21]

Conducting polymer electrodes based on poly(3,4-ethylenedioxythiophene) (PEDOT) are an attractive alternative transparent electrode due to their potential low cost, ease of processing, and mechanical robustness on highly flexible substrates, such as plastic, textiles, and paper.[6, 7, 18] Solution deposited PEDOT, doped with poly(styrenesulfonate) (PEDOT:PSS), has been widely used as a hole-transporting anode buffer layer on ITO,[22, 23] and also demonstrated as a top anode in top-illuminated polymer OPVs based on P3HT:PCBM with efficiencies up to 2.4%.[7, 24-26] However, PEDOT:PSS top-electrode configurations generally require that the underlying device layers do not dissolve or intermix during the solvent deposition process, restricting applicability in many multilayered and tandem device architectures, and limiting demonstrations to single-junction P3HT:PCBM cells.[7, 16, 18, 24-27]

Oxidative chemical vapor deposition (oCVD), is a solvent-free, vacuum-based technique, in which conjugated polymer films are formed directly on the substrate by oxidative polymerization of vapor-phase monomer and oxidant precursors at low temperature (25-150 °C).[6, 28-30] Well-defined polymer patterns can be "vapor-printed" on the substrate of choice when this process is combined with *in situ* shadow masking. Thus, oCVD offers an attractive solvent-free route to transparent polymer top electrodes, while maintaining the benefits of vacuum processing, including parallel and sequential deposition, well-defined thickness control and uniformity, and inline compatibility with standard vacuum process (e.g. thermal evaporation).[29]

Here, we demonstrate top-illuminated OPVs with an oCVD PEDOT transparent anode on top of a small-molecule organic heterojunction based on vacuum-evaporated tetraphenyldibenzoperiflanthene (DBP) and fullerene C_{60} planar heterojunctions.[31] Application of a molybdenum trioxide (MoO_3) buffer layer prior to oCVD deposition increases the device photocurrent nearly 10 times by preventing oxidation of

the underlying photoactive DBP electron donor layer during the oCVD PEDOT deposition, and results in power conversion efficiencies of up to 2.8% for these top-illuminated, ITO-free devices, approximately 75% that of the conventional cell architecture with indium-tin oxide (ITO) transparent anode (3.7%). Finally, we demonstrate the broad applicability of this architecture by fabricating devices on a variety of opaque fiber-based surfaces, including common paper products with over 2.0% power conversion efficiency, the highest to date on such substrates.

4.3 Experimental

Substrate Preparation

Pre-cut glass substrates as well as pre-patterned ITO substrates (Thin Film Devices, 20 Ω/sq), for the conventional control devices, were cleaned by subsequent sonication in DI water with detergent, DI water, acetone, and isopropyl alcohol, followed by 30 seconds of O_2 plasma (100 W, Plasma Preen, Inc.). Common opaque substrates (Figure 4-5) were cut to size with scissors, but used without any pretreatment or cleaning procedures: photo paper (Office Depot, #394-925); magazine print (food network magazine, inner page); US First Class Stamp (2011 "forever" stamp); and plastic food wrapper (Kellogg's® pop-tarts™).

Device Fabrication

The Ag cathode, organic active layers (BCP, C_{60}, and DBP), and MoO_3, were thermally evaporated onto the substrate in sequence through shadow masks at a pressure of ~1×10^{-6} Torr at rates of ~1.0 Å/s. The C_{60} (Sigma Aldrich, 99.9%) and DBP (Luminescencev Technology Corp., >99.5%) were each purified once via thermal gradient sublimation before use; the BCP (Luminescence Technology Corp., >99%), MoO_3 (Sigma Aldrich, powder, 99.99%), and Ag (Alfa Aesar, 1-3 mm shot, 99.9999%) were all used as received. PEDOT top electrodes were then deposited directly on top of the partially completed inverted OPVs in a vacuum chamber using the oxidative chemical vapor deposition process (oCVD), which is described in detail elsewhere.[30, 32, 33] Here, the oCVD PEDOT top electrodes were all synthesized during the same deposition at a reactor pressure of ~1e-4 Torr and a substrate temperature of 150 °C, via simultaneous exposure to vapors of 3,4-ethylenedioxythiophene (EDOT) monomer (Aldrich 97%) metered at ~5 sccm and $FeCl_3$ oxidant (Sigma Aldrich, 99.99%) controllably evaporated from a resistively heated crucible at ~170 °C for ~20 min. No post-treatment or solvent rinsing steps were used, as has been described previously.[33] The PEDOT electrodes were patterned *in situ* during the oCVD process by positioning pre-

cut metal shadow masks in intimate contact with the substrate, which were aligned by hand with the pattern of the bottom device layers. The overlap area between the PEDOT top anode and the Ag bottom cathode defined the device area (~0.012 cm^2), which was measured after testing with an optical microscope. The resulting device structures were either Glass/ITO/MoO_3 (20 nm)/DBP (25 nm)/C_{60} (40 nm)/BCP (7.5 nm)/Ag (100 nm) (conventional control orientation) and Substrate/Ag (100 nm)/BCP (7.5 nm)/C_{60} (40 nm)/DBP (XX nm)/MoO3 (20 nm)/oCVD PEDOT (top-illuminated orientation).

Characterization

Current density-voltage (J-V) characteristics were measured for the completed OPV devices in nitrogen atmosphere using a Keithley 6487 picoammeter. Devices were tested using 110 ± 10 mW cm^{-2} illumination provided by a 1kW xenon arc-lamp (Newport 91191) with an AM 1.5G filter, and the solar simulator intensity was measured with a calibrated silicon photodiode. The external quantum efficiency (EQE) spectra were measured with a Stanford Research Systems SR830 lock-in amplifier, under a focused monochromatic beam of variable wavelength light generated by an Oriel 1kW xenon arc lamp coupled to an Acton 300i monochromator and chopped at 43 Hz. A Newport 818-UV calibrated silicon photodiode was used to measure the incident monochromatic light intensity. Optical transmittance measurements were made for on the DBP and C_{60} films before and after $FeCl_3$ exposure using a Varian Cary 6000i UV-Vis-NIR dual-beam spectrophotometer. PEDOT electrode thicknesses were measured on bare glass slides (positioned next to the OPV devices during oCVD deposition) with a Tencor P-16 profilometer and the sheet resistance was measured using a Signatone S-302-4 four-point probe station with a Keithley 4200-SCS semiconductor characterization system.

4.4 Results and Discussion

For the OPVs in this work, we used a simple single-junction bilayer structure based on thermally evaporated small-molecule organic active layers tetraphenyldibenzoperiflanthene (DBP) as the electron donor and fullerene C_{60} as the electron acceptor with a bathocuproine (BCP) exciton blocking layer at the cathode interface (Figure 4-1a). The conventional orientation device structure on glass/ITO has been discussed previously for these materials, reaching efficiencies of up to 3.6%.[31] Here, we also optionally insert thermally evaporated molybdenum trioxide (MoO_3) layer at the anode interface, which has previously been demonstrated as an electron-blocking layer and physical buffer layer in polymer and small-molecule organic photovoltaics.[34-40]

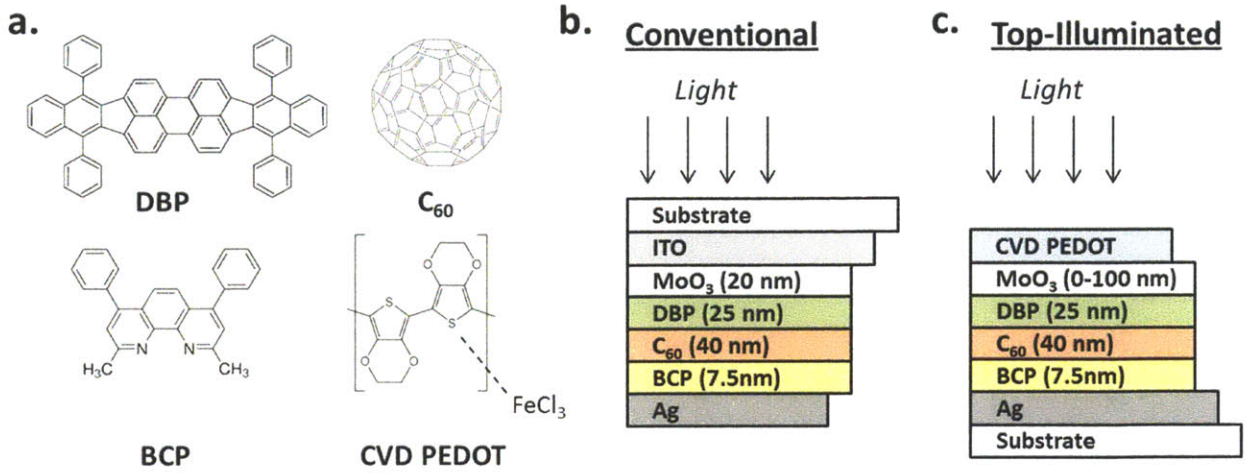

Figure 4-1: Schematics of the device structures and materials used in this report: (a) Chemical structures of DBP, C_{60}, BCP, and CVD PEDOT polymerized and doped with $FeCl_3$. (b) Conventional orientation PV device with transparent ITO anode (device is illuminated from the substrate side). (c) Top-illuminated orientation PV device with transparent CVD PEDOT anode (device is illuminated from the device side).

The conventional device structure was first optimized on ITO-coated glass substrates with the thicknesses shown in Figure 4-1b [MoO_3 (20 nm)/DBP (25 nm)/C_{60} (40 nm)/BCP (7.5 nm)/Ag], and used subsequently as a point of comparison. For the top-illuminated device, the same organic active layers and thicknesses were used, while the order of deposition was reversed, starting from the substrate: Ag, BCP, DBP, C_{60}, (MoO_3). For the transparent top electrode, instead of ITO, PEDOT layer was grown by oCVD from the 3,4-ethylenedioxythiophene monomer with $FeCl_3$ oxidant (Figure 4-1c). The thickness of the oCVD PEDOT electrodes used here were 60±10 nm, which was controlled by the time of deposition, and resulted in films with a sheet resistance of ~200±50 Ω/sq at the conditions used here (see Experimental Section). Although the DBP, C_{60}, and BCP layer thicknesses from optimized conventional device were also used in the top-illuminated device for consistency, we note that the optical environment is not identical since the conventional devices goes from a high index glass and ITO to the device stack, while the inverted structure has MoO3, PEDOT, and then air. This said, the reflective Ag node is maintained in the same position relative to the DBP/C_{60} heterojunction interface, which also strongly affects the positioning of the optical electric field maxima within the respective device layers. We also note that in the conventional orientation, defect states are created in the BCP layer when the metal cathode is deposited on top it, which are proposed to provide efficient electron transport through this layer.[41] In the reversed stack, the BCP organic layer is positioned on top of the bottom Ag surface, and thus likely absent of these states which may increase series resistance through the device.[42]

Figure 4-2a compares the current density-voltage (*J-V*) characteristics of the optimized conventional device on ITO with top-illuminated, oCVD PEDOT devices with and without MoO_3 on glass substrates, and a summary of the performance parameters are shown in

Table 4-1.

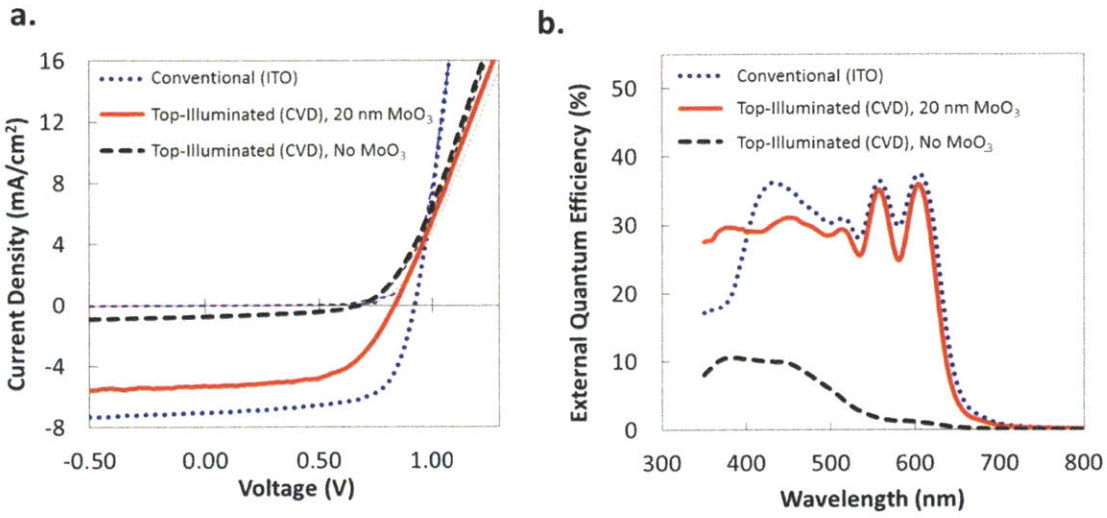

Figure 4-2: (a) Representative J-V performance curves measured under 1.1 sun illumination and (b) external quantum efficiency spectra, for the conventional device with ITO anode (dotted blue) and top-illuminated devices with CVD PEDOT anode, with (solid red) and without (dashed black) MoO_3 as a buffer layer. All devices are on silver-coated glass substrates.

The optimized, conventional, control device exhibits power conversion efficiency (η_p)=3.7±0.3%, open-circuit voltage (V_{OC})= 0.93±0.03V, short-circuit current (J_{SC})= 6.72±(0.3) mA cm^{-2}, and fill factor (*FF*)= 0.66±0.04, consistent with previous reports.[31] Inverting the device and replacing the ITO with the oCVD PEDOT top electrode, decreases the J_{SC} to 4.7±1.6 mA cm^{-2}, V_{OC} to 0.84±0.01 V, and *FF* to 0.58±0.01, resulting in η_p of 2.1±0.6%. The decrease in *Jsc* likely results from small absorptive losses in the less transparent oCVD PEDOT electrode, as observed previously with oCVD PEDOT bottom electrode devices.[6] The *FF* decreases due to increased series resistance, observable in the *J-V* curve under forward bias, which is a result of the more resistive oCVD PEDOT compared to ITO,[6] and possibly detieriorated by the lack of defect states in the BCP layer as discussed above. Removing the MoO_3 between the oCVD PEDOT top electrode and DBP electron donor, significantly decreases the J_{SC} to 0.76±1.6 mA cm^{-2}, the V_{OC} to 0.68±0.02 V, and *FF* to 0.44±0.02, resulting in a η_p of only 0.21±0.1%.

Table 4-1: Summary of performance parameters under 1.1 sun illumination for devices on glass substrates (Figure 2).

Device	J_{sc} (mA/cm^2)	V_{oc} (V)	FF	PCE (%)
Conventional	6.7 ± (0.3)	0.93 ± (0.03)	0.66 ± (0.04)	3.7 ± (0.3)
MoO3 (20 nm)	4.7 ± (1.6)	0.84 ± (0.01)	0.58 ± (0.01)	2.1 ± (0.6)
MoO3 (0 nm)	0.76 ± (0.05)	0.68 ± (0.02)	0.44 ± (0.02)	0.21 ± (0.01)

To understand the origin of the differences in device photocurrent, we measured the external quantum efficiency spectrum for each of these device structures (Figure 4-1b). As expected, the EQE of the top-illuminated CVD device with MoO_3 is slighty lower than that of the conventional device across the wavelength range, which is consistent with the lower observed J_{SC} due to absorptive losses from the oCVD PEDOT electrode as discussed previously.[6] The characterstic absorption peaks from DBP (570 nm and 610 nm) are strongly evident in the EQE of the conventional device and top-illuminated device with MoO_3; however, do not appear in the top-illuminated device without MoO_3, which only shows photocurrent generation below 550 nm, in the region where C_{60} absorbs, indicating a loss of photocurrent originating from the DBP.

In the devices without MoO_3, the surface of the DBP photoactive layer is exposed to $FeCl_3$ oxidant precursor during the oCVD process. To better understand this effect, absorption data was collected on blanket films of DBP and C_{60} both before and after exposure to $FeCl_3$, in the oCVD chamber, under the same pressure and temperature conditions experienced during PEDOT polymerization. Figure 4-3 shows the UV-visible absorbance data for the active layer films before and after $FeCl_3$ exposure both with and without a MoO_3 buffer layer. Though the C_{60} absorption remains unchanged (Figure 4-3b), the bare DBP absorption peaks decrease significantly upon exposure to $FeCl_3$ (Figure 4-3a). This is consistent with the EQE spectra for the top-illuminated device without MoO_3, which only shows photocurrent originating from C_{60} and suggests that the bare DBP layer is prone to oxidation by $FeCl_3$ while the more stable resonant structure of C_{60} remains unaffected. With the addition of the MoO_3 buffer layer (20 nm) on top of the DBP before exposing to $FeCl_3$, the absorption peaks of the DBP remain intact, indicating that the thin MoO_3 layer physically protects the underlying DBP layer from chemically interacting with the $FeCl_3$ during the oCVD process.

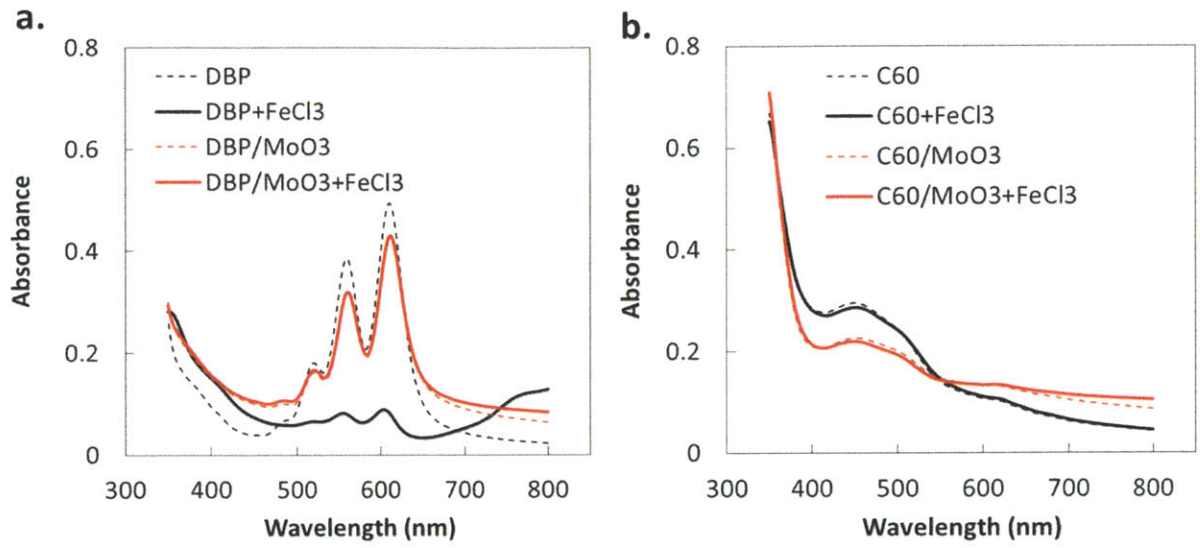

Figure 4-3: UV-visible absorbance spectra for (a) glass/DBP [25 nm]/MoO_3 [0 nm (black) and 20 nm (red)] and (b) glass/C_{60} [40 nm]/MoO_3 [0 nm (black) and 20 nm (red)] . Films were measured before (dashed) and after (solid) exposure to $FeCl_3$ under CVD polymerization conditions.

To further understand how this layer affects device performance, top-illuminated devices with oCVD PEDOT electrodes were fabricated using varying thicknesses (0, 2 nm, 20 nm, 50 nm, and 100 nm) of the MoO_3 buffer layer. Figure 4-4 shows how the main device characteristics (J_{SC}, V_{OC}, *FF*, and η_p) vary with MoO_3 layer thickness. The ultra-thin MoO_3 layer (2 nm) was found to be too thin to protect the underlying active layers during PEDOT polymerization and these devices showed similarly low *Jsc* and V_{OC} characteristics as the devices with no MoO_3. Increasing the MoO_3 thickness further from 20 to 100 nm resulted in a plateau in *Jsc* around 6.0 mA cm^{-2} between 20 and 50 nm (Figure 4-4a), demonstrating limited additional benefit in protecting the photocurrent generation of the underlying semiconductors. Similarly, the V_{OC} increases and eventually plateaus with increasing MoO_3 thickness (Figure 4-4b). The high V_{OC} observed with the MoO_3 layer present is supported by the high work function of MoO_3 (5.7±0.4 eV),[43] compared with the work function of bare CVD PEDOT (5.2±0.1 eV),[44] resulting in increased work function offset between the anode and cathode. It has been also been reported that the MoO_3 work function and band gap both increase with thickness, which can increase *Voc* by reducing electron leakage current from the donor layer and enhancing hole extraction by increased band banding at the MoO_3/donor interface.[13, 43] The maximum Voc observed here is very close to that of the conventional cell; however, we note that some variation may be due to the reversed order of deposition of the cathode interface (i.e., BCP on Ag instead of Ag on BCP) which could increase series resistance or the effective work cathode function. The FF gradually decreases with increasing MoO_3 thickness due to

increased series resistance through the device (Figure 4-4c). The maximum observed η_p of 2.8% was achieved for a device with a 100 nm MoO_3 layer (Figure 4-4d); however, the optimal MoO_3 thickness seems to be lower than 100 nm, where we see maximum values for V_{OC}, J_{SC}, and *FF*. For example, a device having the maximum V_{OC} (0.91 V), J_{SC} (6.7 mA cm^{-2}), and *FF* (0.61) observed with 50 nm MoO_3 (which were not all observed on the same individual device) would give an efficiency of 3.4%.

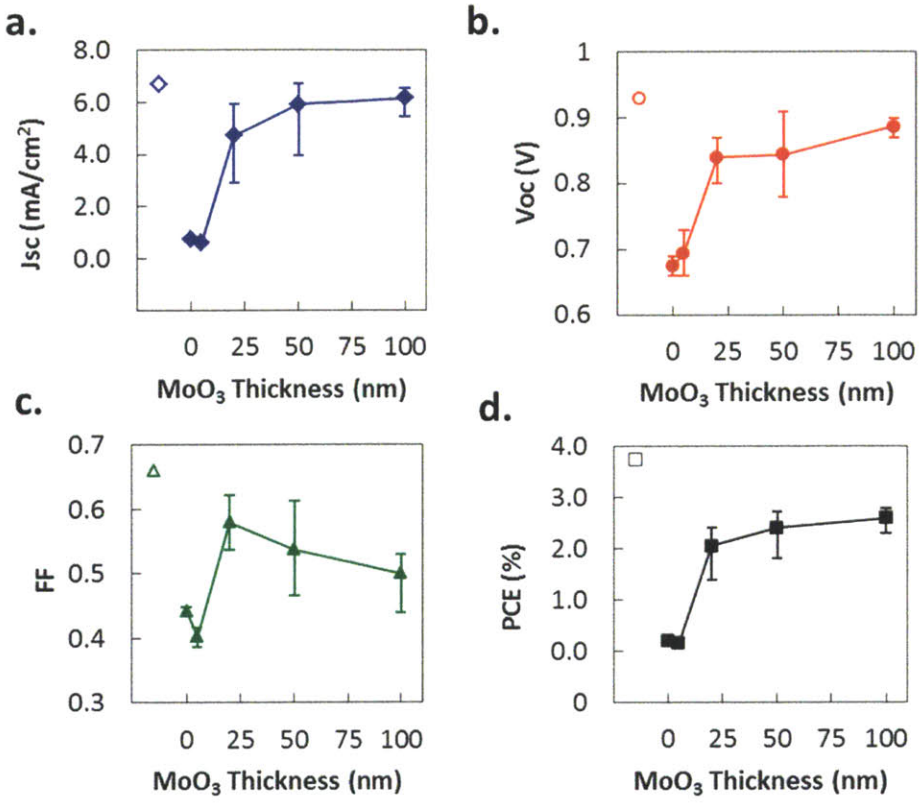

Figure 4-4: Performance parameters for top-illuminated cells (solid symbols) with different MoO_3 buffer layer thicknesses, measured under 1.1 sun illumination: (a) short-circuit current density (blue diamonds), (b) open-circuit voltage (red circles), (c) fill factor (greed triangles), and (d) power conversion efficiency (black squares). The conventional, bottom-illuminated cell with ITO anode and 20 nm MoO_3 is shown for reference at x=-15 (open symbols). Data points are the average of 3-5 devices measured across each substrate, and error bars represent the maximum and minimum values recorded.

Finally, devices were fabricated and tested on a number of common opaque substrates to demonstrate the wide applicability of this top-illuminated architecture (Figure 4-5). Opaque substrates, made from everyday consumer products were selected, included photo paper, magazine print, US first-class stamp, and plastic food packaging. The OPV devices were fabricated and tested in the same way as the cells on glass substrates with a 20 nm MoO_3 buffer layer, and all substrates were used as purchased. The ability to seamlessly transition from fabrication on glass to paper substrates is made possible by avoiding high

temperatures and solvent wetting challenges in this all-dry process. Notably, the *J-V* performance curves (Figure 4-5a) show that inverting the orientation of illumination results in photocurrents (J_{SC}) that match closely with that of the cell on the transparent glass substrate, despite the low substrate transparency. This represents a significant improvement over our previous demonstrations of bottom-illuminated oCVD PEDOT OPVs on paper substrates, which suffered from low photocurrents due to the low optical transmittance of paper substrates.[6] The low *FF* for the device on magazine print is a due to low shunt resistance observable in the *J-V* at zero bias, and likely due to shorting pathways across the thin semiconductor active layers in areas of high surface roughness.[6]

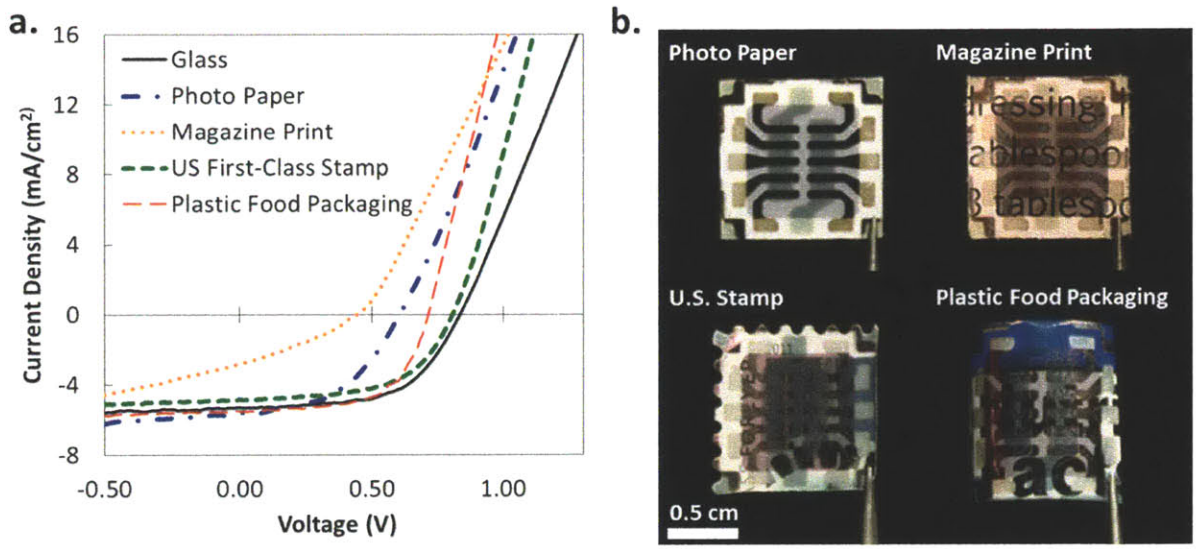

Figure 4-5: (a) Representative J-V curves for top-illuminated OPVs fabricated on the top side of some common opaque substrates under 1.1 sun illumination, including photo paper, magazine print, a U.S. first-class stamp, plastic food packaging, and glass for reference. (b) Photographs of completed 10 device arrays are also shown. All substrates were used as purchased, so the original surface images are visible in the spaces below the completed PV devices (i.e., printed text, Statue of Liberty image, and "Nutritional Facts" text, respectively).

A summary of the performance parameters for these devices are listed in . The efficiency observed here on paper substrates (2.0%) has a performance just over half of the optimized conventional ITO device on glass (3.7%) with the same active layer materials, and is the best reported to date for an OPV on a fibrous paper substrate.[6-8, 45, 46]

Table 4-2: Summary of performance parameters under 1.1 sun illumination for devices on common opaque substrates (Figure 4-5).

Device	J_{sc} (mA/cm^2)	V_{oc} (V)	FF	PCE (%)
Photo Paper	5.7	0.61	0.47	1.5
Magazine Print	2.8	0.45	0.31	0.4
U.S. Stamp	4.8	0.81	0.57	2.0
Plastic Food Package	5.5	0.72	0.61	2.2

4.5 Conclusion

We have demonstrated top-illuminated organic photovoltaics, employing a poly(3,4-ethylenedioxythiophene) (PEDOT) polymer anode deposited by oxidative chemical vapor deposition (oCVD) on top of a small-molecule organic heterojunction based on vacuum-evaporated DBP as the electron donor and fullerene C_{60} as the electron acceptor. A MoO_3 buffer layer between the oCVD PEDOT top electrode and DBP donor layer is shown to increase the device photocurrent nearly 10 times by preventing oxidation of the underlying photoactive DBP electron donor layer during the oCVD PEDOT deposition, and results in power conversion efficiencies of up to 2.8% for the top-illuminated, ITO-free devices, approximately 75% that of the conventional cell architecture with indium-tin oxide (ITO) transparent anode (3.7%). We also demonstrate the broad applicability of this architecture by fabricating devices on a variety of opaque substrates, including common paper products with ~2.0% power conversion efficiency. By replacing the single-junction bilayer cell used here with tandem and bulk heterojunction structures available today, we expect efficiencies in excess of 5% are possible on opaque paper-based substrates without any pretreatment or special manufacturing processes. This demonstrates the near-term potential for deploying organic photovoltaics in the form of everyday opaque substrates, thus adding energy harvesting functionality to otherwise passive products, such as wall and window coverings, product packaging, documents, and apparel.

4.6 Acknowledgments

This work was supported by Eni, S.p.A (Italy) through the MIT Energy Initiative Program. This research was also supported in part by the Department of Energy Office of Science Graduate Fellowship Program (DOE SCGF), made possible in part by the American Recovery and Reinvestment Act of 2009, administered by ORISE-ORAU under contract no. DE-AC05-06OR23100.

4.7 References

1. M. C. Barr, R. M. Howden, R. R. Lunt, V. Bulovic and K. K. Gleason, *Advanced Energy Materials*, 2012, **2**, 1404-1409.
2. <http://www.heliatek.com/?p=1923&lang=en>, Accessed June 1, 2012.
3. S. R. Forrest, *Nature*, 2004, **428**, 911-918.
4. R. D. McCullough, *Advanced Materials*, 1998, **10**, 93-116.
5. C. J. Brabec, S. Gowrisanker, J. J. M. Halls, D. Laird, S. J. Jia and S. P. Williams, *Advanced Materials*, 2010, **22**, 3839-3856.
6. M. C. Barr, J. A. Rowehl, R. R. Lunt, J. Xu, A. Wang, C. M. Boyce, S. G. Im, V. Bulović and K. K. Gleason, *Advanced Materials*, 2011, **23**, 3500-3505.
7. A. Hübler, B. Trnovec, T. Sillger, M. Ali, N. Wetzold, M. Mingebach, A. Wagenpfahl, C. Deibel and V. Dyakonov, *Advanced Energy Materials*, 2011, **1**, 1018-1022.
8. D. Tobjork and R. Osterbacka, *Advanced Materials*, 2011, **23**, 1935-1961.
9. U. Zschieschang, T. Yamamoto, K. Takimiya, H. Kuwabara, M. Ikeda, T. Sekitani, T. Someya and H. Klauk, *Advanced Materials*, 2010, **23**, 654-+.
10. L. Nyholm, G. Nyhström, A. Mihranyan and M. Strømomme, *Advanced Materials*, 2011, **XX**, 1-19.
11. A. C. Siegel, S. T. Phillips, M. D. Dickey, N. S. Lu, Z. G. Suo and G. M. Whitesides, *Advanced Functional Materials*, 2010 **20**, 28-35.
12. S. K. Hau, H.-L. Yip and A. K. Y. Jen, *Polymer Reviews*, 2010, **50**, 474-510.
13. X. Tong, B. E. Lassiter and S. R. Forrest, *Organic Electronics*, 2010, **11**, 705-709.
14. F.-C. Chen, J.-L. Wu, C.-L. Lee, W.-C. Huang, H.-M. P. Chen and W.-C. Chen, *Ieee Electron Device Letters*, 2009, **30**, 727-729.
15. R. R. Lunt and V. Bulovic, *Applied Physics Letters*, 2011, **98**.
16. S. K. Hau, H.-L. Yip, J. Zou and A. K. Y. Jen, *Organic Electronics*, 2009, **10**, 1401-1407.
17. J. Meiss, M. K. Riede and K. Leo, *Journal of Applied Physics*, 2009, **105**.
18. S.-I. Na, S.-S. Kim, J. Jo and D.-Y. Kim, *Advanced Materials*, 2008, **20**, 4061-+.
19. J. Meiss, N. Allinger, M. K. Riede and K. Leo, *Applied Physics Letters*, 2008, **93**.
20. J. Meiss, M. K. Riede and K. Leo, *Applied Physics Letters*, 2009, **94**.
21. C. Tao, G. Xie, C. Liu, X. Zhang, W. Dong, F. Meng, X. Kong, L. Shen, S. Ruan and W. Chen, *Applied Physics Letters*, 2009, **95**.
22. R. Po, C. Carbonera, A. Bernardi and N. Camaioni, *Energy & Environmental Science*, 2011, **4**, 285-310.
23. S. Kirchmeyer and K. Reuter, *Journal of Materials Chemistry*, 2005, **15**, 2077-2088.
24. Y.-S. Hsiao, C.-P. Chen, C.-H. Chao and W.-T. Whang, *Organic Electronics*, 2009, **10**, 551-561.
25. M. Glatthaar, M. Niggemann, B. Zimmermann, P. Lewer, M. Riede, A. Hinsch and J. Luther, *Thin Solid Films*, 2005, **491**, 298-300.
26. J. Ajuria, I. Etxebarria, W. Cambarau, U. Munecas, R. Tena-Zaera, J. Carlos Jimeno and R. Pacios, *Energy & Environmental Science*, 2011, **4**, 453-458.
27. F. Nickel, A. Puetz, M. Reinhard, H. Do, C. Kayser, A. Colsmann and U. Lemmer, *Organic Electronics*, 2010, **11**, 535-538.
28. J. P. Lock, S. G. Im and K. K. Gleason, *Macromolecules*, 2006, **39**, 5326-5329.
29. M. E. Alf, A. Asatekin, M. C. Barr, S. H. Baxamusa, H. Chelawat, G. Ozaydin-Ince, C. D. Petruczok, R. Sreenivasan, W. E. Tenhaeff, N. J. Trujillo, S. Vaddiraju, J. Xu and K. K. Gleason, *Advanced Materials*, 2010, **22**, 1993-2027.
30. S. H. Baxamusa, S. G. Im and K. K. Gleason, *Phys Chem Chem Phys*, 2009, **11**, 5227-5240.
31. D. Fujishima, H. Kanno, T. Kinoshita, E. Maruyama, M. Tanaka, M. Shirakawa and K. Shibata, *Solar Energy Materials and Solar Cells*, 2009, **93**, 1029-1032.

32. S. G. Im, K. K. Gleason and E. A. Olivetti, *Applied Physics Letters*, 2007, **90**, 152112.
33. S. G. Im and K. K. Gleason, *Macromolecules*, 2007, **40**, 6552-6556.
34. G. Li, C. W. Chu, V. Shrotriya, J. Huang and Y. Yang, *Applied Physics Letters*, 2006, **88**.
35. V. Shrotriya, G. Li, Y. Yao, C. W. Chu and Y. Yang, *Applied Physics Letters*, 2006, **88**.
36. D. Y. Kim, J. Subbiah, G. Sarasqueta, F. So, H. Ding, Irfan and Y. Gao, *Applied Physics Letters*, 2009, **95**.
37. H. Y. Chen, J. H. Hou, S. Q. Zhang, Y. Y. Liang, G. W. Yang, Y. Yang, L. P. Yu, Y. Wu and G. Li, *Nature Photonics*, 2009, **3**, 649.
38. I. Hancox, K. V. Chauhan, P. Sullivan, R. A. Hatton, A. Moshar, C. P. A. Mulcahy and T. S. Jones, *Energy & Environmental Science*, 2010, **3**, 107-110.
39. C. Tao, S. Ruan, X. Zhang, G. Xie, L. Shen, X. Kong, W. Dong, C. Liu and W. Chen, *Applied Physics Letters*, 2008, **93**.
40. Y. Sun, C. J. Takacs, S. R. Cowan, J. H. Seo, X. Gong, A. Roy and A. J. Heeger, *Advanced Materials*, 2011, **23**, 2226-+.
41. P. Peumans, A. Yakimov and S. R. Forrest, *Journal of Applied Physics*, 2003, **93**, 3693-3723.
42. G. Parthasarathy, P. E. Burrows, V. Khalfin, V. G. Kozlov and S. R. Forrest, *Applied Physics Letters*, 1998, **72**, 2138-2140.
43. Y. Kinoshita, R. Takenaka and H. Murata, *Applied Physics Letters*, 2008, **92**.
44. S. G. Im, K. K. Gleason and E. A. Olivetti, *Applied Physics Letters*, 2007, **90**.
45. B. Lamprecht, R. Thunauer, M. Ostermann, G. Jakopic and G. Leising, *Physica Status Solidi a-Applications and Materials Science*, 2005, **202**, R50-R52.
46. F. Wang, Z. J. Chen, L. X. Xiao, B. Qu and Q. H. Gong, *Solar Energy Materials and Solar Cells*, 2010, **94**, 1270-1274.

CHAPTER FIVE

Optimizing PEDOT film conductivity: solution and vapor processing techniques

5.1 Introduction

One of the most important properties for a transparent conductor material (whether it be an electrode or buffer layer within a device) is the tradeoff between transparency and conductivity. The films must thin enough to limit losses from optical absorption yet be thick enough to provide low enough sheet resistance to effectively transport or extract charge. The desired optical and electrical requirements for transparent electrode materials are transmittance (T) >90% and sheet resistance R_{sh}< 100 Ω sq^{-1}. Conducting polymer films such as PEDOT have a less desirable trend between transmittance and film conductivity or sheet resistance than standard metal oxide transparent conductor layers.[1]

Researchers are working to improve this relationship by optimizing film conductivities using a number of different processing techniques. The method by which these improvements are made depends heavily on the methods used for synthesis and fabrication of the polymer films. This section details methods of conductivity enhancement that have been investigated both for solution and vapor-processed PEDOT films.

5.2 Solution Processing

The most common method of depositing PEDOT layers for organic electronic devices is to spin coat the layer from a PEDOT:PSS solution in water. The PSS chains allow the PEDOT to be soluble in water and act as a counterion allowing the PEDOT chains to conduct charge. After film deposition, pristine PEDOT:PSS layers typically have a relatively low conductivity (often < 1 S/cm).[2, 3] Additives and various processing techniques have been employed by researchers to reach values well over 1000 S/cm.[4-7] Generally when PEDOT:PSS is deposited, phase segregation between the PEDOT and PSS occurs, as often takes place with multi-component solutions. More conductive PEDOT regions/particles are observed (10-50 nm) embedded in a less conductive PSS matrix.[8] Molecular weight measurements are difficult due to the insolubility of PEDOT films. PEDOT derivatives with soluble long-chain ethers PEDOT-CH_2O-n-$C_{14}H_{29}$ and PEDOT-CH_2O-n-$C_{16}H_{33}$ could be analyzed by GPC and were found to have molecular weights of 12,900 and 14,300, respectively, with polydispersity of 1.45 and 1.65.[9] Smaller molecular weights of ~1500 have been obtained by GPC for lower conductivity films formed by oxidative polymerization.[10] Tran-Van et al. demonstrate how UV-vis, Raman, and FTIR spectroscopy may be used to observe the distribution in conjugation length for short PEDOT oligomers.[10]

The observed dependence on temperature of PEDOT:PSS film conductivity has led researchers to conclude that lateral conductivity occurs by hopping of charge carriers.[11-13] Nardes et al. investigated

anisotropic charge conduction behavior in PEDOT films. Vertical conductivity (perpendicular to the substrate) measurements were conducted by spin-coating films onto a gold electrode and the evaporating another gold electrode on the top surface of the PEDOT:PSS film.[14]

Much of the recent effort that has gone into investigating solution processed PEDOT:PSS has focused on improving the film conductivity. Though the PSS chains enhance processibility, the PSS chains are bulky and get in the way of charge transfer between PEDOT segments.[14, 15] The most common method of improving PEDOT:PSS conductivity has been incorporating additives, such as high boiling point solvents, into the aqueous solution before depositing the film. Some of the commonly used additives include sorbitol, ethylene glycol, and DMSO. For example, Dimitriev et al. explored DMSO and EG as additives ranging from 0 to 8 wt% in the initial solution and observed maximum conductivities at around 5 wt% (1.7 S/cm and 1.3 S/cm for DMSO and EG, respectively).[3] They found that adding the additives before casting led to poor control over film morphology and conductivity. The authors also explored introducing the organic solvents by vapor exposure, which gave more control over film conductivity and did not impact film morphology. Vapor exposure allowed the film to reach saturation levels of DMSO, which directly correlated with film conductivity.

There are differing opinions on the exact mechanism of conductivity enhancement using these solvents. For example, Kim et al. observed a relationship between the dielectric constant of the additive and the conductivity enhancement and suggested the remaining additives may provide a screening effect between the PEDOT and PSS chains[16], while Inganäs et al. proposed that the additive may act as a plasticizer aiding in chain rearrangement at higher temperatures.[17] These additives have been found to affect final chain packing. Some researchers have performed VASE and FTIR analysis that shows that the additives do not remain within the film after annealing yet there is a lasting improvement to the PEDOT:PSS conductivity as a result of increased chain packing.[17, 18] The evidence of changes in morphology includes a measured decrease in optical anisotropy and AFM images suggesting swelling and aggregation of the polymer particles during film formation leading to improved connectivity between conductive regions, which results in an improved charge percolation network. Other studies have seemed to indicate that some of the solvent does indeed remain within the film and can act as a secondary dopant or causes a dopant exchange with the PSS chains.[3, 11] Ouyang et al.[11] investigated PEDOT:PSS films treated with a number of organic solvents (ethylene glycol, DMSO, NMP, N,N-dimethylacetomide, 4-methoxyphenol, acetonitrile, cyclohexone, nitromethane, methyl alcohol, and pyridine) and they found that the enhancement in conductivity strongly depended on the chemical

structure of the organic compound. No conductivity enhancement was observed for organic compounds with only one polar group, such as acetonitrile. The compounds that had the most significant effect on conductivity were those with two or more polar groups. Ouyang et al. proposed that the primary mechanism for the chain in PEDOT chain morphology was the interaction between the dipoles of the organic compounds and the positive charges on the PEDOT chains. The largest value of conductivity (200 S/cm) was found using ethylene glycol. Morphology analysis generally shows that the PEDOT:PSS structure changed from coil to chain structure or that the conductive regions swell and expand to create a larger charge percolation network within the films, hence enhancing film conductivity.[8, 11, 19, 20] The deposited films are often no longer soluble in water after these morphological affects have taken place.

Another important treatment that has been explored is film annealing, often in combination with testing the film additives. There is variation in the results seen by different researchers with annealing the films as well. For example some researchers have shown that at higher temperatures, annealing can actually reduce the film conductivity. [3] The mechanism of degradation here was thought to be shrinking of the conducting grains, thus creating larger distances over which charge hopping must occur. Xiong and Liu found that annealing glycerol doped films improved film conductivity at temperatures below 225 °C.[21] Nardes et al. demonstrated that PEDOT:PSS films treated with sorbitol exhibited a steady increase in film conductivity until the conductivity saturated at ~160 C°. The conductivity enhancement here was thought to be the result of sorbitol and remaining water in the film enabling morphological changes in the PEDOT:PSS film. The authors showed that the evaporation of sorbitol and residual water begins at approximately 80 °C. Enhanced stability, as evidenced by reduced water uptake post-annealing, was attributed to denser chain packing.[22]

Researchers have also investigated post treatment rinsing of dried films. Kim et al. investigated the effect of post treatment time on dry films rinsed in an ethylene glycol bath for several minutes then dried. They found a maximum conductivity of 1418 S cm^{-1} using a treatment time of 30 minutes. Optical and thickness measurements indicate that increasing treatment time leads to increasing removal of PSS from the film. AFM images show larger PEDOT-rich granular networks for the higher conductivity films.[6]

Another method of forming PEDOT films through solution processing is through electropolymerization. Researchers investigating crystallinity and surface morphology of PEDOT films formed by electrochemical synthesis found that they could tune the crystallinity from dense amorphous films to porous crystalline films by varying the switching potential during polymerization.[23]

It is possible that some of the principles and treatments that have been explored for solution-processed films could be modified and applied to vapor-deposited PEDOT films. May of the same characterization techniques are used to study the film properties (e.g. Raman and FTIR, conductivity measurements, XRD, AFM) while it is difficult for both vapor-processed and irreversibly treated solution-processed films to be characterized by techniques most commonly performed in solution (e.g. GPC). The use of stronger solvents or a modified monomer with side chain may allow for analysis of molecular weights.

5.3 Vapor Processing

5.3.1 Vapor Phase Polymerization (VPP)

Another common method for depositing PEDOT layers is through vapor phase polymerization (VPP). VPP differs from oCVD in the oxidant delivery method. In VPP, a solution containing an oxidizing agent, most commonly iron (III) tosylate, $Fe(TOS)_3$, is spin coated onto a bare substrate. The substrate is then exposed to EDOT monomer in a controlled vacuum chamber and a polymer film grows (Figure 5-1).

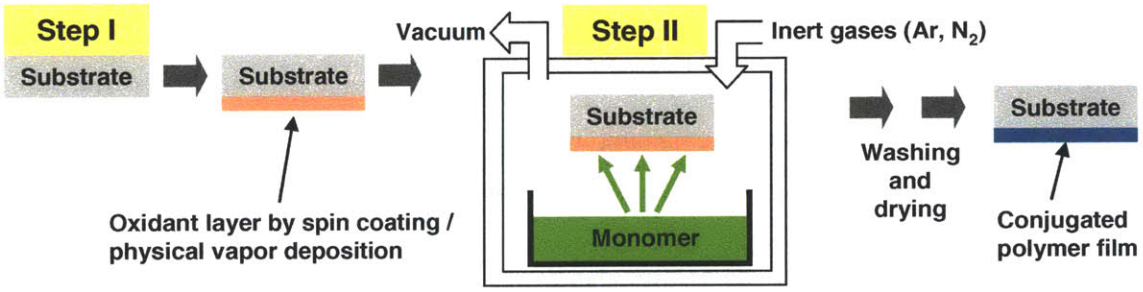

Figure 5-1: Typical procedure for vapor phase polymerization of PEDOT

Considerable work has been done to investigate the growth mechanism in VPP and many studies have also been conducted to vary process parameters to enhance PEDOT film conductivity.[24]

A systematic study of the effects of the reaction pressure and monomer temperature for VPP of EDOT was conducted by Fabretto et al.[25] The change in mass upon EDOT polymerization, i.e. growth rate of the PEDOT film, was recorded by a QCM for a range of operating pressures (1.5 to 10 kPa). The observed rate of polymerization was found to increase by lowering operating pressure. In a parallel experiment, when the temperature of the EDOT containing crucible was decreased from 80°C to 35°C, the maximum conductivity was achieved between 45°C and 55°C. Higher temperatures resulted in an increased rate of

polymerization, while too low a temperature produced a slow growth rate resulting in a patchy film. The researchers hypothesized that a slower polymerization rate would allow more time for the chains to arrange themselves in a more favorable orientation.

Much of the work to optimize the conductivity of VPP PEDOT films has focused on using additives in the pre-spun oxidant solution that then impact the polymerization. Specifically, organic bases such as pyridine and imidazole, have been shown to slow the rate of polymerization and result in increased electrical conductivity.[26, 27] Incorporation of a surfactant such as poly(ethylene glycol)-ran-poly(propylene glycol) (PEG-ran-PPG) to the oxidant solution inhibits the adverse effects of water absorption and prevents the oxidant from forming crystallite domains during the VPP process resulting in a significant increase in the conductivity.[28, 29] It is believed that PEG-ran-PPG coordinates to the Fe^{3+} ions in the oxidant iron(III) tosylate and reduces the effective reactivity of the oxidant, which reduces the rate of polymerization leading to increased conductivity.[29] More recent work utilized a structure-directing template by adding the block copolymer 5800 Da poly(ethylene glycol–propylene glycol–ethylene glycol) (PEG-PPG-PEG). Morphology changes indicated a sheet-like structure of the PEDOT films. Conductivity values as high as 3400 S/cm were achieved.[30] Further studies revealed that the surfactant can potentially replace the weak bases such as pyridine and imidazole in reducing the apparent reactivity of the oxidant, thus eliminating the problems associated with volatility of low molecular weight organic bases.[31]

Just as post-deposition treatments are often done for solution processed polymer layers, a number of pretreatments may also be considered for vapor deposited films including annealing, chemical rinsing or dopant exchange, plasma treatment, UV exposure, and possibly many others. Films deposited via VPP or oCVD are often rinsed with methanol or ethanol to remove unreacted monomer or oxidant as well as short oligomers and byproducts remaining after the polymerization.[32, 33] Films may be dried before or after this rinsing step either in ambient conditions or in the presence of an inert gas. Annealing at temperatures in excess of 80 °C has shown significant degradation of VPP PEDOT films, characterized by a drop in conductivity and work function. Films annealed at 200 °C saw a decrease in conductivity from 870 S cm^{-1} to 290 S cm^{-1} after just 10 minutes, whereas this effect was less pronounced for films annealed at 80 °C, falling from 870 S cm^{-1} to 770 S cm^{-1} over the same time period.[34]

Since VPP is closer in nature to the oCVD film synthesis mechanism it may be especially useful to evaluate conductivity enhancement techniques employed during VPP and try to apply them to oCVD, especially the idea of using chemicals or process conditions to have *in situ* control over film morphology.

5.3.2 Oxidative Chemical Vapor Deposition (oCVD)

The process conditions during oCVD can have a large impact on the final film's electrical properties. The substrate temperature during the oCVD process has been found to have a significant effect on the conductivity of the deposited polymer. The electrical conductivity of oCVD PEDOT films substantially increases as the substrate temperature increases from 15°C - 110°C keeping the other processing parameters identical. The Arrhenius plot of conductivity with the substrate temperature revealed an apparent single activation energy of 28.1 ±1.1 kcal mol^{-1}. The trend observed in conductivity was in accordance with the optical and chemical properties of the corresponding oCVD PEDOT films. It showed that increased substrate temperature resulted polymers with longer conjugation length and higher doping level which helped obtain higher electrical conductivity.[33, 35, 36]

The post-deposition rinsing of oCVD films has also been investigated as a method to improve film conductivity. Films are often rinsed in methanol as a way of removing residual oxidant or unreacted monomer. Rinsing also results in a much smoother film surface. Acid rinsing has also been explored as a way to not only more effectively remove residual oxidant but also to improve the final film conductivity.[37] The reason for the observed conductivity enhancement was thought to be a combination of increased doping and improved chain packing. More work can certainly be done to explore the impact of different rinsing solutions and parameters such as rinsing temperature and time. For example, rinsing too quickly after films have been removed from the deposition chamber has been noted to have an adverse effect on the conductivity. For the acid rinsing treatment, some preliminary results suggest that the method depicted in Figure 5-2, produces smooth, high conductivity films without the water/solvent spots sometimes left behind on the film surface when drying at room temperature after the acid rinsing. With this method the acid rinse solution is dropped onto the heated PEDOT film using a pipette and then allowed to dry and further anneal for an hour. The film is then rinsed in methanol to remove residual materials dried on the film surface. Besides leaving a cleaner, smoother surface, the heating steps could potentially have an added benefit on the film morphology beyond what was originally explored in Chapter 2 as annealing has often been shown in the literature to have an impact on polymer film morphology. The heat applied during the rinsing step could also aid in the mobility of the chains and dopant molecules.

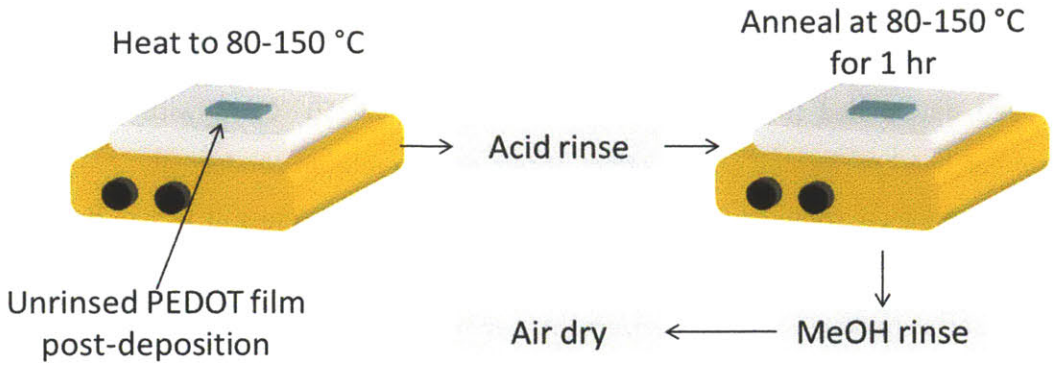

Figure 5-2: Schematic of recommended film rinsing process to be explored

The parameters of the rinsing process (temperatures, times, ambient conditions, etc.) can be altered and optimized to produce higher conductivity films.

5.4 Discussion and Recommendations

Conductivity enhancements for both solution-processed and vapor-deposited PEDOT films generally focus on the morphological effects of post-treatment by solvents or annealing or the process conditions and chemical additives during deposition.

It is likely that some of the strategies for improving solution-processed PEDOT:PSS could be employed to improve the conductivity of vapor-deposited PEDOT films. Since oCVD PEDOT does not contain the bulky PSS regions, the primary factors that should affect the film conductivity are the chain length, doping concentration, and the morphology of the chain packing. Stability is another important issue for integration into optoelectronic devices. Longer chain lengths and tighter chain packing should reduce the need for hopping conduction and lead to more conductive films. For oCVD, these effects have already been demonstrated to some extent by showing that higher substrate temperatures during polymerization leads to higher conductivities, presumably as a result of longer chain lengths,[33] and by performing acid rinsing on films, which removes residual materials and gives a more crystalline structure, leading to higher conductivities.[37] Perhaps the most useful pursuit in trying to improve oCVD film conductivity would be exploring the effects of annealing (temperature, time, and environment). It would also be interesting to explore what effect vapor exposure to various solvents, including those used as additives in solution-processed PEDOT:PSS such as EG and DMSO, has on oCVD films, perhaps in conjunction with annealing treatments. It may also be useful to investigate the effects of varying temperature during rinsing treatments with acids or other types of solvents.

Another potential avenue for exploration is the variation of process conditions to optimize film conductivity. For instance, the maximum temperature at which a reasonable film growth rate still occurs has not been determined (films typically grown between 80-150 °C. As with VPP PEDOT, some exploration has been performed on the effect of film growth rate on conductivity. Preliminary results seem to indicate higher conductivities for films with slower growth rates. It is hypothesized that the improvement is either due to morphological effects from slower growth (e.g. giving chains more time to arrange with better packing) or the improvement may be a result of altering the relative flow rates of oxidant and monomer. It was noted that large differences in the relative flow rates (i.e. a high monomer flow rate with a low oxidant flow rate or a low monomer flow rate with a high oxidant flow rate) led to poor film quality (lower conductivities or too much residual oxidant). Better films were produced when the relative flow rates matched (low monomer flow rate with low oxidant flow rate or in cases where both the monomer and oxidant flow were moderate or high). Controlling the oxidant by a constant power input to ramp temperature slowly, as opposed to giving a temperature set point, has allowed slower delivery and more control over oxidant flow to the substrate.

The choice of oxidant is another important factor for the film characteristics. The fact that thermally evaporated oxidants such as $FeCl_3$ leave residual materials behind, necessitating rinsing steps and perhaps hindering tightly-packed film growth, may make moving to a more volatile liquid oxidant an attractive option. The size of the dopant molecules should be considered as they may impact chain packing and stability. The exact mechanisms of film degradation are still under investigation for both solution and vapor-processed films. A likely hypothesis is that tighter chain packing provides a better barrier to environmental moisture and thereby produces more stable films.

It is recommended in future experiments to use a quartz crystal microbalance (QCM) or other technique for measuring the $FeCl_3$ flow rate and potentially the film growth rate as well. The oxidant flow rate may then be calibrated to the power and temperature set points of the crucible heater controller. Another potential option to improve conductivity may be to perform a second oxidation step either during the rinsing phase or by running a second deposition with a different substrate temperature and/or oxidant flow rate.

One option that has not yet been explored in oCVD is to flow a volatile chemical during the polymerization to enable or force better chain alignment. Alternatively, a surface treatment could be done on the substrate to help structure film growth. Exploring the block copolymers PEG-PPG-PEG that

have been so successful in improving VPP PEDOT films would be a logical first step in trying to improve the structure of oCVD PEDOT films.

5.5 Conclusions

Controlling film morphology is an important tool for further optimization of the electrical properties of oxidative chemical vapor deposited PEDOT films. Some preliminary work has been done in the area but further experimentation and developing new strategies for controlling the film morphology are important next steps. Various techniques have been explored in solution-processing PEDOT:PSS and in vapor phase polymerization of PEDOT that may be applicable to the oCVD process. It is recommended that future work looks at systematically exploring both established and novel techniques as they can be applied to oCVD. The results of exploring these techniques for PEDOT films should be applicable to other polymers or copolymers deposited via oCVD, morphology concerns being especially important for semiconducting polymers used in optoelectronic applications.

5.6 References

1. M. C. Barr, J. A. Rowehl, R. R. Lunt, J. Xu, A. Wang, C. M. Boyce, S. G. Im, V. Bulović and K. K. Gleason, *Advanced Materials*, 2011, **23**, 3500-3505.
2. A. Elschner, S. Kirchmeyer, W. Lovenich, U. Merker and K. Reuter, *PEDOT: Principles and Applications of an Intrinsically Conductive Polymer*, CRC Press, Boca Raton, FL, 2011.
3. O. P. Dimitriev, D. A. Grinko, Y. V. Noskov, N. A. Ogurtsov and A. A. Pud, *Synthetic Metals*, 2008, **159**, 2237-2239.
4. Y. Xia, K. Sun and J. Ouyang, *Energy & Environmental Science*, 2012, **5**, 5325-5332.
5. Y. Xia, K. Sun and J. Ouyang, *Advanced Materials*, 2012, **24**, 2436-2440.
6. Y. H. Kim, C. Sachse, M. L. Machala, C. May, L. Müller-Meskamp and K. Leo, *Advanced Functional Materials*, 2011, **21**, 1076-1081.
7. Y. Xia and J. Ouyang, *Organic Electronics*, 2012, **13**, 1785-1792.
8. S. Timpanaro, M. Kemerink, F. J. Touwslager, M. M. De Kok and S. Schrader, *Chemical Physics Letters*, 2004, **394**, 339.
9. P. Schottland, O. Stéphan, P.-Y. Le Gall and C. Chevrot, *J. Chim. Phys.*, 1998, **95**, 1258-1261.
10. F. Tran-Van, S. Garreau, G. Louarn, G. Froyer and C. Chevrot, *Journal of Materials Chemistry*, 2001, **11**, 1378-1382.
11. J. Ouyang, Q. Xu, C.-W. Chu, Y. Yang and J. Shinar, *Polymer*, 2004, **45**, 8443.
12. A. N. Aleshin, R. Kiebooms, H. Yu, M. Levin and I. Shlimak, *Synthetic Metals*, 1998, **94**, 157-159.
13. J. Huang, P. F. Miller, J. S. Wilson, A. J. de Mello, J. C. de Mello and D. D. C. Bradley, *Advanced Functional Materials*, 2005, **15**, 290-296.
14. A. M. Nardes, M. Kemerink, R. A. J. Janssen, J. A. M. Bastiaansen, N. M. M. Kiggen, B. M. W. Langeveld, A. J. J. M. van Breemen and M. M. de Kok, *Advanced Materials*, 2007, **19**, 1196-1200.
15. T. Stocker, A. Kohler and R. Moos, *Journal of Polymer Science B: Polymer Physics*, 2012, **50**, 976-983.
16. J. Y. Kim, J. H. Jung, L. D. E. and J. Joo, *Synthetic Metals*, 2002, **126**, 311.
17. L. A. A. Pettersson, S. Ghosh and O. Inganas, *Organic Electronics*, 2002, **3**, 143.

18. H. J. Snaith, H. Kenrick, M. Chiesa and R. H. Friend, *Polymer*, 2005, **46**, 2573-2578.
19. S. K. M. Jonsson, J. Birgerson, X. Crispin, G. Greczynski, W. Osikowica, A. W. D. van der Gon, W. R. Salaneck and M. Fahlman, *Synthetic Metals*, 2003, **139**, 1.
20. E. Vitoratos, S. Sakkopoulos, E. Dalas, N. Paliatsas, D. Karageorgopoulos, F. Petraki, S. Kennou and S. A. Choulis, *Organic Electronics*, 2009, **10**, 61-66.
21. Z. Xiong and C. Liu, *Organic Electronics*, 2012, **13**, 1532-1540.
22. A. M. Nardes, M. Kemerink, M. M. de Kok, E. Vinken, K. Maturova and R. A. J. Janssen, *Organic Electronics*, 2008, **9**, 727-734.
23. L. Niu, C. Kvarnstrom, K. Froberg and A. Ivaska, *Synthetic Metals*, 2001, **122**, 425-429.
24. D. Bhattacharyya, R. M. Howden, D. Borrelli and K. K. Gleason, *Journal of Polymer Science B: Polymer Physics*, 2012, **50**, 1329-1351.
25. M. Fabretto, J. P. Autere, D. Hoglinger, S. Field and P. Murphy, *Thin Solid Films*, 2011, **519**, 2544-2549.
26. J. P. Lock, S. G. Im and K. K. Gleason, *Macromolecules*, 2006, **39**, 5326-5329.
27. B. Winther-Jensen, D. W. Breiby and K. West, *Synthetic Metals*, 2005, **152**, 1-4.
28. K. Zuber, M. Fabretto, C. Hall and P. Murphy, *Macromolecular Rapid Communications*, 2008, **29**, 1503-1508.
29. M. Fabretto, M. Mueller, K. Zuber and P. Murphy, *Macromolecular Rapid Communications*, 2009, **30**, 1846-1851.
30. M. V. Fabretto, D. R. Evans, M. Mueller, K. Zuber, P. Hojati-Talemi, R. D. Short, G. G. Wallace and P. J. Murphy, *Chemistry of Materials*, 2012, **24**, 3998-4003.
31. M. Fabretto, C. Jariego-Moncunill, J.-P. Autere, A. Michelmore, R. D. Short and P. Murphy, *Polymer*, 2011, **52**, 1725-1730.
32. B. Winther-Jensen and K. West, *Macromolecules*, 2004, **37**, 4538-4543.
33. S. G. Im, E. A. Olivetti and K. K. Gleason, *Surface and Coatings Technology*, 2007, **201**, 9406-9412.
34. P. A. Levermore, L. Chen, X. Wang, R. Das and D. D. C. Bradley, *Advanced Materials*, 2007, **19**, 2379-+.
35. S. G. Im and K. K. Gleason, *Macromolecules*, 2007, **40**, 6552-6556.
36. S. G. Im, K. K. Gleason and E. A. Olivetti, *Applied Physics Letters*, 2007, **90**, 152112-152113.
37. R. M. Howden, E. D. McVay and K. K. Gleason, *Journal of Materials Chemistry A*, 2013, **1**, 1334-1340.

CHAPTER SIX

The application of oxidative chemical vapor deposited (oCVD) PEDOT to textured and non-planar photovoltaic device geometries for enhanced light trapping

The work described in this chapter has been submit for publication to Organic Electronics[1]

6.1 Abstract

In organic photovoltaics (OPVs), active layer thicknesses are limited by exciton diffusion length. Thus, non-planar surfaces and device architectures are desired for enhancing the light absorption in OPVs. The oxidative chemical vapor deposition (oCVD) process enables the formation of conformal films of conducting polymers on complex surface structures. oCVD poly(3,4 ethylenedioxythiophene) (PEDOT) is demonstrated to be compatible with a wide range of nano- to macro-scale textured and non-planar architectures that have been demonstrated to enhance light absorption in photovoltaics by various mechanisms of light trapping, such as lengthening optical pathways and taking advantage of reflective light bouncing. Here, conformal oCVD (PEDOT) layers are demonstrated over submicron features including submicron nanowedges and nanocones (with 70-100 nm groove depth and 100 nm pitch) and square gratings (50-350 nm groove depth and 139-833.3 nm pitch). In contrast, solution-applied PEDOT:PSS exhibits blanketing, thinning at the top of the features, and welling up of material in the bottom of the features, thus failing to conformally coat the complex surfaces. The application of oCVD PEDOT to macro-scale 3D OPV architectures was also explored. Enhanced active layer absorbance is shown using tetraphenyldibenzoperiflanthene (DBP) as the absorbing layer over the PEDOT.

6.2 Introduction

Organic photovoltaics (OPVs) are being explored as a low-cost option for harvesting solar energy. The relatively low-energy process conditions make OPVs compatible with flexible substrates that can be used in fast, large-area roll-to-roll fabrication. One of the major drawbacks of OPVs, as compared to inorganic PVs, is lower light absorption[2]. Many recent studies have investigated textured features or gratings to enhance light absorption within the cell. Modeling using various techniques, such as rigorous coupled wave analysis (RCWA,[3-6] modification to the transfer matrix method, [7-9] and finite element modeling, [10, 11]has demonstrated improved light absorption by the cell active layers, and therefore an improved device efficiency for cells with various feature dimensions[12].

Various feature shapes and sizes have been explored including square or triangular trench gratings[3], pyramids [13] and cones, and non-uniform texturing[14]. Figure 6-1 shows examples of types of textures that could be utilized in photovoltaics to enhance light absorption. Some features are easier to fabricate, depending on the method of pattern formation and the materials being imprinted. The basic shape of the texture as well the relevant geometric parameters (e.g. height and spacing between features) will impact the absorption enhancement.

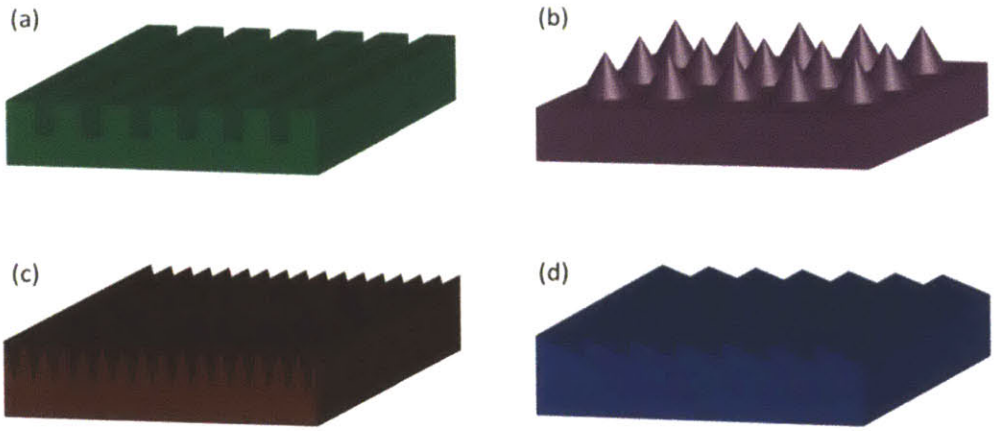

Figure 6-1: Examples of some of the variety of texturing geometries that may be explored for light trapping in photovoltaics. (a) square trenches (b) cones (c) triangular trenches (d) triangular groove geometry commonly used for reflection and transmission gratings

Researchers have also investigated the use of larger macro-scale 3D geometries to enhance light trapping and performance in photovoltaics[15, 16]. Figure 6-2 shows examples of non-planar device geometries that could be utilized to enhance light absorption. These 3-dimensional device structures are meant to enhance power output for a given area footprint.

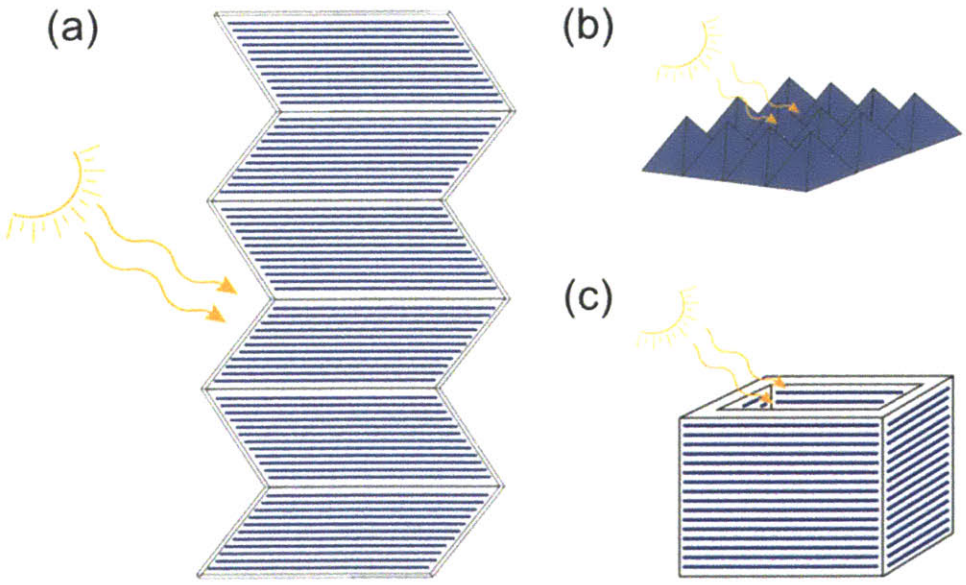

Figure 6-2: Examples of some of the variety of macro-scale 3D device structures that may be explored for light trapping in PV systems: (a) v-shaped fold tower, (b) pyramid structure, and (c) open-faced cube

The ideal geometry for a given device will depend on a number of factors, including the device layer structure, the choice of substrate, and the cell fabrication methods. Larger-scale pattern fabrication by

commercial imprint tools is already in use in semiconductor fabrication and the scaling up of replicating these patterns on polymers by hot embossing or injection molding is currently being explored[17, 18]. The optimal dimensions are highly dependent on the optical and physical properties of the material layers (e.g. complex refractive index and layer thickness). The thickness of the active layers for organic photovoltaics is limited by the exciton diffusion length within that material. In order to reduce losses due to recombination, the active layers are often made very thin (20-40 nm), which lowers their absorption[19]. Light trapping schemes can be especially effective for these thinner active layer cells[20]. One means by which having a structured device enhances light absorption is by decoupling the optical and electrical pathways within a device, as seen in Figure 6-3. Decoupling the optical and charge pathways can provide an effectively longer pathway for light absorption while maintaining a short pathway for charge separation.

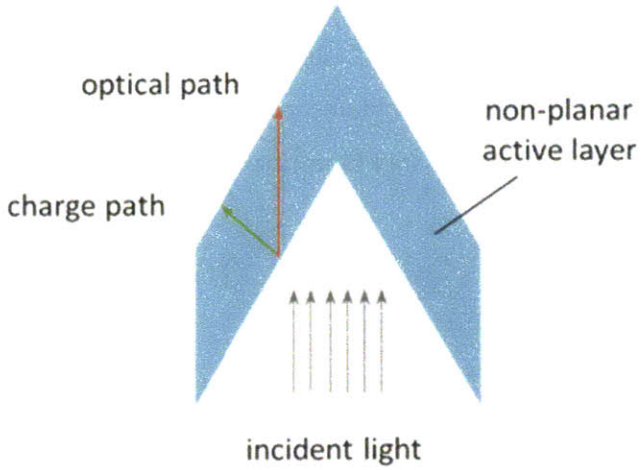

Figure 6-3: Diagram depicting decoupling of optical and charge pathways within an active layer with a non-planar structure

The light absorption enhancement predicted by modeling or observed experimentally can stem from a number of optical phenomenon. For example, some architectures are designed to scatter light, while others utilize an anti-reflection coating or an enhanced transmission grating to improve light transmission into the active layers. Other larger feature size structures take advantage of multiple reflection bounces to enhance light trapping. These behaviors are discussed in further detail in the following sections.

One of the main challenges for fabricating textured or 3D devices is obtaining films of uniform thickness which follow the contours of the non-planar substrates, so-called conformal coverage. As seen in work by various groups,[3, 4, 13, 21] conformally coating textured substrates or electrodes by solution processing

is challenging. In some cases, the coating solution wells up in the bottom of the feature while thinning along the sides and top of the feature. In other cases, the solution blankets the surface and does not fully penetrate the feature, as shown in Figure 6-4. Many factors are important for determining how conformal the films will be, including the geometric parameters of the features (shape and size), the rheology of the solutions, and the deposition process parameters (e.g. spin coating RPM). For the photoactive layers, nonconformal coverage can lead to an increase in recombination losses and shorting and for electrode or buffer layers, such as PEDOT:PSS, can lead to increased absorption losses and inferior charge extraction[12].

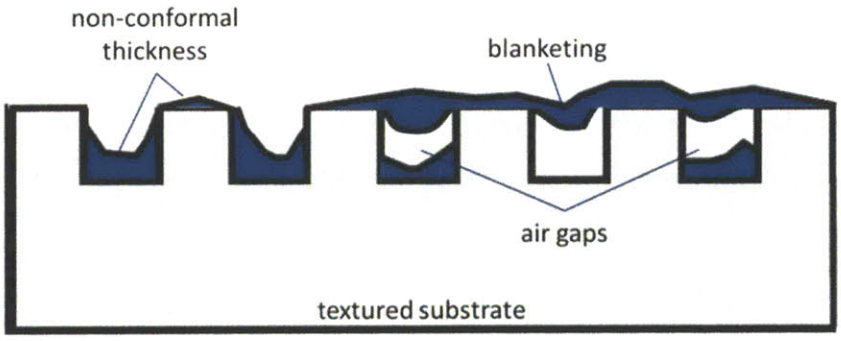

Figure 6-4: Diagram demonstrating potential problems with spin-coating a solution onto a textured surface

One solution to overcome these issues is to utilize vapor deposition techniques. Oxidative chemical vapor deposited (oCVD) poly(3,4 ethylenedioxythiophene) (PEDOT) has been demonstrated as an effective electrode for organic photovoltaics[22]. In a single step oCVD simultaneously achieves both the synthesis and conformal deposition of a conjugated polymeric thin film[23]. Because no spin coating is required, as with depositing poly(3,4-ethylenedioxythiophene) poly(styrenesulfonate) (PEDOT:PSS), it is expected that oCVD PEDOT would be able to conformally coat gratings and features over a wide range of geometric profiles.

In this paper we demonstrate how oxidative chemical vapor deposition (oCVD) can be used to create PEDOT electrodes on a variety of featured substrates. The conformal coverage and application to two main categories is discussed: texturing at single interfaces and three-dimensional non-planar cell architectures. PEDOT is able to conformally coat or fill in features sizes in the submicron range and is also compatible with fabricating larger macro-scale structures to create 3D architectures.

6.3 Materials and Methods

Square trench patterned silicon master slides were purchased from Lightsmyth with the following dimensions (corresponding to Figure 6-5b) pattern 1: g=50 nm, p=139 nm, w=69.5 nm; pattern 2: g=350 nm, p=700 nm, w=375 nm; pattern 3: g=200 nm, p=833.3 nm, w=416 nm. Corresponding to Figure 6-5c, nanocone (g=70-100 nm, p=100 nm) and nanowedge (g=70-100 nm, p=100 nm) master patterns were fabricated on silicon wafers at MIT Lincoln Labs. The patterns were created using interference lithography with a 157 nm source. An etch mask was patterned in hydrogen silsesquioxane (HSQ) and the difference in the lateral etch rate of the film to the vertical etch rate in silicon creates the tapered structures. Further details can be found in reference[24].

Prior to use, all silicon master substrates were cleaned for 5 minutes under oxygen plasma and then exposed to a fluorinating agent, tridecafluoro-1,1,2,2-tetrahydrooctyl) trichlorosilane under vacuum for 1 hour, to prevent the PMMA from sticking to the pattern after embossing.

For samples prepared for cross-sectional imaging, thin layers (~200-300 nm) of PMMA dissolved in anisole (Microchem, solids 4%) were spin coated onto silicon wafers before being imprinted. For samples prepared for optical measurements, bare PMMA (ePlastics, thickness 0.79 mm) substrates were imprinted. For samples in which the PEDOT layers themselves were imprinted, PEDOT was deposited directly onto silicon wafers.

Imprinting the PMMA and PEDOT layers was performed via hot embossing, as diagramed in Figure 6-5a, in a custom chamber designed at MIT Lincoln Labs. For PMMA samples, the imprinting was done at 125 °C and 260 psi for 2 minutes. PEDOT samples were imprinted at 160 °C and 260 psi for 10 minutes.

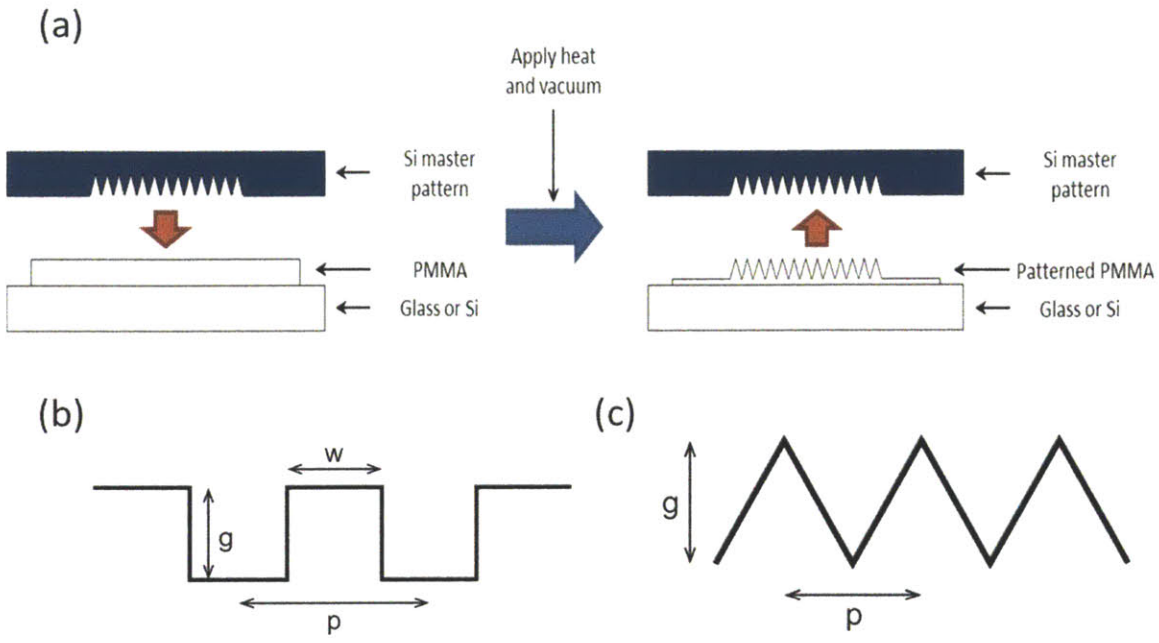

Figure 6-5: (a) Schematic of hot embossing processes to imprint PMMA (b) groove dimensions for square grating patterns (c) groove dimensions for nanowedge and nanocone patterns

The absorber material used for optical measurements, tetraphenyldibenzoperiflanthene (DBP) (Luminescencev Technology Corp., >99.5%), was used as purchased. DBP was deposited using a thermal evaporator at a pressure of ~1 x 10^{-6} at a rate of 0.2 Å/s. Film thicknesses were measured using a Woollam VASE ellipsometer and a Dektak profilometer. For textured profiles, film thicknesses were measured using SEM imaging. The ellipsometer was also used to measure optical constants *n* (complex refractive index) and *k* (extinction coefficient), which were used in the modeling section, (Supporting Information).

Films were imaged using a 6700 JEOL-JSM Field Emission Scanning Electron Microscope (FE-SEM). Substrates were prepared for cross-sectional imaging by first sputtering 5-10 nm of Au onto the surface then submerging them in liquid N_2 before being broken in half. Optical transmittance measurements were made using a Varian Cary 6000i UV-Vis-NIR dual-beam spectrophotometer.

The PEDOT films were formed by oxidative chemical vapor deposition (oCVD), described in more detail elsewhere[25]. Substrates were simultaneously exposed to vapors of 3,4-ethylenedioxythiophene (EDOT) monomer (Sigma Aldrich, 97%) and $FeCl_3$ oxidant (Sigma Aldrich, 99.99%) controllably evaporated from a resistively heated crucible. Process conditions were held the same across all depositions (chamber pressure ~0.1 mTorr, substrate temperature = 80 °C). The relatively low stage temperature was used so

as to not damage the PMMA imprinted patterns. The deposition length was varied to control film thickness. PEDOT:PSS (Sigma Aldrich, 1.1% in H_2O high conductivity grade) films were prepared by spin coating between 3,000-6,000 rpm for 60 seconds.

For the larger folded samples, polycarbonate sheets (0.127 mm thick) and copy paper (92 bright 20 lb) were used. The folding tests were performed by manually folding and creasing the samples and repeatedly measuring sheet resistance by probing the same locations across the fold line using a multimeter.

6.4 Results/Discussion

Texturing at a single interface

One way of enhancing light trapping in PV cells is to create texturing at a single interface. The result of texturing the front or top surface, where light enters the cell, is similar to anisotropic surface etching/roughening done on silicon solar cell surfaces to enhance light trapping[26]. Improvements can be achieved by either front-side texturing or backside texturing [27] as seen in Figure 6-6.

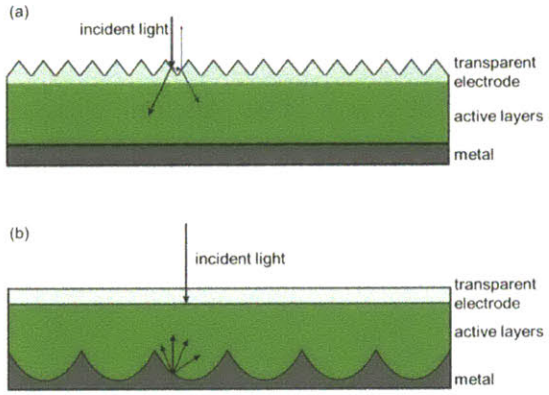

Figure 6-6: (a) Schematics of device architectures with texturing at (a) front and (b) back interfaces

Texturing of the substrate

One of the primary architectures explored in this work was pre-texturing of the substrate. Stand-alone PMMA substrates and thin sheets of PMMA spun cast onto silicon wafers were patterned by hot-embossing from a silicon master pattern. Subsequent layers were then deposited directly onto the textured PMMA substrates. One of the main advantages demonstrated here is the conformality of the oCVD PEDOT films onto the different textures. For cases where "filling in" the features is desired (Figure 6-7d), the oCVD PEDOT shows very close contact with the original texture pattern without gaps or other

defects, Figure 6-7b. Figure 6-7a shows a common problem with depositing solution-processed films onto textured substrates where there are gaps in the layer and the material does not conformally fill in the features.

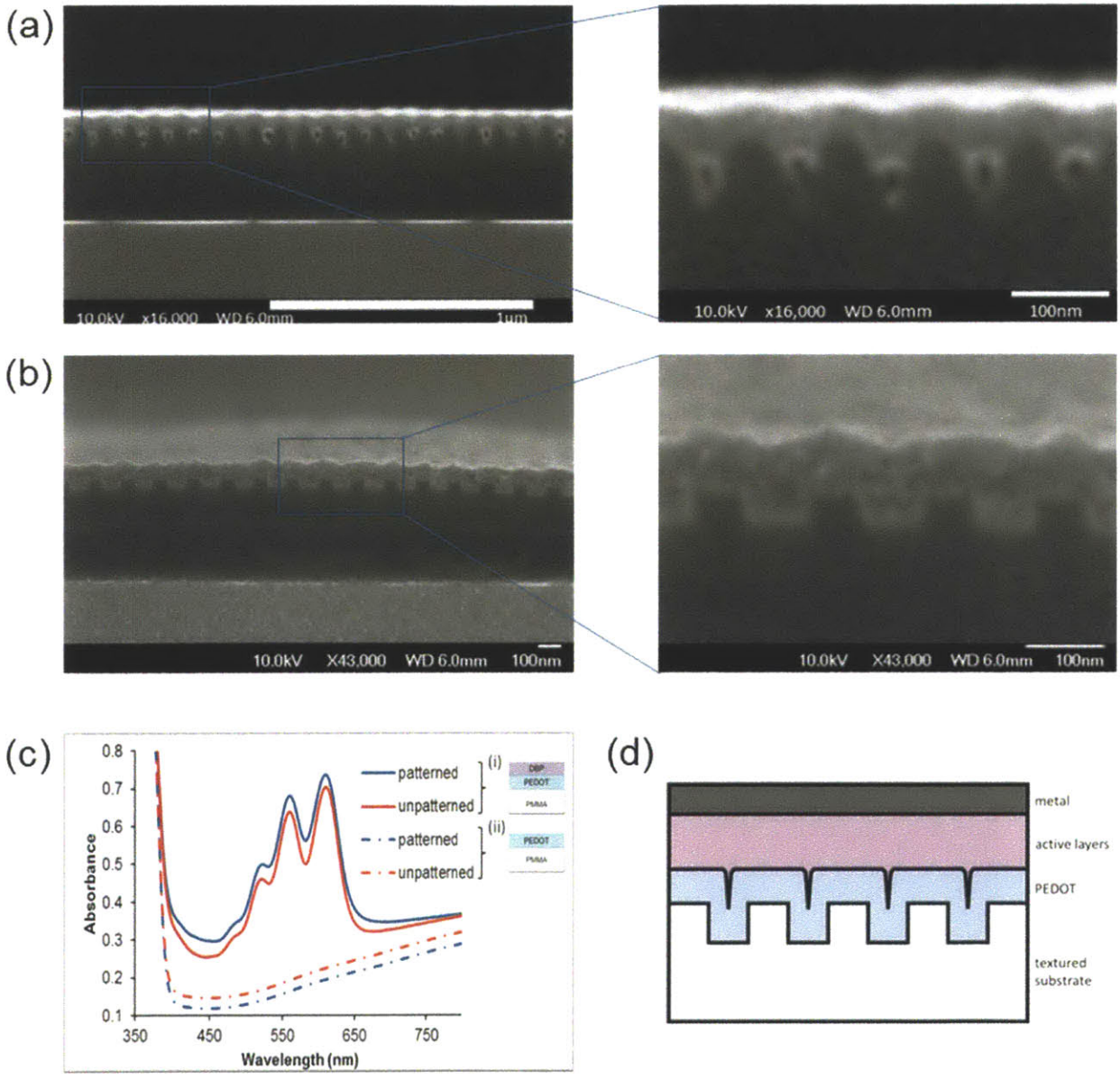

Figure 6-7: (a) PEDOT:PSS spin coated onto imprinted PMMA (nanowedge pattern). Inset shows pattern defects zoomed in. (b) oCVD PEDOT deposited on imprinted PMMA (square nanogrid pattern). Inset shows filling in of patterns zoomed in. (c) UV-Vis absorbance spectra for (i) DBP on PEDOT that has been deposited on both patterned (square grid) and unpatterned PMMA and (ii) a sample PEDOT layer on patterned and unpatterned PMM. (d) Schematic of device architecture with PEDOT deposited on pre-textured substrate

A thin layer of DBP (20 nm), a commonly used photovoltaic absorber material, was evaporated on top of the PEDOT for both textured and non-textured substrates. As seen in Figure 6-7c, there is an increase in

the absorbance of the active layer when the substrate is pre-textured. At the peaks at 560 nm and 610 nm there are 7% and 5% increases in the absorbance, respectively. It is expected that this value would increase even further by optimizing pattern geometry. The dashed lines show that this increase in absorbance is not due to more absorption in the PEDOT layer when deposited alone on the textured substrate.

In some cases, the electrode should not fill in the features but rather conformally coat the feature and create a texture on which to deposit the active layers. For smaller layer thicknesses we see that oCVD PEDOT does not have the issues with thinning at the tops of features and welling up at the bottoms of the features as is present with the spin-coated films. Figure 6-8 shows small < 100 nm feature nanowedge features and larger > 100 nm square grating features coated both by spin-coated PEDOT:PSS and oCVD PEDOT.

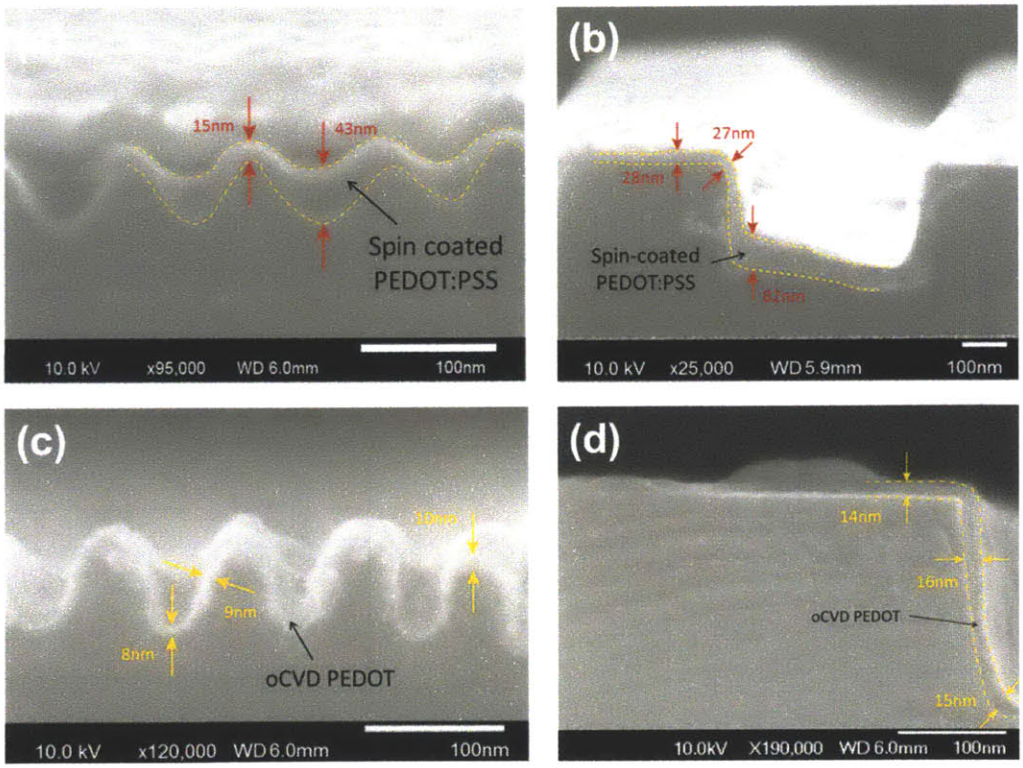

Figure 6-8: SEM images of (a) Spin-coated PEDOT:PSS on nanowedges textured PMMA (b) Spin-coated PEDOT:PSS on square trench textured PMMA (c) oCVD PEDOT on nanowedges textured PMMA (d) oCVD PEDOT on square trench textured PMMA. The sputtered gold layer is visible on the top surface of the images and may affect the appearance of the morphology . Dashed yellow lines have been added to (a), (b), and (d) to denote where the PEDOT:PSS and oCVD PEDOT layers are located. Arrows have been added to show film thickness at various locations.

For the nanowedge pattern with PEDOT:PSS spin-coated on top, Figure 6-8a, there is substantial welling up of the material at the bottoms of the features and thinning at the top. For the same pattern with

oCVD PEDOT, Figure 6-8b, we do not see a large variation in thickness when looking at the tops, bottoms, and side walls of the features. For the larger square features the same result is observed with the PEDOT:PSS having non-uniform coverage, Figure 6-8c, and the oCVD PEDOT layer providing conformal coverage, Figure 6-8d. Resistance measurements across the features did not indicate any noticeable decrease in oCVD PEDOT film conductivity (~800 S/cm) when patterned on planar vs. textured substrates.

Texturing the transparent electrode

An alternative to starting with a textured substrate is texturing the transparent electrode layer or hole-injection buffer layer itself before depositing the active layer materials, as diagramed in Figure 6-9a. This technique has been demonstrated using PEDOT:PSS by Yang et al., [28]in which dehydrated PEDOT:PSS, deposited on ITO, is imprinted using a silicon mold with < 100nm feature sizes. Larger, 600 nm, gratings were created in PEDOT:PSS using a PDMS mold by Chou et al. [29]Researchers have also demonstrated similar imprinting techniques to pattern the active layers before evaporating the back metal electrode[3, 30].

Figure 6-9b shows an oCVD PEDOT layer that was deposited on silicon and then imprinted using a square grating silicon master pattern with nano-scale feature sizes.

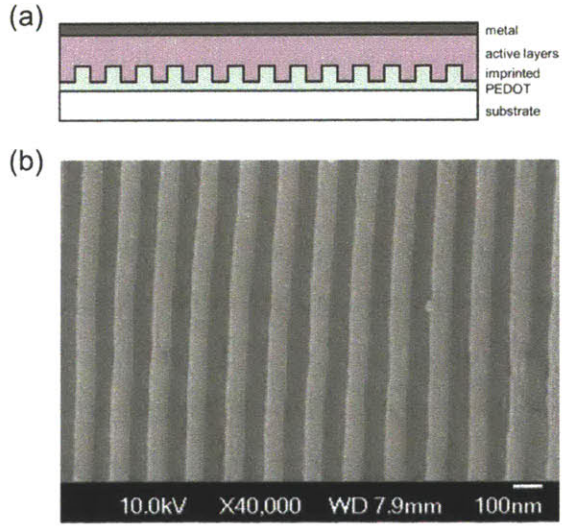

Figure 6-9: schematic of device architecture with imprinted PEDOT deposited on planar substrate (b) PEDOT layer (thickness = 94 nm) deposited on silicon and imprinted with small square grid pattern (groove depth 50 nm)

Simple texturing of the PEDOT electrode or buffer layer could be used to enhance both charge transport between the PEDOT and the active layers by creating a high surface area interface and light absorption by creating a non-planar framework on which to deposit the active layers. Being able to texture the PEDOT directly would also allow for these textured features to be created on substrates that are less easily patterned than PMMA, such as glass.

Texturing the back electrode

Texturing of the back electrode, which was not specifically explored in this work, can be accomplished by a variety of techniques including imprinting the top active layer before metal deposition or using lithography or other patterning techniques to create features or a mesh. Alternatively, the device could be fabricated with an inverted structure where the active layers were patterned onto a textured, reflective metal back electrode and a transparent electrode was deposited on top. oCVD PEDOT is well-suited to either of these configurations as it has been demonstrated in both conventional [22] and inverted, top-illuminated device structures[31].

Non-planar architecture

Another method to enhance light trapping is creating a non-planar architecture in which absorption is enhanced by light trapping due to reflective bouncing and/or decoupling of the optical and charge pathways. This type of technique has been demonstrated for inorganic devices by Zhu et al. [14]They showed enhanced photon management using nanowire and nanocone structures for anti-reflection and fabricated nanodome structured silicon devices with a 25% improvement in power conversion efficiency (PCE) over a planar device.

One example of this type of architecture for organic PVs has been modeled for both larger [10, 32] and subwavelength [5] sizes and experimentally demonstrated where light trapping is enhanced by creating a folded "v-shaped" architecture for conventional cells and a tandem cell [33] by using different active layer materials on either side of the "v" structure. Non-planar devices have also been demonstrated by depositing the electrode and active layer materials onto micron scale square [21] and triangular grid structures [4].

Macro-scale 3D device structures have been explored for inorganic devices as well. For example, Grossman et al. predicted that even simple 3D structures (cubes or towers with v-shaped patterns) could be used to substantially produce more energy than flat panels with the same area footprint [16, 34].

oCVD PEDOT is well-suited to use in non-planar structures. As seen in Figure 6-8d, as with the smaller < 100 nm feature sizes, the oCVD process provides a very conformal polymer layer over larger trenches. This electrode layer can either provide a base on which to build the rest of a non-planar device, as in Figure 6-10a, or could be deposited on top of an as-deposited non-planar half-cell, which would allow for the construction of devices on opaque non-planar substrates, as in Figure 6-10b.

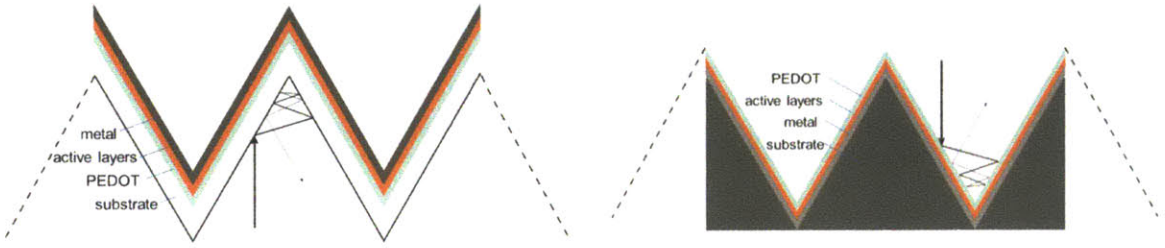

Figure 6-10: Schematics of device architectures with PEDOT deposited on non-planar substrates as (a) bottom electrode and (b) top electrode with optional opaque substrate.

The application of oCVD PEDOT to non-planar structures in the submicron and larger macro-scale size ranges is discussed in the following sections.

Submicron features

To demonstrate the enhanced absorption for non-planar vs. planar architectures, PMMA substrates were imprinted with a variety of patterns detailed in Table 6-1.

Table 6-1: Pattern dimensions

Pattern ID	Groove depth	Period/pitch	Line width	Description
G50	50 nm	139 nm	69.5 nm	square trenches
G200	200 nm	833.3 nm	416 nm	square trenches
G350	350 nm	700 nm	375 nm	square trenches
Nanowedges	70-100 nm	100 nm		triangular trenches
Nanocones	70-100 nm	100 nm		2D array of cones

A thin layer of PEDOT (15 nm) was then deposited on the substrates, followed by evaporation of a 20 nm DBP absorber layer. The absorbance was measured for the different patterns and compared with a planar substrate with the same layers.

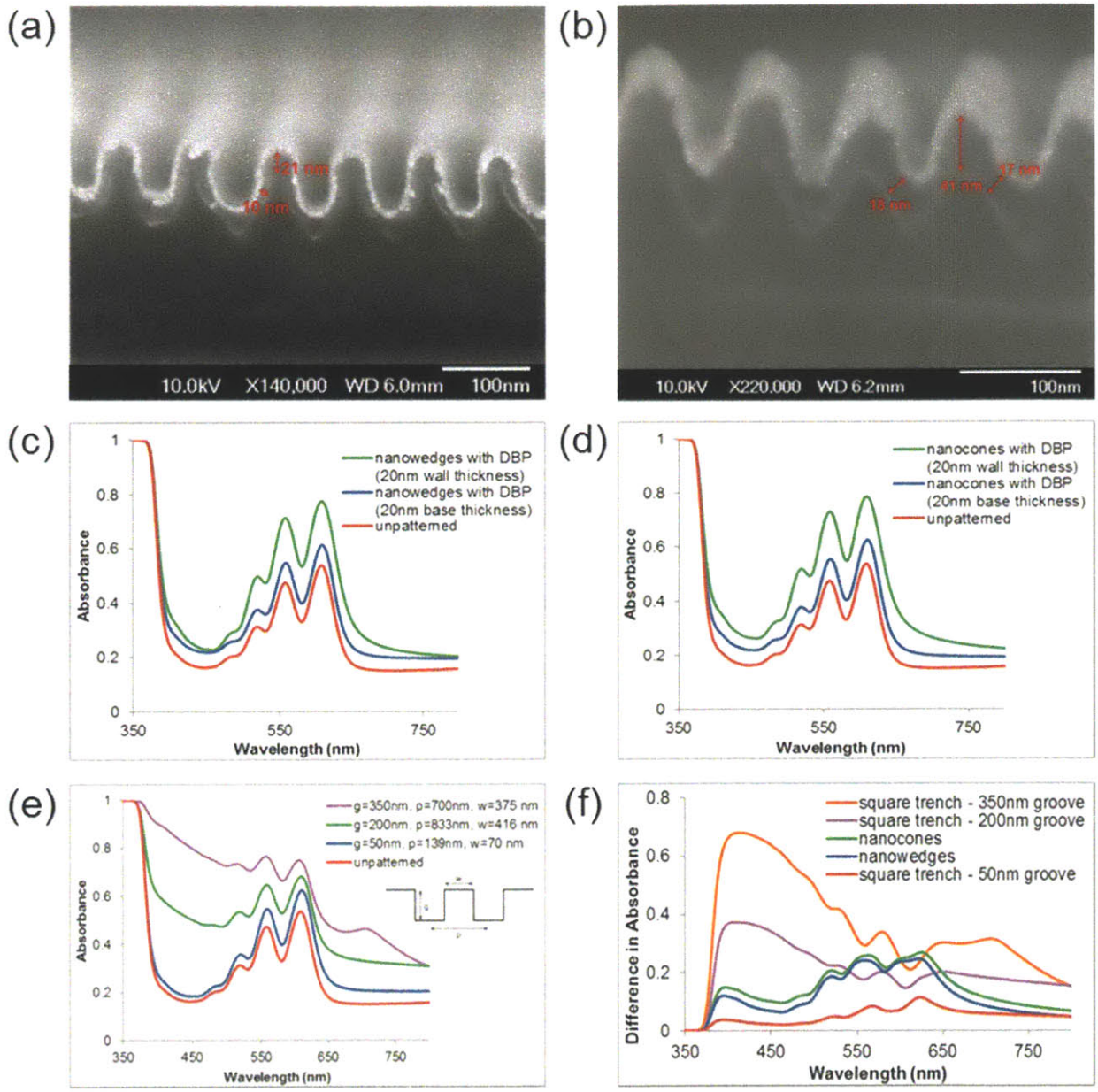

Figure 6-11: (a) SEM image of DBP (20nm) on nanowedges pattern (b) SEM image of DBP (40nm) on nanowedges pattern (c) absorbance of DBP (20nm base thickness and 20nm wall thickness) on nanowedges pattern vs. planar PMMA (d) absorbance of DBP (20nm base thickness and 20nm wall thickness) on nanocones pattern vs. planar PMMA (e) Absorbance of DBP (20nm) on PEDOT (15nm) on square trench imprinted PMMA vs. planar PMMA. The square trench dimensions, groove height, pattern width, and pitch, are detailed in the legend. (f) Difference in absorbance between patterned samples and unpatterned (nanowedges with DBP-20 nm wall thickness from graph [c], nanocones with DBP-20 nm wall thickness from graph [d], and all three square trench patterns from graph [e]). The planar sample absorbance was subtracted from the patterned sample absorbance to show the increase in absorbance as a function of wavelength.

For the smaller features, SEM images were taken to compare the thickness of the active layer in comparison to the measured thickness on planar substrates. Due to the directional nature of thermal evaporation, when evaporating 20 nm of DBP, only the top and bottoms of the features end up with a

20 nm layer thickness while the side wall coverage is approximately half as thick (~10 nm), Figure 6-11a. The same trend is seen for a 40 nm DBP layer where the base layer is 40 and the side walls are half as thick (~20 nm), Figure 6-11b. Some of these coverage issues could be overcome by tilting the stage during evaporation or evaporating small amounts at different angles to increase line of sight coverage. In Figure 6-11c the absorbance of DBP and PEDOT on a planar substrate is compared to DBP and PEDOT deposited on the nanowedges pattern both with a base 20 nm DBP layer (thinner side wall coverage) and with a thicker DBP layer that gives a 20 nm sidewall coverage. The same was done in Figure 6-11d for the nanocones pattern.

For all the samples there was an increase in the absorption even at a base of 20 nm DBP thickness and with the sidewalls having a <20 nm DBP thickness. With these dimensions applied to a photovoltaic cell, in comparison to a planar cell with a 20 nm active layer, the thinner sidewall thickness, would lead to less charge recombination. For the nanowedges pattern, the absorption peaks at 560 nm and 610 nm respectively increased by 16% and 14% for the 20nm base layer and by 51% and 45% for the 20nm side wall layer. For the nanocones pattern, the absorption peaks at 560 nm and 610 nm respectively increased by 17% and 17% for the 20nm base layer and by 55% and 47% for the 20nm side wall layer. In a full device, the absorption enhancement may improve even further with the inclusion of the reflective metal back electrode.

For the square trench patterns, a significant increase in absorption is seen in comparison to the unpatterned sample, Figure 6-11e. The absorption increases with increasing groove depth. In Figure 6-11f the difference in absorbance between the patterned and unpatterned samples has been plotted to show the increase in absorbance as a function of wavelength. For the patterns with the smallest features, the nanocones, nanowedges, and square trenches with a 50 nm groove depth, the absorbance increases the most for wavelengths where the DBP most strongly absorbs. This wavelength dependence suggests that for the smaller features, the absorption is enhanced primarily due to increasing the optical path length. For the larger square trench features, the absorption more significantly increases for wavelengths where DBP does not absorb as strongly. For the larger features, the absorption enhancement is due to a combination of increased optical path-length and reflective light bounces, with more light being trapped by the trenches with deeper grooves. The reflective light trapping is more beneficial at wavelengths where DBP does strongly absorb and thus results in a greater increase in measured absorbance.

Macro-scale 3D structures

oCVD can be used to fabricate PEDOT layers on larger macro-scale non-planar devices as well. Simple patterns can be created by folding thin plastic or textile materials such as polycarbonate or paper as seen in Figure 6-12b. The durability of oCVD PEDOT layers on bendable and foldable materials along with the ability to act as a functional electrode on such substrates has been previously demonstrated [22, 31]. Tests were completed on PEDOT deposited onto polycarbonate and paper substrates to determine conductivity loss upon folding, Figure 6-12. Two substrates (one paper and one plastic) were flat and unfolded before the deposition and then folded forward/inward after the PEDOT deposition (Figure 6-12i), two substrates were pre-folded prior to the PEDOT deposition and then re-folded after the deposition (Figure 6-12ii), and two substrates were unfolded before the deposition and then folded backward (Figure 6-12iii).

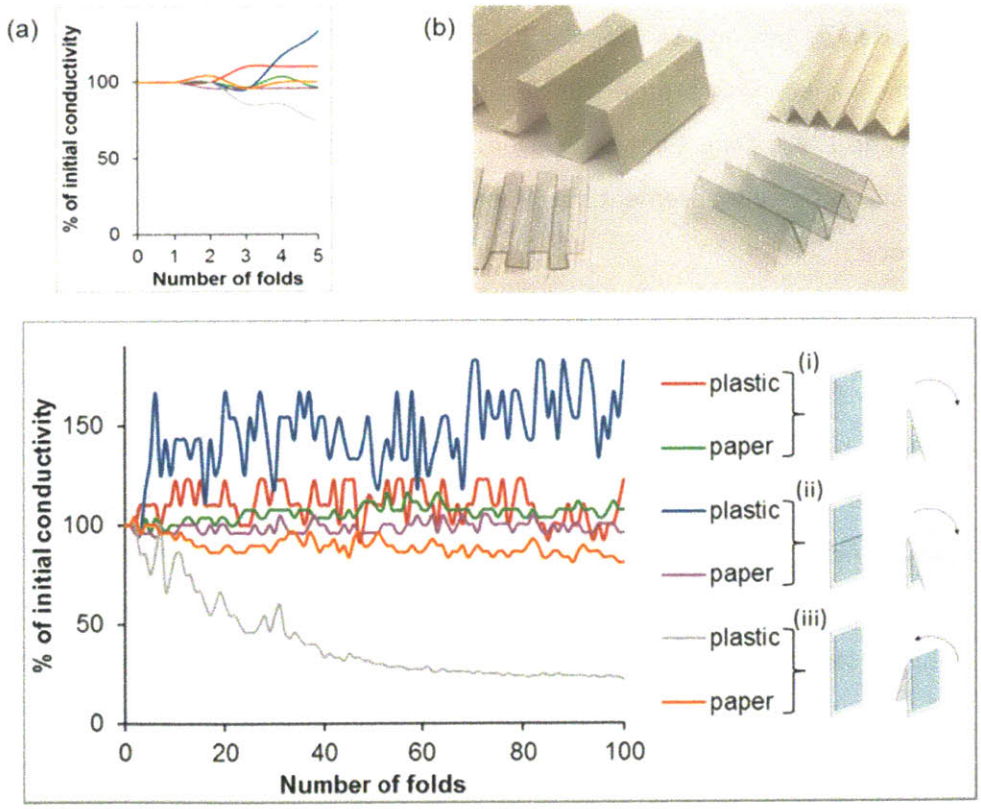

Figure 6-12: Change in conductivity of PEDOT layers on plastic and paper substrates after multiple folding cycles (i) regular folding, with PEDOT interior to fold, of initially flat substrate (ii) regular folding of PEDOT deposited on a pre-folded substrate (iii) back folding, with PEDOT exterior to fold, of initially flat substrate (a) inset shows values for first 5 folds (b) PEDOT deposited on folded polycarbonate and paper substrates

For all four regular folded samples (both flat and pre-folded), Figure 6-12i-ii, the conductivity did not decrease below 95% of the initial value even after 100 folding cycles. The back folded samples, Figure 6-12iii, exhibited a larger decrease in conductivity falling to 80% and 25% for the paper and plastic samples, respectively, though part of the decrease may have been due to the need to handle and crease the PEDOT deposited side. For all samples the PEDOT layers were found to retain their initial conductivity after one fold, Figure 6-12a. The ability to retain good electrical contact upon folding, on either initially flat or pre-folded substrates could have implications for future PV designs in which light trapping features are constructed through simple manipulation of the substrate structure.

Simple v-shaped structures (half-cells with a PEDOT layer and an absorber DBP layer) were fabricated and tested to show the increased absorption upon decreasing the folding angle for both a conventional structure (Figure 6-13b) where light shines first through the transparent substrate and an inverted top-illuminated structure where a transparent electrode is deposited on top of a cell stack (Figure 6-13a).

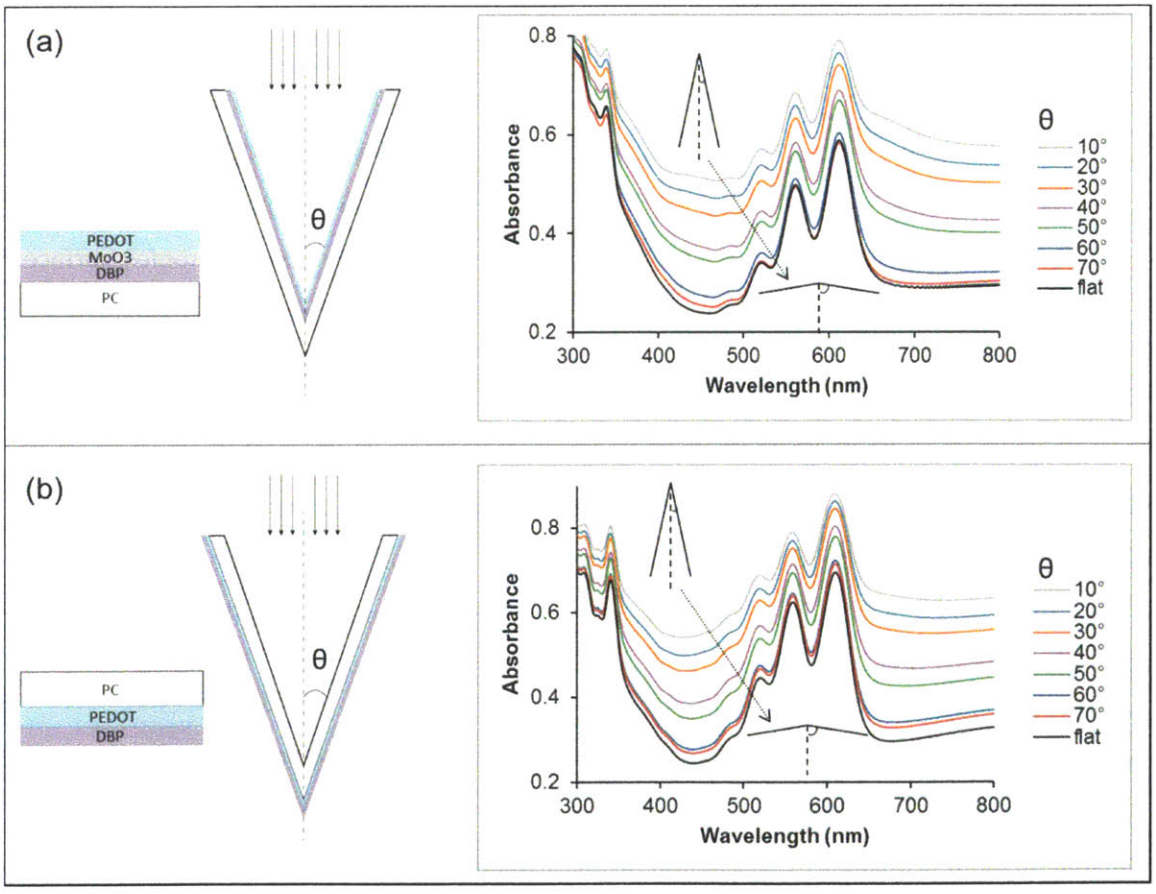

Figure 6-13: (a) Schematic of simple v-structure with inverted top-illuminated structure (MoO_3 [20nm] layer used to protect DBP [20nm] during PEDOT deposition) [31] and UV-Vis absorbance data at various folding angles θ. (b) Schematic of simple v-structure with conventional structure and UV-Vis absorbance data at various folding angles θ.

For both configurations, there is a significant increase in the amount of light absorbed going from unfolded (flat) to smaller folding angles. For example, for the conventional structure, the peaks at 560 nm and 610 nm increase by 14% and 14% for a 50° folding angle and 32% and 30% for a 20° folding angle, respectively. Andersson et al. investigated similar V-structures [10]. Using finite element modeling, they predicted significant increases in absorption are seen for folding angles < 60° due to the beginning of reflective bouncing (at 50° about 65% of the reflected light from one side hits the adjacent side). The same increase is seen for the structures created in this work in Figure 6-13. Another increase, also observed by Andersson et al., occurs and when the folding angle goes below 40°. In these folded configurations some light will be lost due to increased absorption in the PEDOT layer; however, with a full device stack there would be an added benefit of light reflecting off the back metal surface, which may then be absorbed in the active materials. A configuration such as this may lower the power output of individual cells due to partial shading but could produce a greater power output per a given area by absorbing and converting more of the incident light.

6.5 Conclusions

The oCVD process for depositing thin films of PEDOT was demonstrated for various light trapping photovoltaic architectures. For texturing at a single interface, it was shown that PEDOT is able to fully fill in features of varying shapes and feature sizes as low as 50 nm. For thinner layers, the PEDOT coatings were conformal and did not suffer the issues of thinning or blanketing across complex surfaces as is often seen with solution-processed films. Optical measurements showed that an active layer (DBP) coated onto PEDOT on a textured substrate exhibits higher absorbance than layers coated on fully planar devices.

Imprinting the PEDOT layer itself was accomplished by increasing the embossing time to 10 minutes. Imprinted PEDOT electrodes provide a textured framework on which active layers may be deposited to give a high surface area interface for charge transport and enable enhanced light trapping by creating a textured or non-planar device structure.

The application of oCVD PEDOT to non-planar and larger macro-scale features was also demonstrated. PEDOT is able to act as the transparent electrode in either conventional structures, where the electrode is deposited onto a transparent substrate, or in inverted, top-illuminated structures, where the transparent electrode is deposited onto a device stack with the option of using an opaque substrate. The oCVD PEDOT retains its conductivity upon folding on both paper and plastic substrates. Simple v-

shaped structures were created on plastic with PEDOT and DBP to show the absorbance enhancement at various folding angles.

As researchers look toward moving beyond traditional planar photovoltaic structures, vapor-based processes such as oCVD may play a vital role in ensuring good conformality and coverage of complex featured substrates.

6.6 Acknowledgements

This research is supported in part by Eni S.p.A. under the Eni-MIT Alliance Solar Frontiers Program and by the Department of Energy Office of Science Graduate Fellowship Program (DOE SCGF), made possible in part by the American Recovery and Reinvestment Act of 2009, administered by ORISE-ORAU under contract no. DE-AC05-06OR23100. We thank Dr. Theodore Bloomstein and his colleagues at MIT Lincoln Laboratory for their contributions of equipment, materials, and guidance for this work.

6.7 References

1. R. M. Howden, E. J. Flores, V. Bulovic and K. K. Gleason, *Submit to Organic Electronics*, 2013, **Manuscript**.
2. B. Kippelen and J. L. Bredas, *Energy & Environmental Science*, 2009, **2**, 251-261.
3. M. Niggemann, M. Glatthaar, A. Gombert, A. Hinsch and V. Wittwer, *Thin Solid Films*, 2004, **451-452**, 619-623.
4. M. Niggemann, M. Glatthaar, P. Lewer, C. Muller, J. Wagner and A. Gombert, *Thin Solid Films*, 2006, **511-512**, 628-633.
5. N. P. Sergeant, M. Agrawal and P. Peumans, *Optics Express*, 2010, **18**, 5525.
6. C.-C. Tsai, R. R. Grote, A. Banerjee, R. M. Osgood and D. Englund, *Optical Society of America*, 2012, **Submit 2012**.
7. H. Hoppe, N. Arnold, N. S. Sariciftci and D. Meissner, *Solar Energy Materials & Solar Cells*, 2003, **80**, 105-113.
8. G. F. Burkhard, E. T. Hoke and M. D. McGehee, *Advanced Materials*, 2010, **22**, 3293-3297.
9. H. Hoppe, N. Arnold, D. Meissner and N. S. Sariciftci, *Thin Solid Films*, 2004, **451-452**, 589-592.
10. V. Andersson, K. Tvingstedt and O. Inganas, *Journal of Applied Physics*, 2008, **103**, 094520.
11. K. S. Nalwa and S. Chaudhary, *Optics Express*, 2010, **18**, 5168.
12. M. Niggemann, M. Riede, A. Gombert and K. Leo, *Physica Status Solidi (a)*, 2008, **205**, 2862-1874.
13. C.-C. Chen, L. Dou, R. Zhu, C.-H. Chung, T.-B. Song, Y. B. Zheng, S. Hawks, G. Li, P. S. Weiss and Y. Yang, *ACS Nano*, 2012, **6**, 7185-7190.
14. J. Zhu, Z. Yu, S. Fan and Y. Cui, *Materials Science and Engineering R*, 2010, **70**, 330-340.
15. Y. Zhou, F. Zhang, K. Tvingstedt, W. Tian and O. Inganas, *Applied Physics Letters*, 2008, **93**, 033302.
16. M. Bernardi, N. Ferralis, J. H. Wan, R. Villalon and J. C. Grossman, *Energy & Environmental Science*, 2012, **5**, 6880.

17. H. Schift, C. David, M. Gabriel, J. Gobrecht, L. J. Heyderman, W. Kaiser, S. Köppel and L. Scandella, *Microelectronic Engineering*, 2000, **53**, 171-174.
18. M. Worgull, M. Heckele and W. K. Schomburg, *Microsyst Technol*, 2005, **12**, 110-115.
19. B. Zimmerman, M. Glatthaar, M. Niggemann, M. K. Riede, T. Ziegler and A. Gombert, *Proceedings of SPIE*, 2006, **6197**, 61970G-61971.
20. W. Bai, Q. Gan, G. Song, L. Chen, Z. Kafafi and F. Bartoli, *Optics Express*, 2010, **18**, A620.
21. K. S. Nalwa, J.-M. Park, K.-M. Ho and S. Chaudhary, *Advanced Materials*, 2011, **23**, 112-116.
22. M. C. Barr, J. A. Rowehl, R. R. Lunt, J. Xu, A. Wang, C. M. Boyce, S. G. Im, V. Bulovic and K. K. Gleason, *Advanced Materials*, 2011, **23**, 3500-3505.
23. D. Bhattacharyya, R. M. Howden, D. Borrelli and K. K. Gleason, *Journal of Polymer Science B: Polymer Physics*, 2012, **50**, 1329-1351.
24. T. M. Bloomstein, P. W. Juodawlkis, R. B. Swint, S. G. Cann, S. J. Deneault, N. N. Efremow Jr., D. E. Hardy, M. F. Marchant, A. Napoleone, D. C. Oakley and M. Rothschild, *Journal of Vacuum Science Technology B*, 2005, **23**, 2617-2623.
25. W. E. Tenhaeff and K. K. Gleason, *Advanced Functional Materials*, 2008, **18**, 979-992.
26. F. Leblanc, J. Perrin and J. Schmitt, *Journal of Applied Physics*, 1994, **75**, 1074.
27. L. Forbes, *Solar Energy*, 2012, **86**, 319-325.
28. Y. Yang, K. Lee, K. Mielczarek, W. Hu and A. Zakhidov, *Nanotechnology* 2011, **22**, 485301.
29. W.-Y. Chou, J. Chang, C.-T. Yen, F.-C. Tang, H.-L. Cheng, M.-H. Chang, S. L.-C. Hsu, J.-S. Chen and Y.-C. Lee, *Applied Physics Letters*, 2011, **99**, 183108.
30. S.-I. Na, S.-S. Kim, J. Jo, S.-H. Oh, J. Kim and D.-Y. Kim, *Advanced Functional Materials*, 2008, **18**, 3956-3963.
31. M. C. Barr, R. M. Howden, R. R. Lunt, V. Bulovic and K. K. Gleason, *Advanced Energy Materials*, 2012, **2**, 1404-1409.
32. S.-B. Rim, S. Zhao, S. R. Scully, M. D. McGehee and P. Peumans, *Applied Physics Letters*, 2007, **91**, 243501.
33. K. Tvingstedt, V. Andersson, F. Zhang and O. Inganas, *Applied Physics Letters*, 2007, **91**, 123514.
34. B. Myers, M. Bernardi and J. C. Grossman, *Applied Physics Letters*, 2010, **96**, 071902.

CHAPTER SEVEN

Conclusions

7.1 Conclusions

The first goal of the thesis project was to make improvements to the oCVD polymer films and optimize properties relevant to their application in organic photovoltaics. The design and construction of a new oCVD reactor and development of a new deposition procedure has allowed more control over the process conditions, resulting in more repeatable films. The acid rinsing study, detailed in Chapter 3, demonstrated a superior method for removing residual oxidant from the deposited films, significantly lowering sheet resistance and film roughness, and improving thermal stability. Lowering film sheet resistance without altering the absorption characteristics resulted in an improved tradeoff between charge collection and light transmission in PEDOT films, a significantly important factor for transparent conducting electrodes.

The next goal of the thesis work was to integrate the oCVD polymer films into photovoltaic devices and investigate compatibility with novel PV materials. oCVD PEDOT was first demonstrated as a replacement for the commonly used HTL spin coated PEDOT:PSS and then as a replacement for the ITO transparent electrode in the control device structure. The issues of spin-coated PEDOT:PSS on graphene's hydrophobic surface were overcome using vapor-deposited PEDOT HTLs, as discussed in Chapter 4. ITO-free devices with comparable performance to control structures were created using these graphene electrodes. Chapter 5 describes work done on top-illuminated inverted devices created by using oCVD to directly deposit PEDOT electrodes on the rest of a device stack. This work enabled the fabrication of devices on opaque substrates.

The use of oCVD PEDOT electrodes with textured and non-planar 3D organic photovoltaic (OPV) architectures was explored in Chapter 7. These light trapping structures have been demonstrated in the literature to significantly enhance light absorption and therefore power conversion efficiency in photovoltaics. oCVD PEDOT was shown to give much more conformal coverage than solution-processed layers and enhanced light absorption was demonstrated for a number of device geometries.

Significant improvements have been made to both the oCVD process itself and the final film quality. More conductive, stable films have been fabricated for application in optoelectronic devices. The efficiency of devices with polymer PEDOT electrodes has been vastly improved and the integration with various other materials and structures has led to creation of novel device architectures. These findings could have implications for further optimizing the PEDOT material and oCVD process, reaching even

higher efficiencies in OPV devices, and further expanding the application space over which OPV technologies may be deployed.

APPENDIX A

Polymer-free near-infrared photovoltaics with single chirality (6,5) semiconducting carbon nanotube active layers

The work described in this chapter has been published in *Advanced Materials*[1]

A.1 Introduction

The addition of single-walled carbon nanototubes (SWNTs) into next generation solar cells as near infrared absorbers has shown the potential to efficiently harness energy in the 1000nm to 1400nm range.[2-4] However, these and other SWNT enabled PVs have required the use of a polymer wrapping agents[2-5] or photoactive layer.[6-8] While such layers are suspected to increase device performance at the laboratory scale, the use of PV engineered polymers is oftentimes limiting due to their inherently low photostability and the necessity of highly controlled environments for assembly and characterization.[9] In contrast, carbon nanotubes have the strong advantage of being extremely stable in air while at the same time absorbing the near infrared region of the solar spectrum.[10] Here, for the first time, we demonstrate a polymer free carbon based photovoltaic which relies on exciton dissociation at the SWNT/C_{60} interface. Through the construction of a carbon based photovoltaic completely free of polymeric active or transport layers, we show both the feasibility of this novel device as well as inform the mechanisms for inefficiencies in SWNT and carbon based solar cells.

A.2 Experimental

Single chirality (6,5) semiconducting SWNTs were isolated using multiple iterations of a modified procedure demonstrated by Liu et al.[11] which advanced considerably the pioneering observations from Kappes.[12] Following the isolation of sufficient (6,5) SWNT solution, films were constructed using a vacuum filtration technique[13] and deposited onto either a transparent or patterned-In:SnO_2 (ITO) substrate for optical and photovoltaic characterization, respectively. The C60 (Sigma Aldrich, 99.9%), and the top Ag cathode (Sigma) were thermally evaporated using shadow masking at a base pressure of $1 \times 10\text{-}6$ Torr at rates of 1.0 Å/s for the organic materials and 2 Å/s for Ag. The C60 was purified via thermal gradient sublimation before use. Ag was used as received. Pre-patterned ITO substrates (Thin Film Devices, 20 Ω/sq) were cleaned by subsequent sonication in DI water with detergent, DI water, acetone, and isopropyl alcohol, followed by 30 seconds of O2 plasma cleaning. The device structure was confirmed via cross-sectional SEM. The cross section was created by mechanically cleaving the device such that all 4 layers were visible. A JOEL 6700 SEM was used, set at 1kV with a working distance of 2.9mm and using the secondary electron imaging (SEI) detector. The image, Figure A-1, clearly shows the 4 layers that are used in the device. However, we note that the SWNT layer seems to have slightly collapsed and sheared such that the interface is no longer sharp. SWNT have a strong binding force with adjacent SWNT and this is a possible explanation for the bundled shearing that appears to have occurred during cleaving.

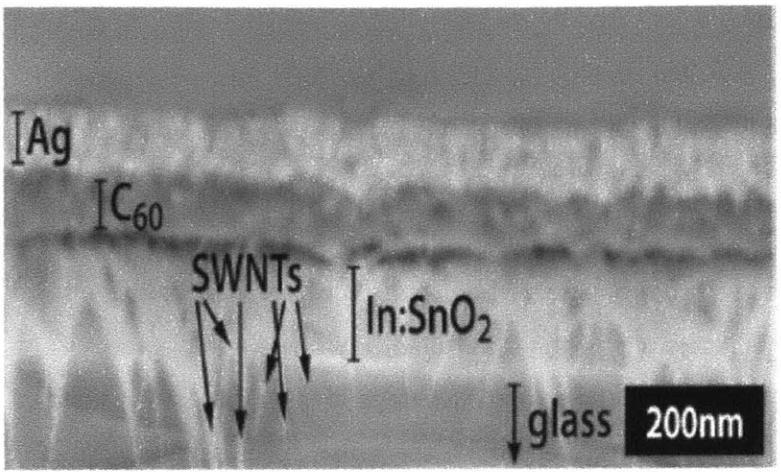

Figure A-1: Cross-sectional scanning electron microscope (SEM) image showing the four distinct layers in the planar heterojunction device. Arrows drawn from SWNTs intended as guide to the eye for SWNTs hanging from the cleaved interface. Note that because of the cleaving method utilized and the inter-woven nature of the SWNT layer, assignment of SWNT layer thickness via cross-sectional SEM is not accurate due to hanging SWNTs draped over its cross section. Accurate SWNT film thickness was determined via surface profilometry of isolated SWNT films, as described in the main text.

Current-voltage measurements were recorded by a Keithley 6487 picoammeter in nitrogen atmosphere. Devices were tested using 100 mW/cm2 illumination provided by a 150 W xenon arc-lamp (Newport 96000) filtered to AM 1.5G. The EQE spectrum was collected using a home built setup. The light sources that were used were a Xenon arc lamp for the visible to the beginning of the near IR and a Quartz tungsten halogen lamp for the majority of the near infrared, both supplied by Newport. The light source is sent through a monochromator and the source is chopped. The monochromatic light is then swept through the wavelength range of interest and read out through a lock-in amplifier in order ensure that low levels of signal can be read. The EQE spectrum was found to overlap exactly for the part of the spectrum read by both detection mechanisms from 900 to 1100nm. The testing facility is kept under a nitrogen atmosphere in a glove box in order to keep out any contamination similar to that performed by P.R. Brown et. al.[14]

A.3 Results and Discussion

To study the case of an all carbon nanotube phase, we designed and constructed a device whereby electrons and holes are conducted through SWNT and C_{60} layers, respectively, and excitons are dissociated at the interface between the two, Figure A-2. Further, device assembly using only highly purified single chirality (6,5) SWNTs[11, 15, 16] allows for the distinction between intrinsic losses and those caused by impurities in SWNT chirality that have dominated many systems reported in the literature.

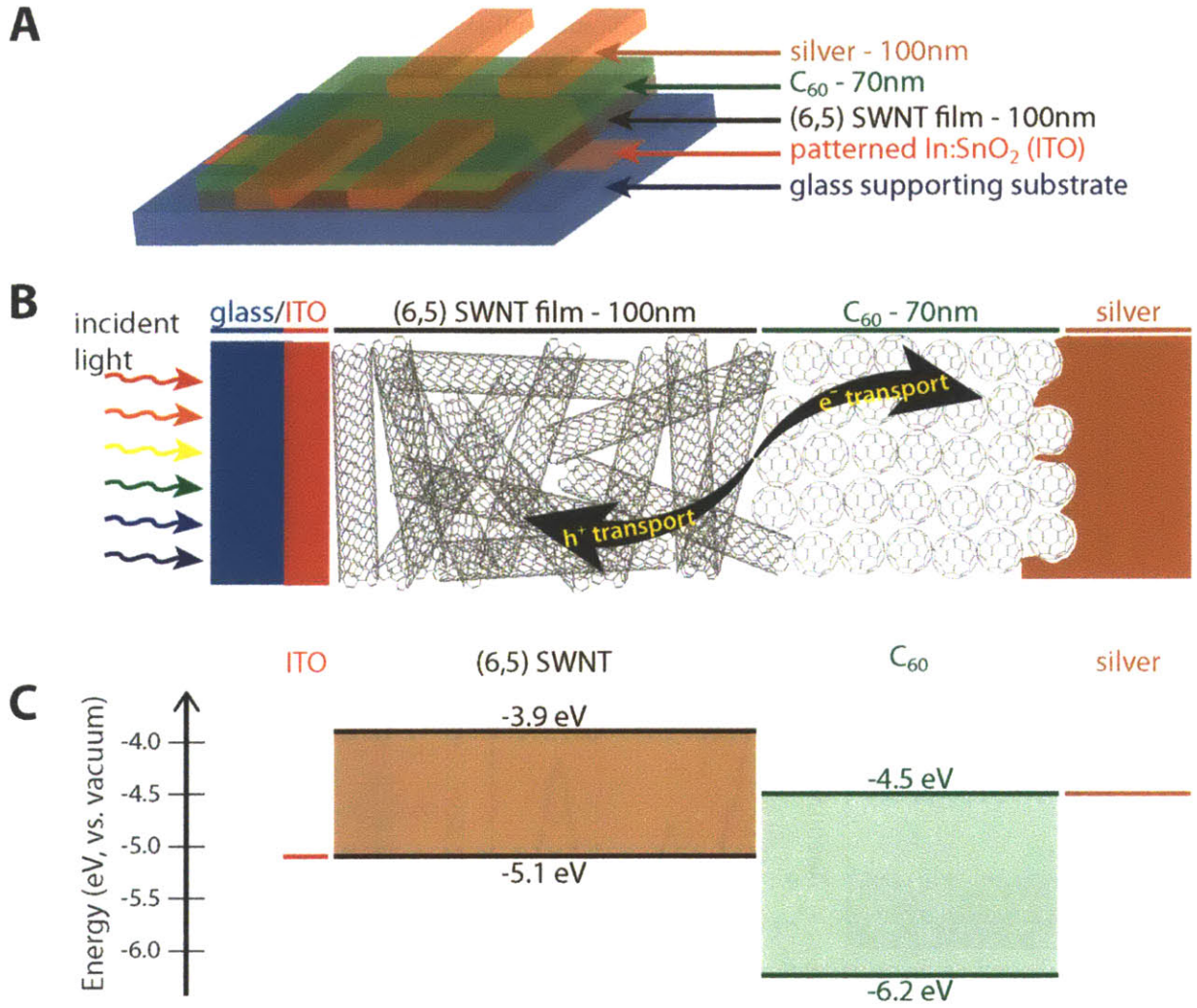

Figure A-2: Schematic and energy diagram of polymer-free carbon nanotube photovoltaic device. Layered three-dimensional device architecture (A) which allows for the fabrication and analysis of multiple devices from a single SWNT film, and cross-sectional diagram (B) emphasizing the directional transport of charge carriers. Energy diagram (C) of device, illustrating a type-II heterojunction. Absolute energy levels of (6,5) SWNTs taken from reference [16].

Building an all-carbon photovoltaic first necessitated the isolation of a relatively large quantity of single-chirality SWNTs, from which bulk SWNT films could be constructed. Resultant films showed coloration from the SWNTs, but were sufficiently transparent to allow for transmission based optical characterization, Figure A-3D. Both absorbance (Figure A-3E) and 2D emission (Figure A-3F) spectroscopic peaks observed in the (6,5) SWNT film are red-shifted and broadened with respect to the (6,5) SWNT nanotube solution—absorption and emission from 977nm to 1030nm and 982nm to 1063nm, respectively. We assign this shift and broadening to the increased dielectric screening present in SWNTs surrounded by other nanotubes, as opposed to surfactant and solvent molecules.[17] The photoluminescence from the film further demonstrates the high purity of the SWNT matrix with respect

to the (6,5) chirality. Specifically, only the (6,5) chirality emission peak is present—Figure A-3C,F. Given that exciton energy transfer (EET), has been shown to be highly efficient in both large[18] and small[19] bundles of SC-SWNTs, we exclude, for the first time, the potential of inhomogeneity in SWNT chirality from the list of possible inefficiencies in a SWNT based photovoltaic device.

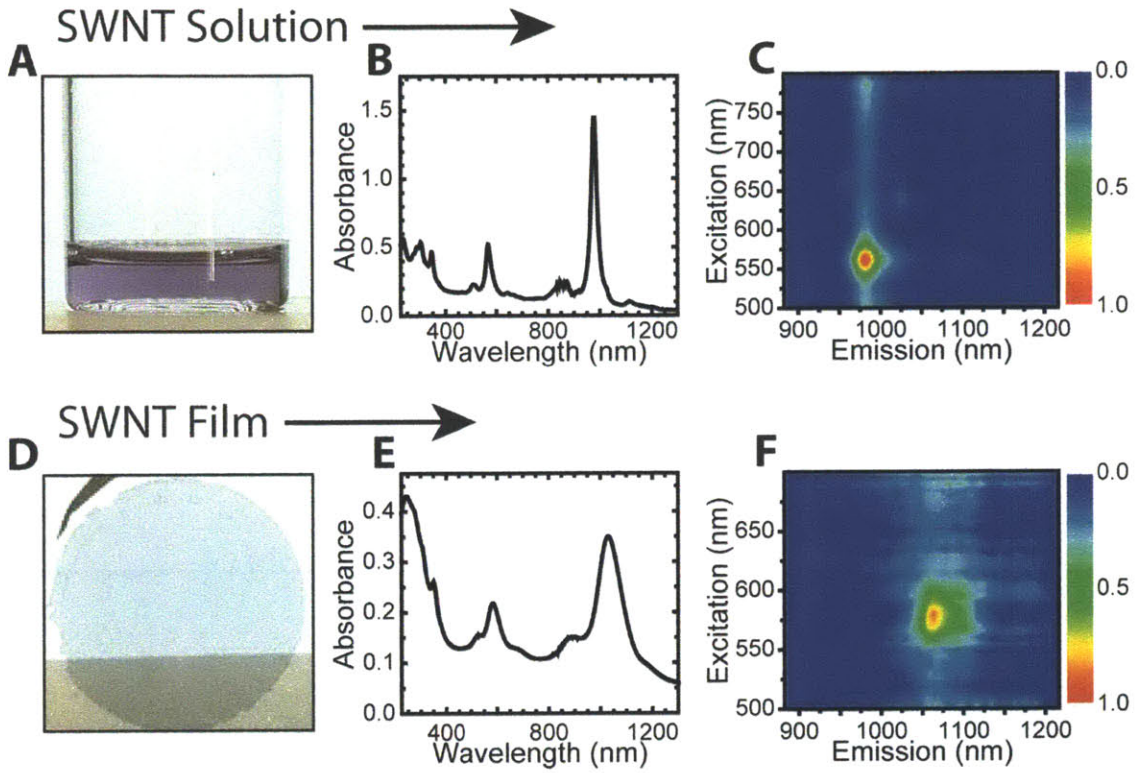

Figure A-3: Characterization of liquid and fi lm single chirality (6,5) SWNT samples. Photographs (A, D), absorbance traces (B, D), and 2D emission spectrographs (C, F) of both SWNTs suspended in 2% SDS solution (A, B, C) and formed into a 100 nm thick fi lm (D, E, F). The strong absorption and emission peaks are indicative of a single-chirality SWNT sample.

The single chirality nature of the SWNT films demonstrated here exceed those produced with SWNT obtained from density gradient ultracentrifugation. Because of this, exciton diffusion in a highly pure single chirality film has yet to be characterized, and will be the subject of future studies.

To further isolate the effects of non-SWNT materials in device performance, we washed each film with copious amounts of deionized water to remove surfactant. EDX analysis was performed on both a film prepared for device construction as well as one dropcast directly from 2% SDS solution. While dropcast films showed the presence of Na^+, this ion was absent in the washed films, suggesting that all surfactant was removed from the device prepared SWNT layers.

Devices were constructed by depositing highly pure surfactant free (6,5) SWNT films atop an ITO/glass support in a planar heterojunction geometry as the p-type material, while a thermally evaporated 70nm thick of C_{60} served as the n-type material. The back electrode was formed by thermal deposition of silver, completing the photovoltaic device, Figure A-2A.

Electrons and holes are collected at the C_{60}/silver and SWNT/ITO interfaces, respectively, Figure A-2B. Energetically, the choice of (6,5) SWNTs and C_{60} forms a type II heterojunction device,[20] Figure A-2C. Here, we explicitly chose to forego the use of an electron or hole blocking layer—one or both of which have become common in the fabrication of organic planar heterojunction devices[9]—with the goal of gaining insight into the performance and limitations of an all carbon active and transport layer. We plan to explore the implementation of these layers in future studies, with the ultimate goal of maximizing device efficiency.

Performance of 7 identically fabricated devices was measured under 100mW/cm^2 AM1.5 illumination, and average parameters of V_{oc}=0.32±0.025V, J_{sc}=0.76±0.045mA/cm^2, FF=0.32±0.029, and η=0.79±0.15% were calculated. The best device performed at V_{oc}=0.33V, J_{sc}=0.81mA/cm^2, FF=0.37, and η=0.10%, Figure A-4A. The measured overall efficiencies of 0.10% are comparable to polymer based photovoltaics where SWNT were added to increase active layer conductivity.[21-23] To ensure that the SWNTs were contributing to the observed photocurrent, an external quantum efficiency (EQE) spectrum was acquired using calibrated monochromatic excitation from 300 to 1100nm, Figure A-4B. We note that a large part of the photocurrent is contributed by the C_{60} layer, as evidenced by the EQE peaks in the 300-600nm region, a phenomenon which could partially be due to the creation of a Schottky barrier at the C_{60}/Ag interface.[24] Importantly, a peak is present in the near infrared which directly corresponds with the absorbance of the (6,5) SWNT film, Figure A-4B, inset. This is the first demonstration of photocurrent response from a SWNT film made of a single SWNT chirality.

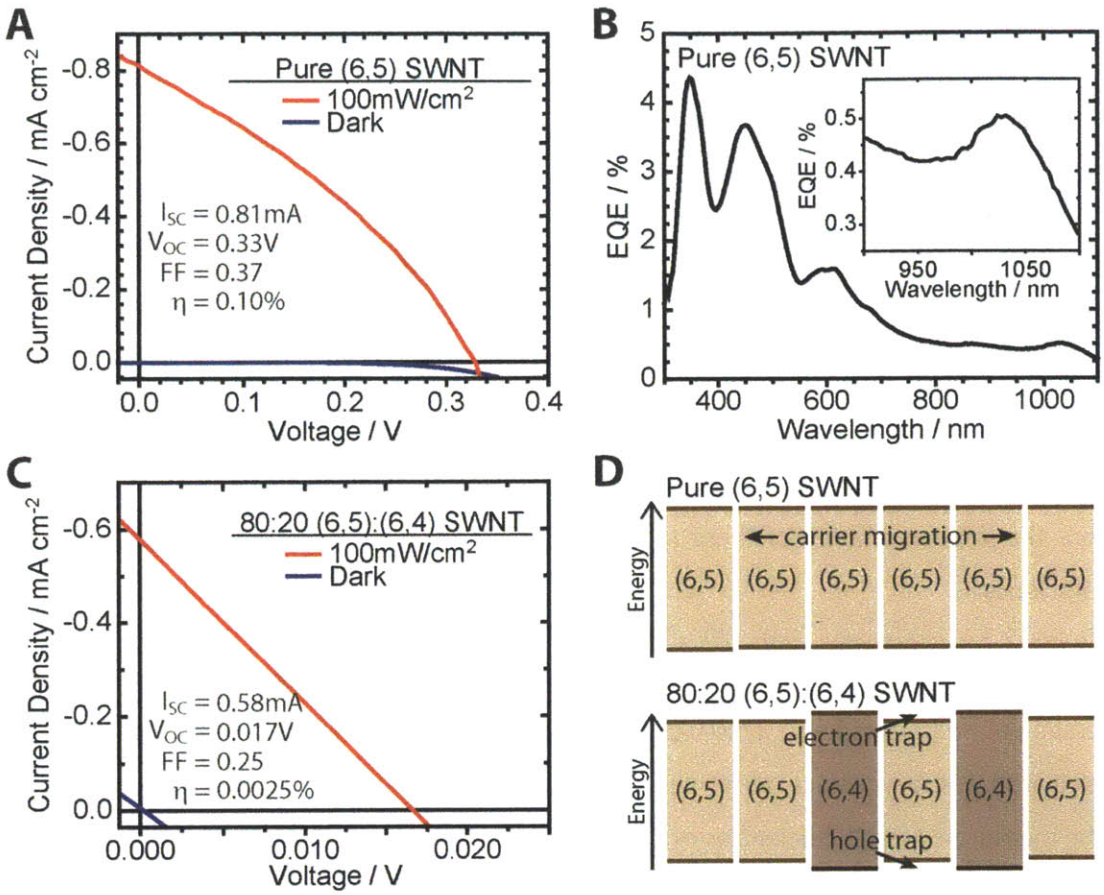

Figure A-4: Photovoltaic characterization of polymer-free carbon nanotube solar cell. IV (A) and EQE (B) of pure (6,5) SWNT-C¬60 device. Inset in (B) emphasizes region corresponding to E 11 transition in (6,5) SWNTs. IV characterization of 80:20 (6,5):(6,4) SC-SWNT by weight (C), and schematic representation of the recombination centers introduced when a semiconducting nanotube fi lm is constructed with multiple chiralities, (D). IV curves shown both under AM1.5 illumination (red) and in the dark (blue).

In order to comment on the importance of monodispersity in SWNT chirality, we constructed control devices from a film made with 80:20 (6,5):(6,4) SC-SWNT by weight. Interestingly, these devices showed extremely poor performance in V_{oc}, I_{sc}, and fill factor, Figure A-4C. Power conversion efficiency was reduced in this device by over 30 times relative to the device constructed with a pure (6:5) film. This discrepancy can be explained by the lack of a well-defined uniform bandgap within the SWNT film and at the SWNT/C_{60} interface. Because of the presence of (6,4) SWNTs, electron and hole traps are formed within the carbon nanotube film, serving as centers for exciton recombination, Figure A-4D.

This report of a polymer free carbon nanotube based solar cell represents an important step forward in the evolution of carbon based photovoltaics. In his pioneering work, Arnold et. al. demonstrated the first SWNT based photovoltaic using a matrix comprised of polymer, C_{60}, and unpurified HiPco SWNT.[4]

According to Arnold, to fully exploit the potential of SWNTs in photodetectors, the SWNT must be isolated from each other and paired with semiconductor layers that have the appropriate energetics for efficiently dissociating SWNT excitons.[4] Here, we demonstrate that this condition is not necessary to extract photocurrent from SWNT based photovoltaics, but rather, polymer free devices can be realized if the photoactive SWNT layer is comprised of a single SWNT chirality.

In terms of device efficiency, those reported here still fall behind what has been previously reported using SWNT/polymer matricies. For example, the observed EQE peak efficiency at the nanotube E_{11} transition, 0.5%, is lower than other studies which employ SWNTs as the absorbing layer,[2, 5] However, this is the first demonstration of photocurrent obtained from a completely polymer free SWNT-C_{60} device, and we expect improvement with future device optimization. Below, we discuss the performance of our device in the terms of commonly studied efficiency limiting mechanisms.

A possible reason for sub-optimal device performance is the use of a SWNT layer that is significantly thicker than the estimated bulk SWNT exciton diffusion length. Many studies have reported the exciton diffusion length within single nanotubes as hundreds of nm.[25, 26] However, fewer studies have investigated the exciton diffusion length through collections of contacting nanotubes. Bindl et al.[5] reported an approximate diffusion length of 2 nm within a nanotube fi lm, however, this value was determined with the presence of a polymeric wrapping around the nanotubes. Through a reduction of polymeric wrapping, Bindl et al. report an increase in diffusion length, therefore, we predict further increase in diffusion length in the limit of a polymer free SWNT fi lm. However, exciton diffusion lengths have never been directly measured in single-chirality films of this purity, making it difficult to approximate the exact value. Elucidation of exciton diffusion lengths in pure SWNT films will be the subject of future work.

We expect the exciton diffusion through the film will largely be governed by exciton hopping mechanisms and EET. To date, evidence for band-like continuum behavior, as has been seen in quantum dot superlattices,[27] has not been realized in SWNT films. However, there is recent evidence to suggest the possibility of excitonic tunneling in nanotube bundles.[28] The exact mechanisms, rate, and diffusion lengths of excitons in these films will be the subject for future studies.

A.4 Conclusions

In conclusion, an all carbon photovoltaic device has been demonstrated where a film of highly purified (6,5) carbon nanotubes acts as the active photoabsorption layer. There is evidence to suggest that the tight control over the electronic structure of the SWNTs has enabled a V_{OC} higher than previously demonstrated in other devices. While the device efficiency is low, it is interesting to note that it is comparable to many polymer-SWNT bulk heterojunction devices, and that this tight control over electronic type also shows evidence for an increased diffusion length through the film. Only a 20% impurity by weight of a second chirality of semiconducting SWNT (6,4) results in a more than 30 times decrease in power conversion efficiency. This work provides a foundation for future work aimed at increasing the efficiency of polymer-free all-carbon photovoltaics via several mechanisms, including active layer thickness modulation, bulk heterojunction geometries and SWNT alignment.

A.5 Acknowledgements

This work was supported by Eni, S.p.A (Italy) through the MIT Energy Initiative Program. R.M.J. gratefully acknowledges support from the National Science Foundation Graduate Research Fellowship and the Department of Defense through the National Defense Science and Engineering Graduate Fellowship. This research was also supported in part (authors R.H. and A.J.H.) by the Department of Energy Office of Science Graduate Fellowship Program (DOE SCGF), made possible in part by the American Recovery and Reinvestment Act of 2009, administered by ORISE-ORAU under contract no. DE-AC05-06OR23100. The authors would also like to thank Prof. Vladimir Bulovic for the use of his fabrication facilities.

A.6 References

1. R. M. Jain, R. Howden, K. Tvrdy, S. Shimizu, A. J. Hilmer, T. P. McNicholas, K. K. Gleason and M. S. Strano, *Advanced Materials*, 2012, **24**, 4436-4439.
2. D. J. Bindl, A. S. Brewer and M. S. Arnold, *Nano Research*, 2011, **4**, 1174-1179.
3. D. J. Bindl, N. S. Safron and M. S. Arnold, *ACS Nano*, 2010, **4**.
4. M. S. Arnold, J. D. Zimmerman, C. K. Renshaw, X. Xu, R. R. Lunt, C. M. Austin and S. R. Forrest, *Nano Letters*, 2009, **9**, 3354-3358.
5. D. J. Bindl, M. Y. Wu, F. C. Prehn and M. S. Arnold, *Nano Letters*, 2011, **11**, 455-460.
6. Y. Kanai and J. C. Grossman, *Nano Letters*, 2008, **8**, 908-912.
7. M. H. Ham, G. L. C. Paulus, C. Y. Lee, C. Song, K. Kalantar-zadeh, W. Choi, J. H. Han and M. S. Strano, *ACS Nano*, 2010, **4**, 6251-6259.
8. S. Ren, M. Bernardi, R. R. Lunt, V. Bulovic, J. C. Grossman and S. G. Gradecak, *Nano Letters*, 2011, **11**, 5313-5321.

9. B. Kippelen and J. L. Bredas, *Energy & Environmental Science*, 2009, **2**, 251-261.
10. P. Avouris, M. Freitag and V. Perebeinos, *Nature Photonics*, 2008, **2**.
11. H. P. Liu, D. Nishide, T. Tanaka and H. Kataura, *Nature Communications*, 2011, **2**.
12. K. Moshammer, F. Hennrich and M. M. Kappes, *Nano Research*, 2009, **2**, 599-606.
13. L. Hu, D. S. Hecht and G. Grüner, *Nano Lett.*, 2004, **4**, 2513-2517.
14. P. R. Brown, R. R. Lunt, N. Zhao, T. P. Osedach, D. D. Wanger, L. Y. Chang, M. G. Bawendi and V. Bulovic, *Nano Letters*, 2011, **11**, 2955-2961.
15. M. S. Arnold, A. A. Green, J. F. Hulvat, S. I. Stupp and M. C. Hersam, *Nature Nanotechnology*, 2006, **1**, 60-65.
16. S. Ghosh, S. M. Bachilo and R. B. Weisman, *Nature Nanotechnology*, 2010, **5**.
17. F. Wang, M. Y. Sfeir, L. M. Huang, X. M. H. Huang, Y. Wu, J. H. Kim, J. Hone, S. O'Brien, L. E. Brus and T. F. Heinz, *Physical Review Letters*, 2006, **96**, 167401.
18. J. H. Han, G. L. C. Paulus, R. Maruyama, D. A. Heller, W. J. Kim, P. W. Barone, C. Y. Lee, J. H. Choi, M. H. Ham, C. Song, C. Fantini and M. S. Strano, *Nature Materials*, 2010, **9**, 833-839.
19. P. H. Tan, A. G. Rozhin, T. Hasan, P. Hu, V. Scardaci, W. I. Milne and A. C. Ferrari, *Physical Review Letters*, 2007, **99**, 137402.
20. V. Barone, J. E. Peralta, J. Uddin and G. E. Scuseria, *Journal of Chemical Physics*, 2006, 124.
21. E. Kymakis, I. Alexandrou and G. A. J. Amaratunga, *Journal of Applied Physics*, 2003, **93**, 1764-1768.
22. E. Kymakis and G. A. J. Amaratunga, *Reviews on Advanced Materials Science*, 2005, **10**, 300-305.
23. J. X. Geng and T. Y. Zeng, *Journal of the American Chemical Society*, 2006, **128**, 16827-16833.
24. M. Koltun, D. Faiman, S. Goren, E. A. Katz, E. Kunoff, A. Shames, S. Shtutina and B. Uzan, *Solar Energy Materials & Solar Cells*, 1996, **44**, 485-491.
25. S. Moritsubo, T. Murai, T. Shimada, Y. Murakami, S. Chiashi, S. Murayama and Y. K. Kato, *Physical Review Letters*, 2010, **104**, 247402.
26. L. Luer, S. Hoseinkhani, D. Polli, J. Crochet, T. Hertel and G. Lanzani, *Nature Physics*, 2009, **5**, 54-58.
27. E. Talgorn, Y. Gao, M. Aerts, L. T. Kunneman, J. M. Schins, T. J. Savenije, A. J. Houtepen and D. A. Siebbeles, *Nature Nanotechnology*, 2011, **6**, 733-739.
28. J. J. Crochet, J. D. Sau, J. G. Duque, S. K. Doorn and M. L. Cohen, *ACS Nano*, 2011, **5**.

APPENDIX B

Oxidative chemical vapor deposition (oCVD) chamber drawings and accessories list

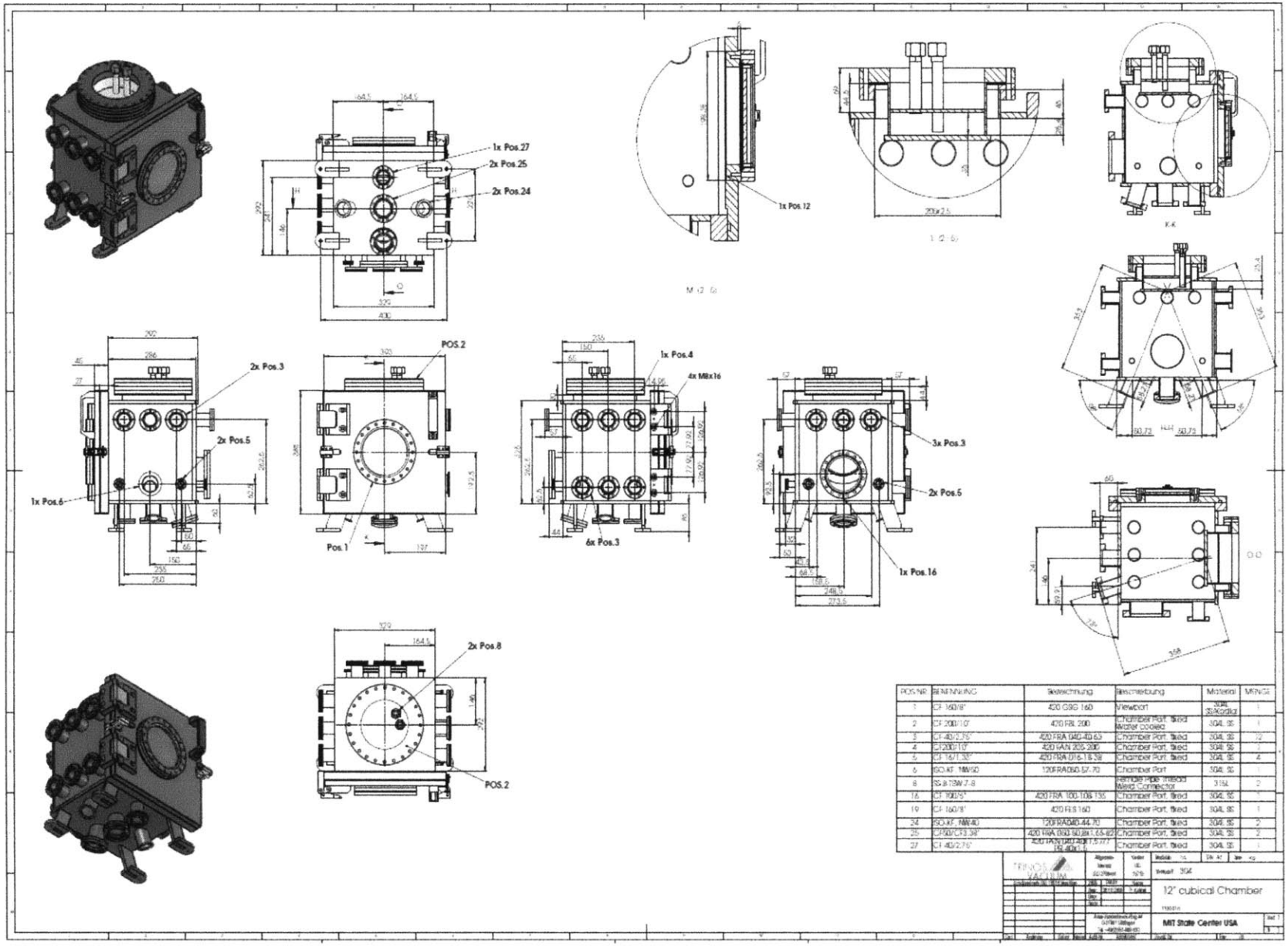

POS.NR	BENENNUNG	Teilezeichnung	Beschreibung	Material	MENGE
1	CF 160/8"	420 ISRS 160	Viewport	304L SSAgGdId	1
2	CF 200/10"	420 FBL 200	Chamber Port, Tread Welded Cooled	304L SS	1
3	CF 40/2.75"	420 FRA 040-40.63	Chamber Port, Tread	304L SS	12
4	CF200/10"	420 FAN 200-200	Chamber Port, Tread	304L SS	1
5	CF 16/1.38"	420 FRA 016-16.38	Chamber Port, Tread	304L SS	4
6	ISO-KF NW40	120FRA050.57.70	Chamber Port	304L SS	1
8	RS-8-TSW-7-8		Hermale Pipe Thread Weld Connector	316L	2
16	CF 100/5"	420 FRA 100.108.135	Chamber Port, Tread	304L SS	1
19	CF 160/8"	420 FES 160	Chamber Port, fixed	304L SS	1
24	ISO-KF NW40	120FRA040-44.70	Chamber Port, Tread	304L SS	2
25	CF50/CF3.38"	420 FRA 050.50.84.1.65-62	Chamber Port, Tread	304L SS	2
27	CF 40/2.75"	420 FAN 040-40.1.5-117	Chamber Port, Tread	304L SS	1

Figure B-1: Full engineering drawings for oCVD reactor

Table B-1: Legend for Figure B-1 engineering drawings

POS-NR.	BENENNUNG	Bezeichnung	Beschreibung	Material	MENGE
1	CF 160/8"	420 GSG 160	Viewport	304L SS/Kodial	1
2	CF 200/10"	420 FBL 200	Chamber Port, fixed Water cooled	304L SS	1
3	CF 40/2.75"	420 FRA 040-40-63	Chamber Port, fixed	304L SS	12
4	CF200/10"	420 FAN 205-200	Chamber Port, fixed	304L SS	1
5	CF 16/1,33"	420 FRA 016-18-38	Chamber Port, fixed	304L SS	4
6	ISO-KF, NW50	120FRA050-57-70	Chamber Port	304L SS	1
8	SS-8-TSW-7-8		Female Pipe Thread Weld Connector	315L	2
16	CF 100/6"	420 FRA 100-108-135	Chamber Port, fixed	304L SS	1
19	CF 160/8"	420 FES 160	Chamber Port, fixed	304L SS	1
24	ISO-KF, NW40	120FRA040-44-70	Chamber Port, fixed	304L SS	2
25	CF50/CF3.38"	420 FRA 050-50,8x1,65-82	Chamber Port, fixed	304L SS	2
27	CF 40/2.75"	420 FAN 040-40x1,5 /// PR-40x1,5	Chamber Port, fixed	304L SS	1

TRINOS VACUUM

Schutzvermerk ISO 16015 beachten

Allgemeintoleranz ISO 2768-mK | Kanten ISO 13715 | Maßstab 1:5 | DIN A1 | Gew. kg

Werkstoff: 304

	2009	Datum	Name
Bear.		28.10.2009	P. Kunkel
Gepr.			
Norm			

12" cubical Chamber

P09415

Anna-Vandenhoeck-Ring 44
D-37081 Gottingen
Tel. +49(0)551-999 630

MIT State Center USA

Blatt 1 Bl.

Zust.	Änderung	Datum	Name	Auftr.-Nr.	AB09004B7	Ersatz für		Rev.	09

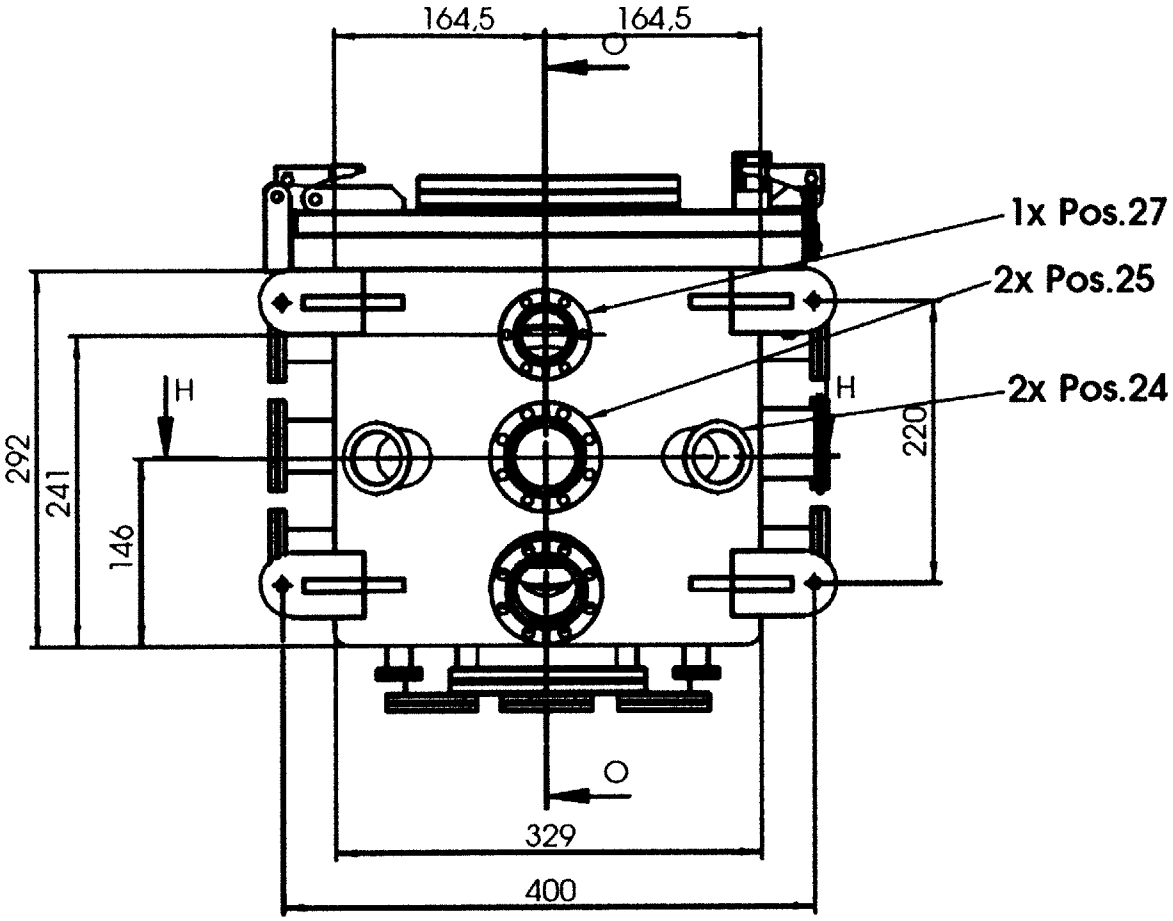

Figure B-2: oCVD chamber engineering drawings – close-up of bottom of chamber

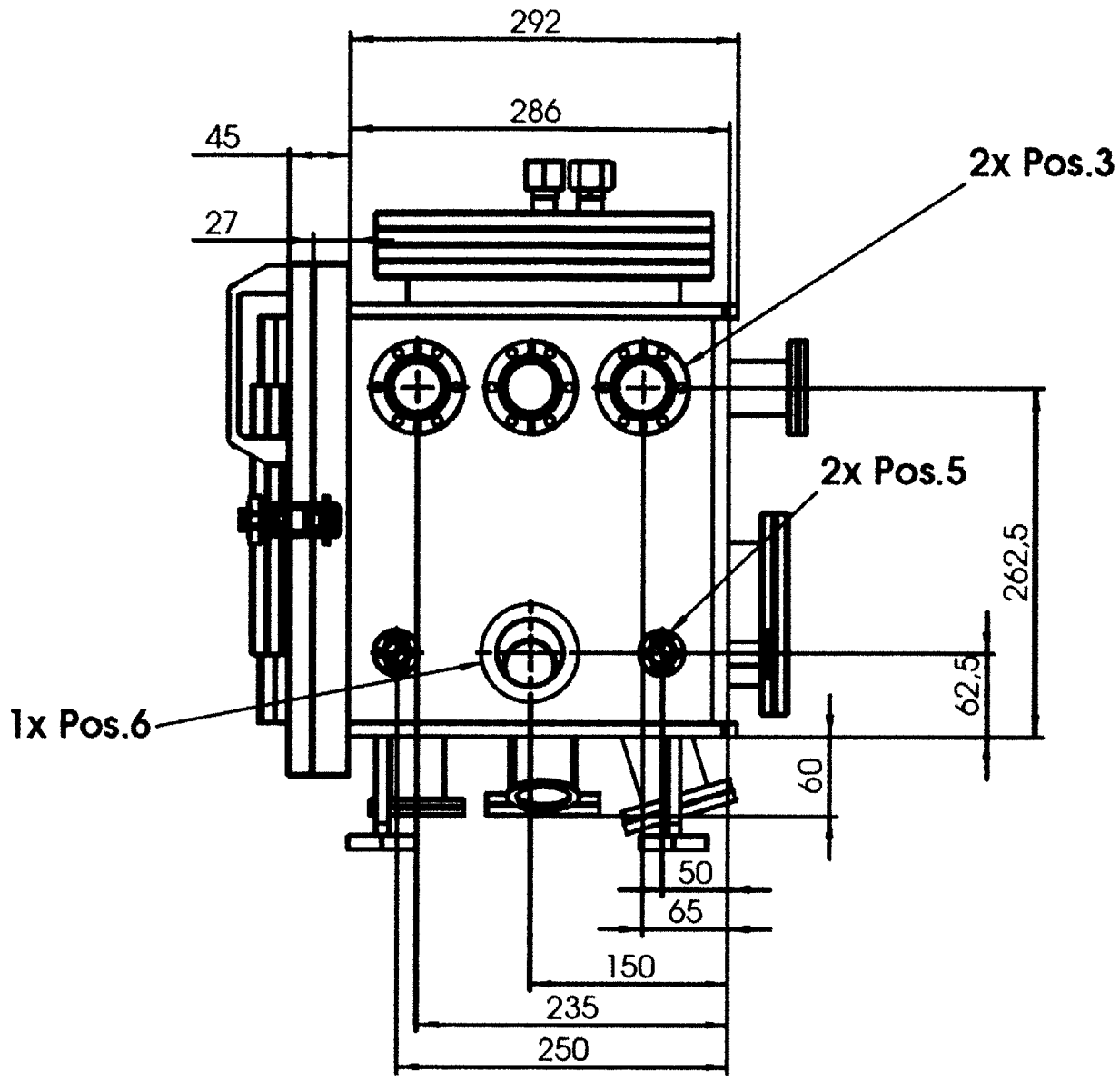

Figure B-3: oCVD chamber engineering drawings – close-up of right side of chamber

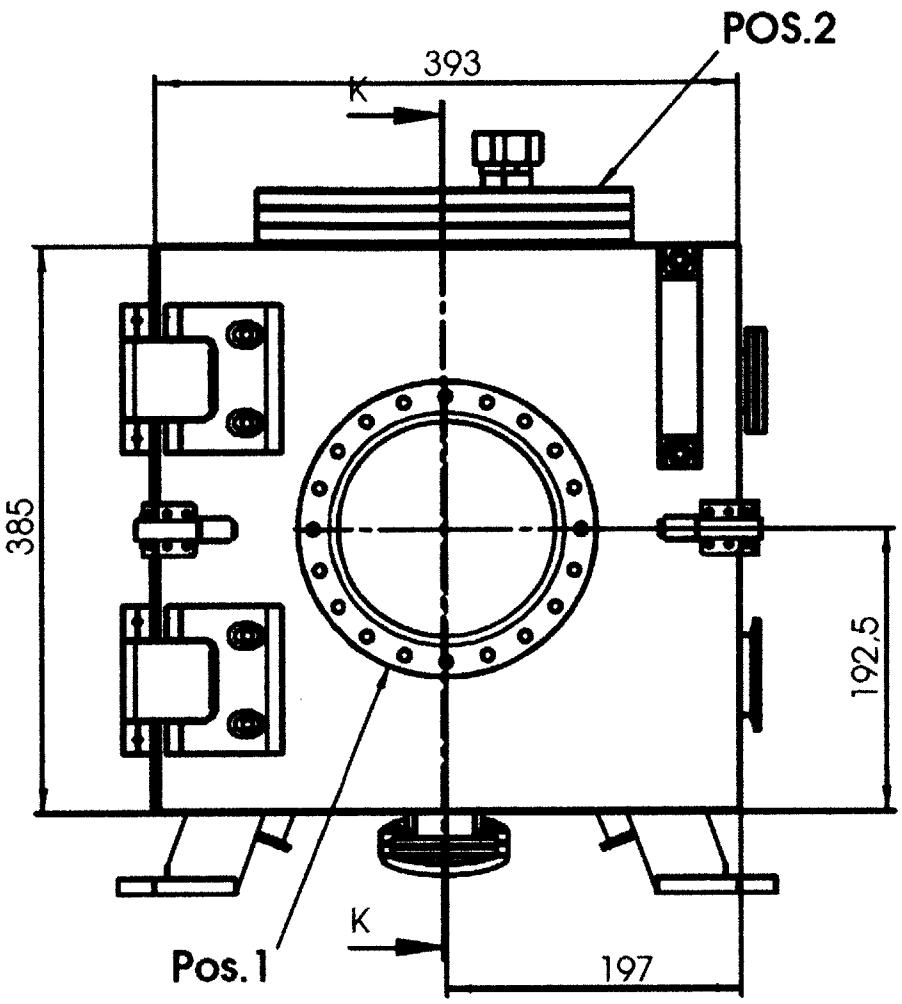

Figure B-4: oCVD chamber engineering drawings – close-up view of door and chamber front side

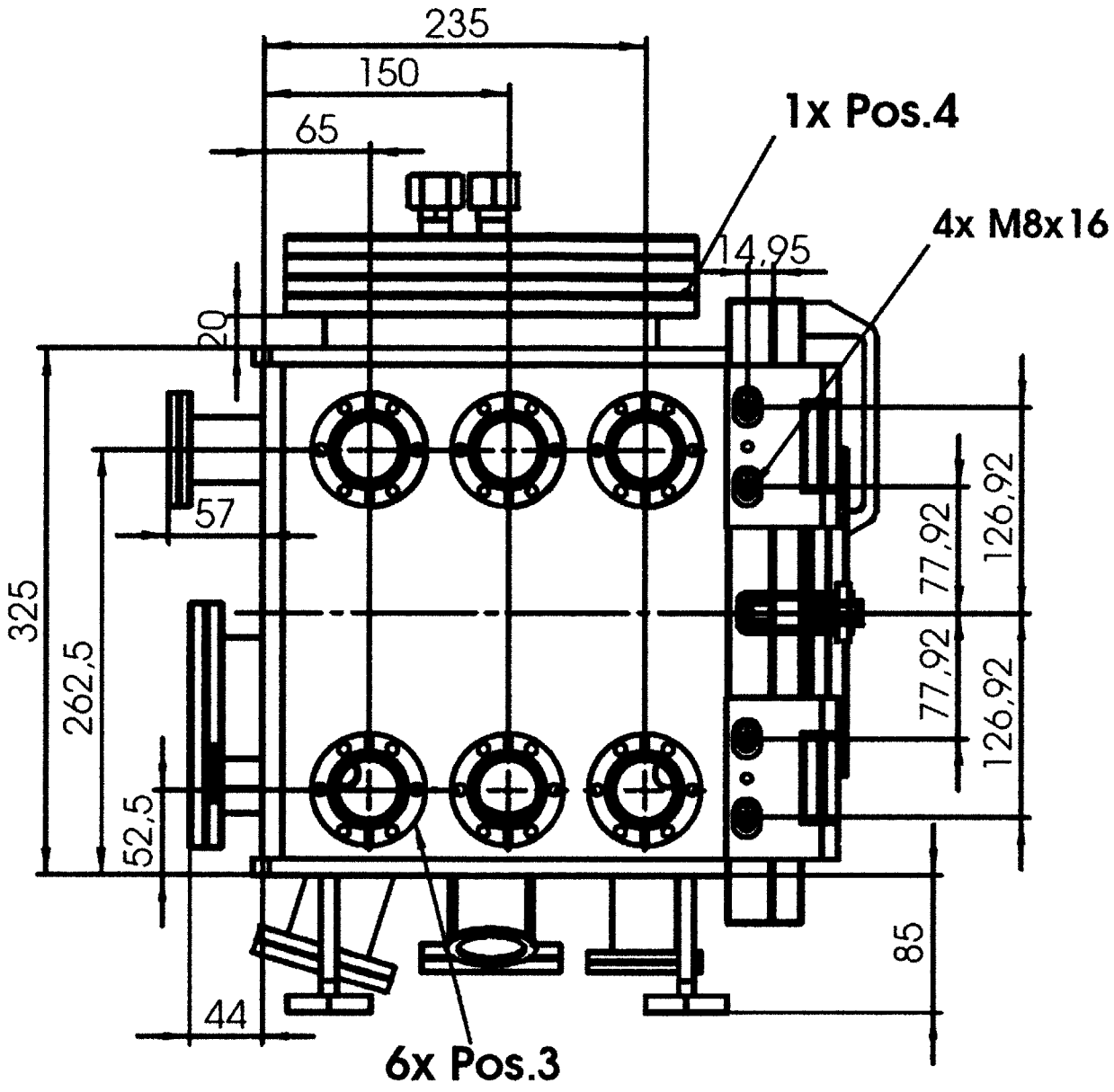

Figure B-5: oCVD chamber engineering drawings – close-up view of left side of chamber

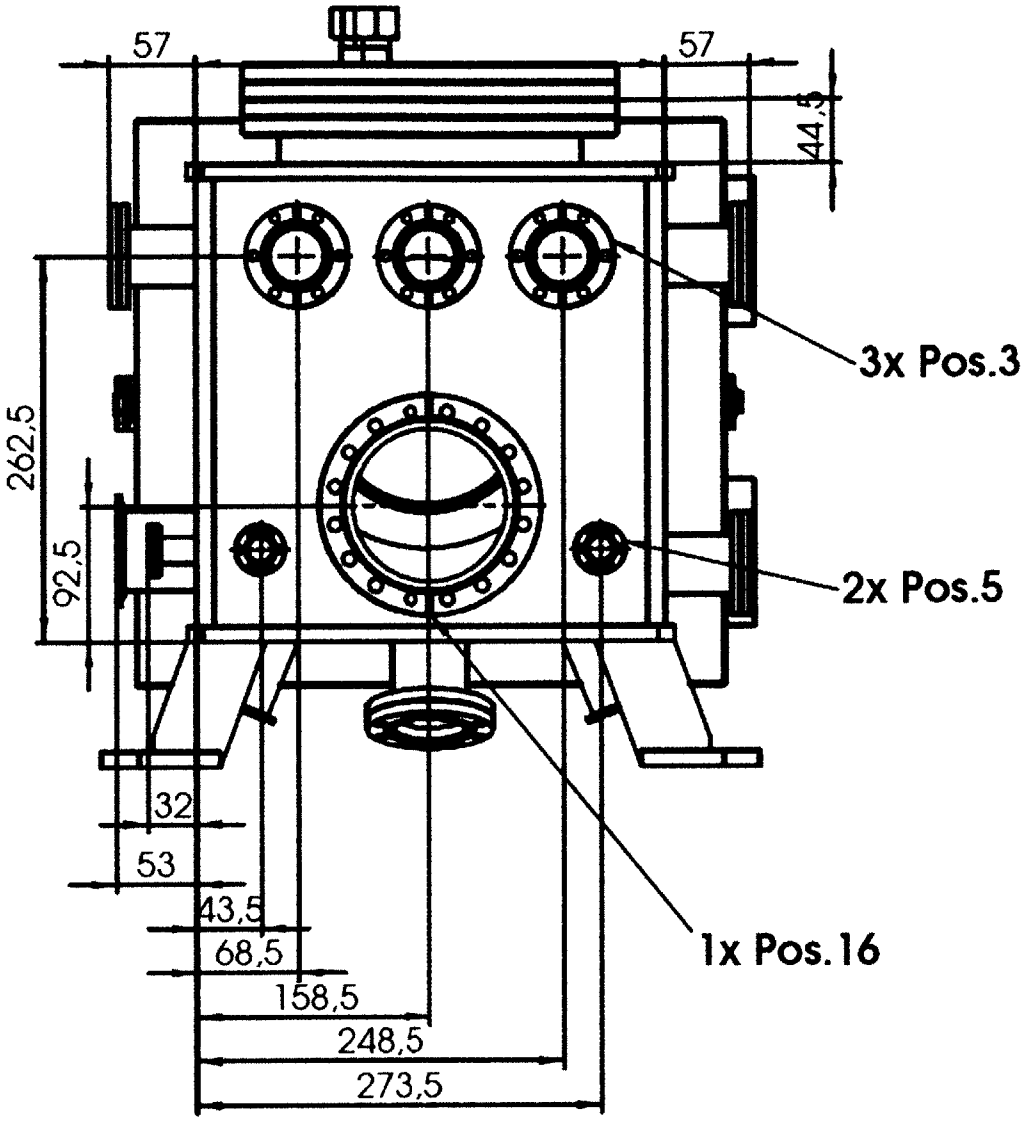

Figure B-6: oCVD chamber engineering drawings – close-up view of back side of chamber

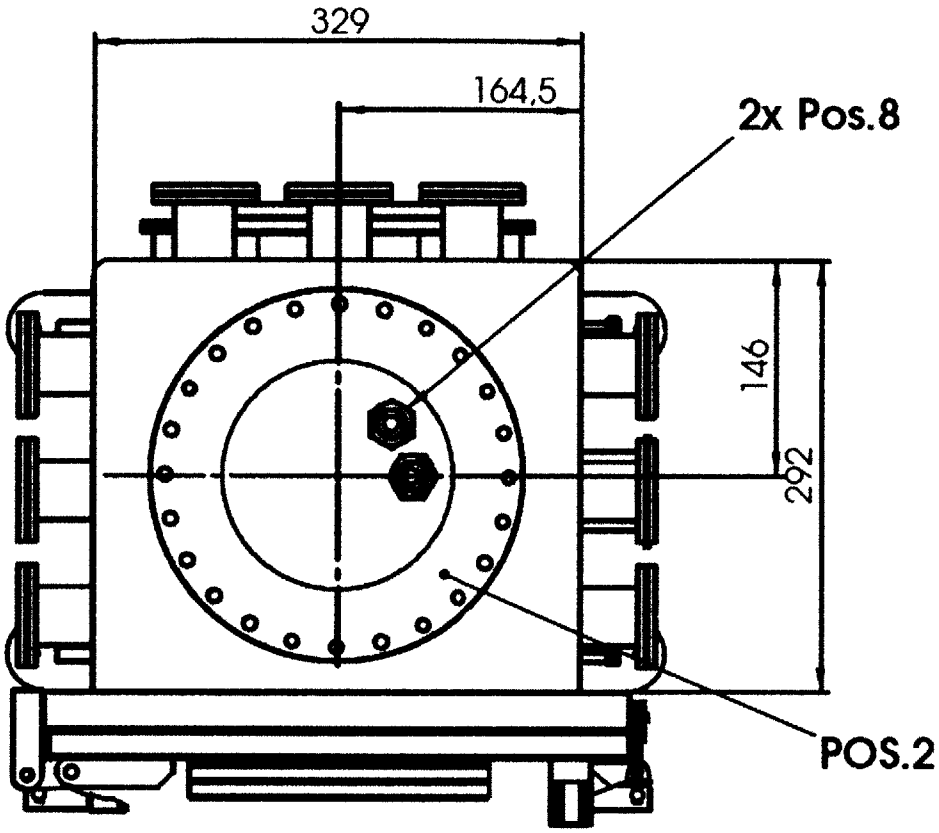

Figure B-7: oCVD chamber engineering drawings – top down view of chamber

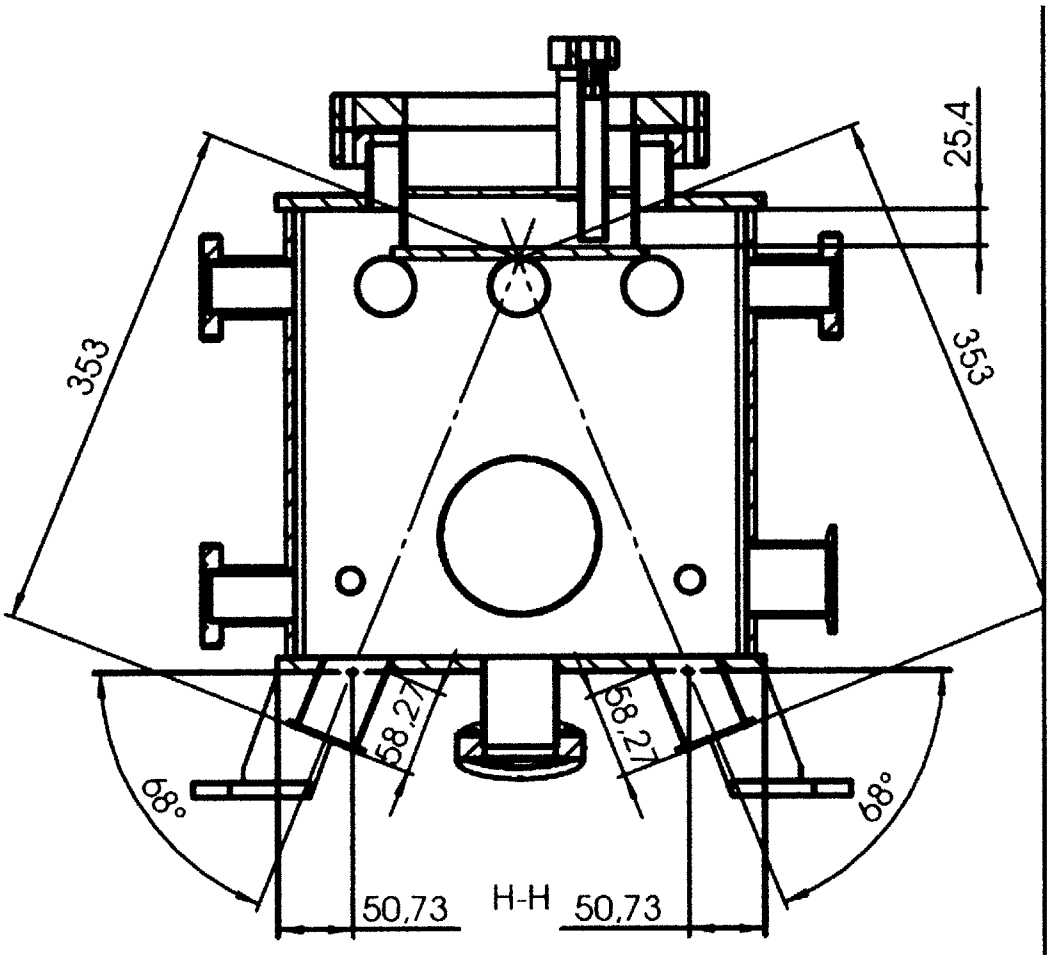

Figure B-8: oCVD chamber engineering drawings – view showing angled bottom ports with respect to stage location for interferometry measurements

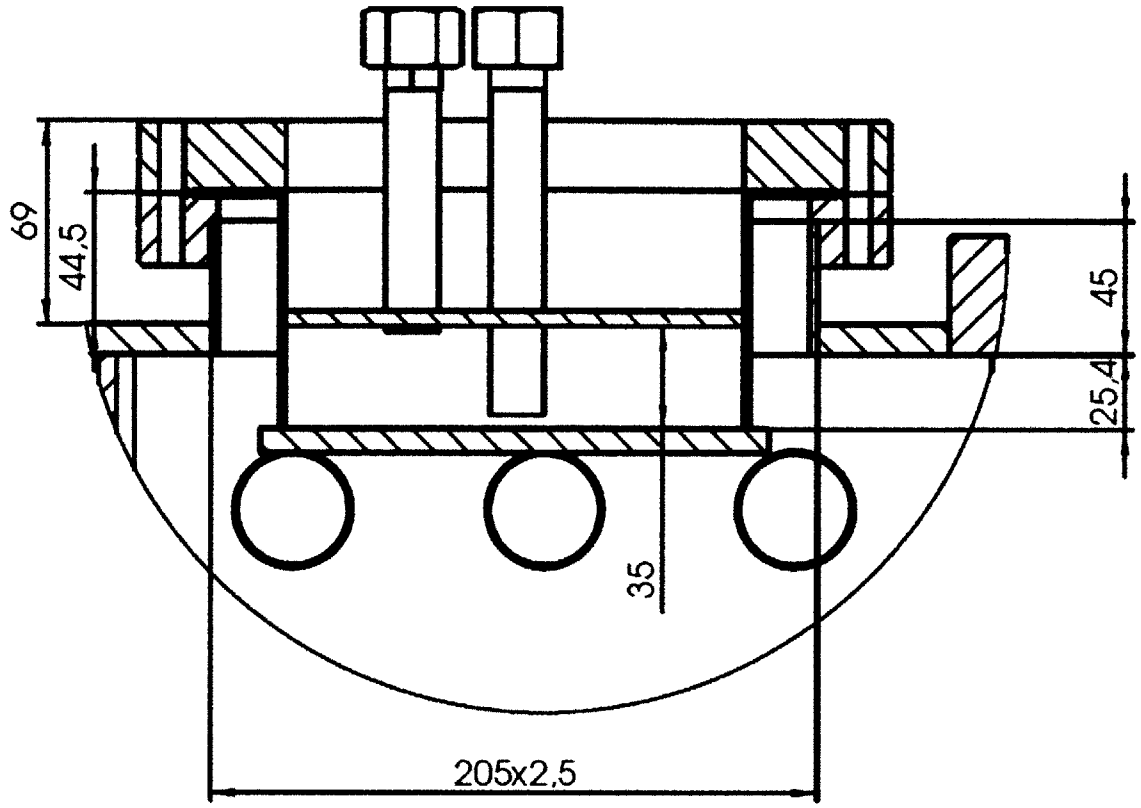

Figure B-9: oCVD chamber engineering drawings – close-up view of water-chilled top flange

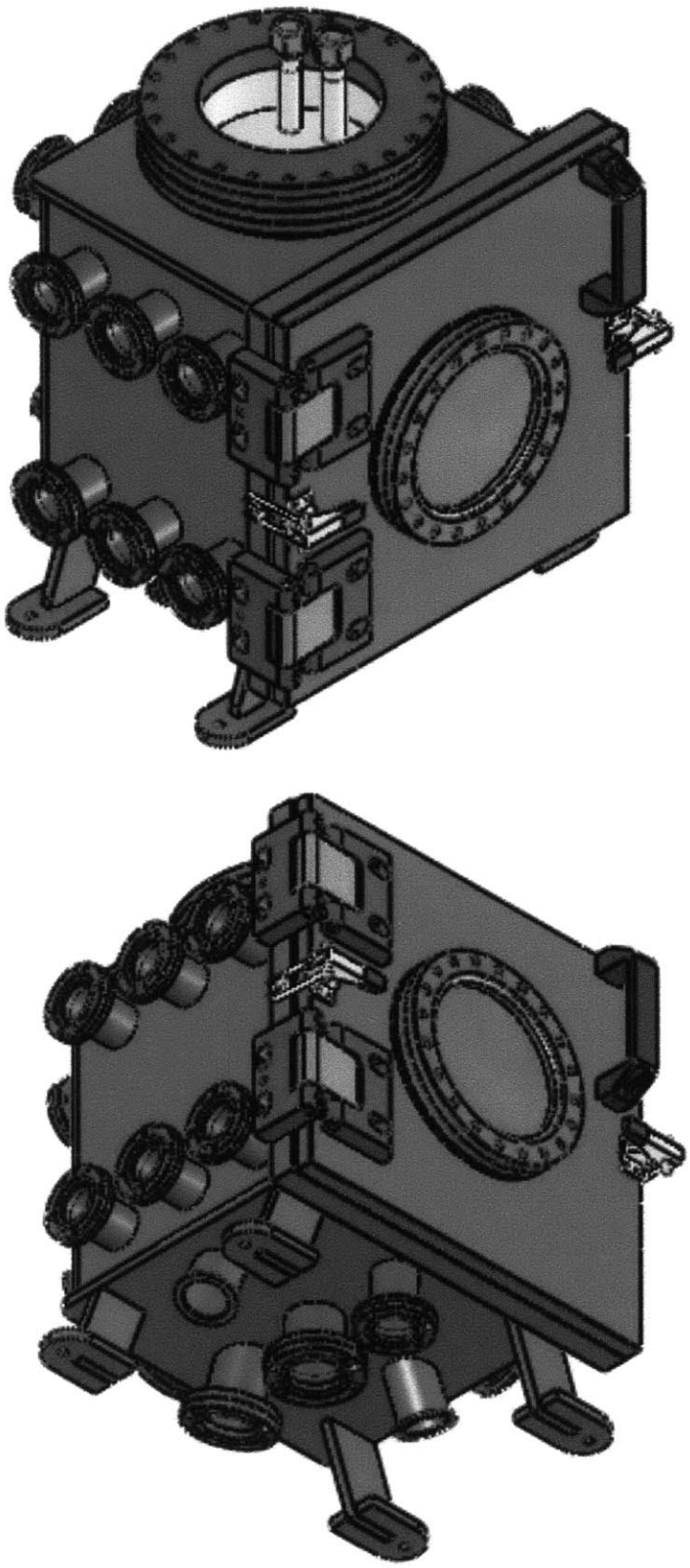

Figure B-10: 3D rendered views of chamber

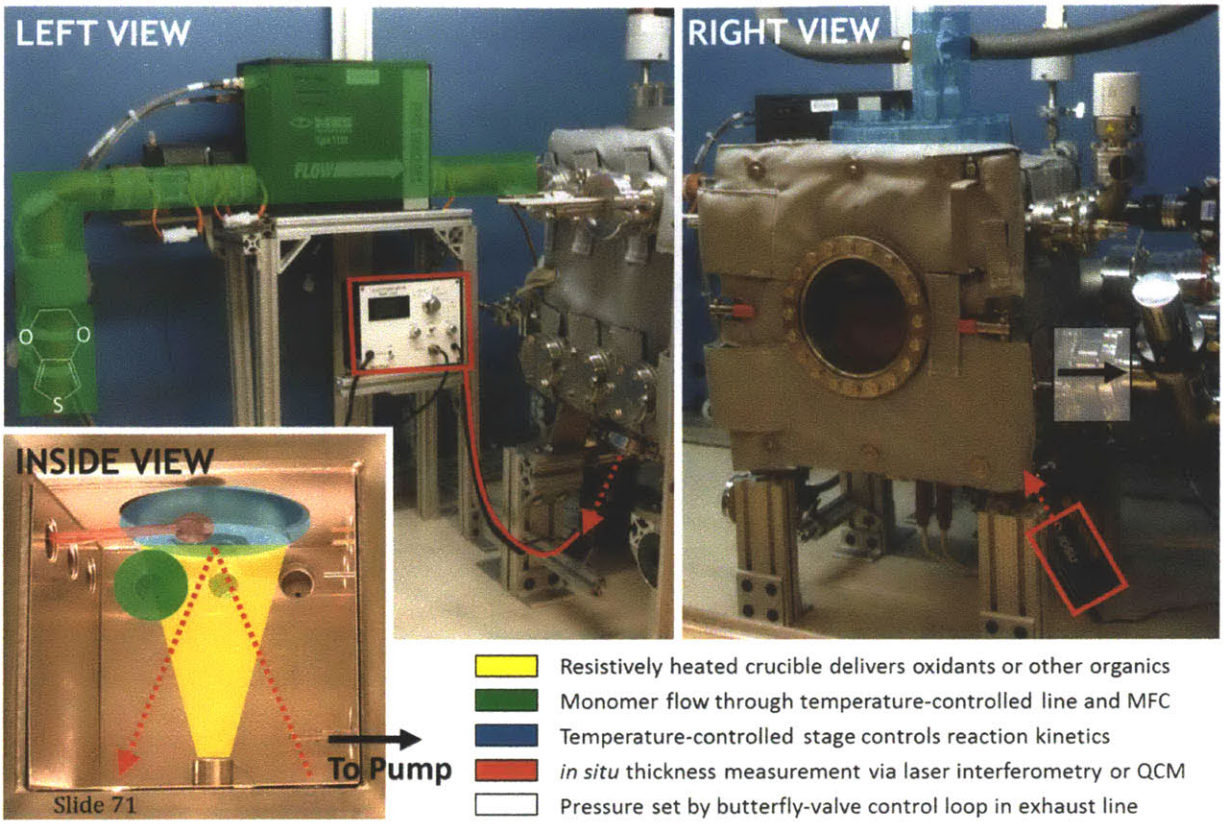

Figure B-11: Photographs labeled with oCVD chamber systems

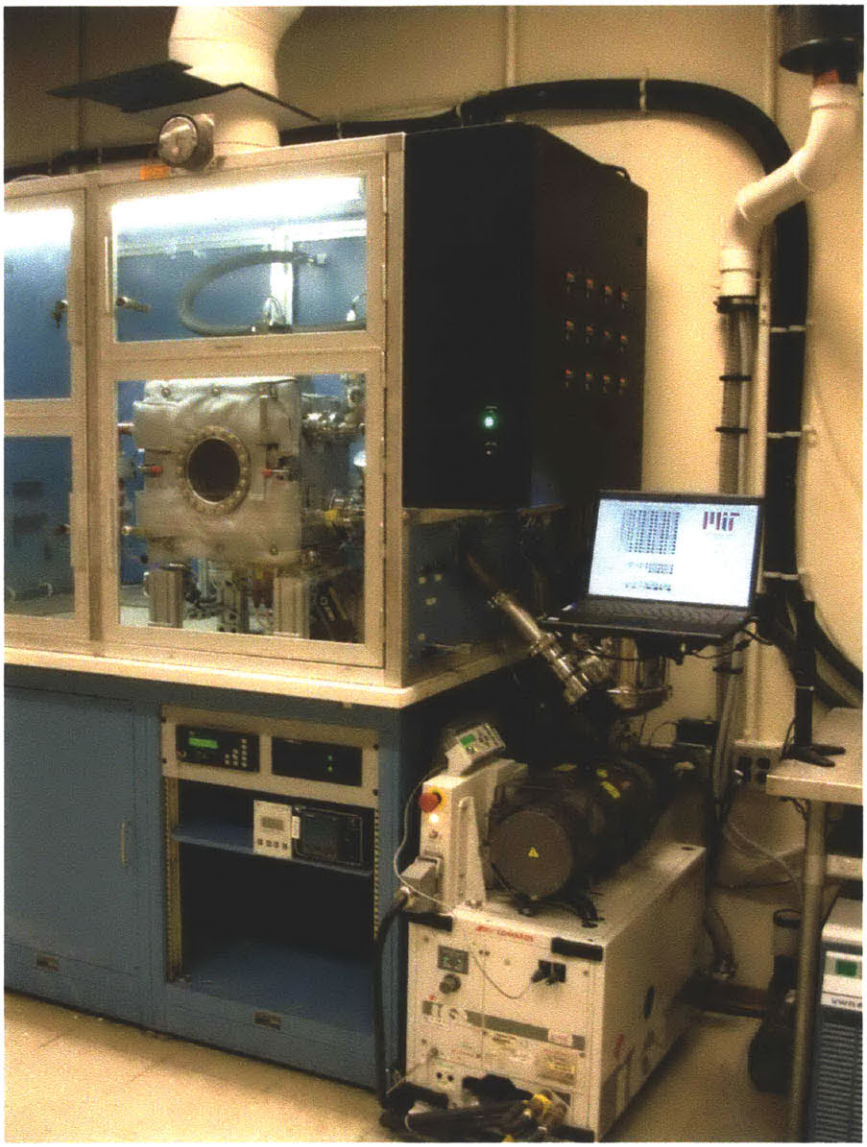

Figure B-12: Photograph of full oCVD system setup